Perpendicular Patterned Media for High Density Magnetic Storage

Thesis by

Joyce Y. Wong

In Partial Fulfillment of the Requirements

for the Degree of

Doctor of Philosophy

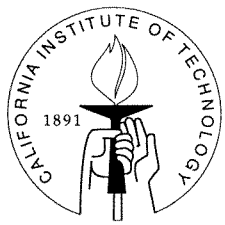

California Institute of Technology

Pasadena, California

2000

(Defended May 24, 2000)

Acknowledgements

I would like to thank my thesis advisor, Professor Axel Scherer, whose wealth of knowledge, kind personality, guidance, and patience has provided me with the type of research environment that has allowed me to learn, grow, excel, and enjoy graduate school. He has been an advisor who gives me the freedom to pursue what I think is important in my research, but at the same time, always being available when I need advice from his expertise in nanofabrication. I would also like to thank his wife, Dr. Teresa Cheeks-Scherer, whose support and advice is very much appreciated.

Another professor that I am very grateful to is Professor David Rutledge, who was my undergraduate thesis advisor. He has prepared me for the challenges of graduate school through his vast knowledge in electrical engineering and guidance during my senior thesis work. Other mentors that I am very grateful to are Professors Thomas Tombrello, William Bridges, Michael Roukes, Yu-chong Tai, Harry Atwater, Stephen Quake, and Slobodan Cuk at Caltech, and Professor Sheldon Schultz at the University of California, San Diego (UCSD). Their expertise in specialized fields and advice from their broad experience have been very helpful throughout undergraduate and graduate school.

I owe many thanks to Mladen Barbic, who is the graduate student that I work closely with in Professor Sheldon Schultz's group at UCSD. He is not only a collaborator, but also a good friend. I will always cherish all the frustrating times we encountered in the lab, as well as the excitement we shared when we first demonstrated recording in our patterned media samples. I would also like to thank Dr. Steven Yamamoto and Dr. Robert O'Barr, who are past members of Professor Schultz's group, for opening a path for us before we started our thesis work.

During the first two years of graduate school, I was involved in the tunnel displacement transducer project with Dr. Thomas George at the Jet Propulsion Laboratory (JPL). I want to thank him for providing us with the resources as well as support

throughout the project. Thanks also go to Patty Chang-Chien, for helping me with part of the fabrication that was carried out at JPL. For the last six years, I have also been one of the teaching assistants for the APh9 course. It has been fun and rewarding to work with undergraduate Freshman. I have enjoyed working with the other teaching assistants as well. I will miss being a part of that course after I leave.

I also wanted to extend my appreciation to two previous graduate students in our group, Dr. Chuan-cheng Cheng and Wei-hua Xu. They were always very informative and patient in training me on the equipment in the lab when I first worked in the group doing my undergraduate senior project. I am very glad to have Hou-pu Chou as a fellow graduate student in the group as well. It has been very helpful to have someone to go through some of the hurdles of graduate school, such as mini-oral and candidacy exam, and finishing our theses, together. Now, my officemates, Ali Husain and Mark Adams, are probably glad that I am finally graduating. It has been very comforting to have them, and especially Ali, listen to all my frustrations and worries, and to share my excitements as well. As for David Barsic, I have always enjoyed his easy-going personality and absurd humor. Those qualities have definitely made some of the frustrating times with processing in the lab more tolerable. He has also been a great help with maintaining all the equipment in the lab.

Other graduate students in the group that I would like to thank are Oskar Painter for discussion on GaAs processing, Tomoyuki Yoshie for his expertise in semiconductor fabrication, Jelena Vuckovic for her theoretical background in semiconductor physics, and Marko Loncar for his knowledge in XeF_2 etching. I have enjoyed working with all of them during the last few years. I would also like to thank Oliver Dial, a former undergraduate in our group, for converting our commercial scanning electron microscope into an e-beam writer. I have enjoyed having Tom Baehr-Jones, Michael Hochberg, and Ben Lee work with us as undergraduates as well.

I would like to express my gratitude to Dr. Theodor Doll, a visiting associate in our group for the last year and a half. His motivation and devotion toward science has inspired me in my work. It has definitely been great fun working together with him in the lab and having him as a part of our group. It has also been a pleasure

knowing his family in Germany. I would also like to thank other visiting associates, Dr. Thomas Krauss, Dr. Tony Loomis, and Dr. David Wei, for their knowledge and experience from industry and other universities and laboratories. Reynold Johnson, the former technical engineer in our group, has my appreciation for all his help in setting up and maintaining the fabrication equipment in our lab. I am also thankful to him for teaching me the basics of machining work. Many thanks also go to the assistants in our group, Michelle Vine and Kate Finigan, who have allowed me to better focus on my thesis project by taking care of all the administrative work.

I am very grateful to Marlene and Cesar Moncada, for their friendship and support during the last couple years of graduate school. Friends have always been an important part of my life, and I would like to especially thank a few long-time friends, Irene Chan, Carmen Davis-Reid, Dr. Amit Mehra, Dr. David Lande, Erick Co, Jerry Shan, and Dr. Joseph Lee for always being there when I need them. In addition, Dr. John Davis, Dr. Alina Moussessian, Tony Vanelli, Lee Burrows, Dr. Bill Weber, Dr. Ayhan Irfanoglu, Wen Hsieh, Ellis Meng, Dr. Thomas Tsao, Dr. Zvonimir Bandic, Elizabeth Boer, Dr. Frank Monzon, Dr. Keith Schwab, Dan Provenzano, Roger Koumans, and Will Green are some fellow graduate students and post-doctoral scholars that I would like to express my appreciation for their friendship.

I am very much indebted to my parents for their kindness, thoughtfulness, support, and encouragement throughout all these years. I am also obliged to my sister, Natalie, who is always there to share my joy and sadness. Without my family and relatives, I would not have been where I am now. Last but not the least, I am always beholden to Reginald Lee, for his friendship and all the wonderful memories that we shared during graduate school.

Even though I was strongly encouraged to go to another graduate school to get a different perspective, I decided to stay at Caltech mainly because of the sincerity and quality of the people in this group, as well as in the different departments here. Now that my graduate life is coming to an end, I am still glad I made that choice, and would not have done it any differently if I had to choose again.

Abstract

Current longitudinal thin-film media in magnetic hard-disk drives are facing an oncoming limit caused by the superparamagnetic effect, in which the individual grains in the medium become so small that they are no longer stable against thermal fluctuation. This situation is undesirable as the stored information may be lost within an unexpectedly short time frame. There have been several proposed solutions in addressing the superparamagnetic limit, and one of them is perpendicular patterned media. In this approach, a periodic array of magnetic pillars is defined lithographically on a non-magnetic substrate. Binary data of "1" or "0" can be stored in each of these elements, which have two possible magnetization directions perpendicular to the plane of the medium.

In our perpendicular patterned media design, Ni columns of 150–230nm diameter with a 6:1 aspect ratio are embedded in an $(AlGa)_2O_3$/GaAs substrate. The fabrication procedure uses a combination of high resolution electron beam lithography, dry etching, and electroplating. The high aspect ratio in the column is achieved by taking advantage of the high etching rate and selectivity of AlGaAs/GaAs over $(AlGa)_2O_3$ in the Cl_2 chemically assisted ion beam etching process. In addition to being a robust etching mask, the $(AlGa)_2O_3$ layer also plays an important role in the chemical mechanical polishing procedure to remove the overplated Ni mushrooms.

Once the Ni columns are fabricated, magnetic characterization is performed using magnetic force microscopy and scanning magnetoresistance microscopy. The former measurement confirms that the electroplated Ni columns are magnetic while the latter determines whether the individual columns are stable enough to retain the recorded information. We have successfully demonstrated recording in our 170nm diameter Ni column array arranged in a square format using a commercial read/write head. This is the first demonstration of single magnetic column per bit data storage in a prototype perpendicular patterned medium. Furthermore, we have recorded in higher

density Ni column arrays in the form of tracks, corresponding to 1.3 and 2.6Gbits/in.^{2}. Even though we are limited by the spatial resolution of the magnetoresistive read sensor, we have continued to pursue higher density structures up to an areal density of 350Gbits/in.^{2}. Consideration of the issues in high resolution patterning and the magnetic stability of the individual columns have prompted researchers in the magnetic recording industry to anticipate the ultimate storage limit of perpendicular patterned media to be around 1Tbits/in.^{2}.

Contents

List of Figures

Chapter 1 Introduction

1.1 Brief background and current trends in magnetic recording

Magnetic hard-disk drives have continued to be a popular avenue for data storage since their introduction—the Random Access Method of Accounting and Control (RAMAC) drives—in 1956 by IBM. The RAMAC drive was capable of storing up to five million characters on its 50 aluminum platters, each of which was 24in. in diameter and coated on both sides with magnetic iron oxide. The drive weighed nearly a ton and occupied the same floor space as two modern refrigerators [1]. Amazingly, this type of storage format has been able to sustain its demand, even after more than four decades since its appearance in the consumer market, mainly due to the combination of its rising capacity and declining price through all these years. The capacity of hard-disk drives grew about 25 to 30% each year through the 1980s and accelerated to an average of 60% in the 1990s (see Figure 1.1) [1]. By the end of last year the annual increase had reached 130%. At the time of writing, the areal density of commercial hard-disk drives is $\sim$14Gbits/in.^{2}, and laboratory demonstrations $\sim$50Gbits/in.^{2} have been reported. In the semiconductor industry, the increasing number of transistors used in a modern computer seems to obey Moore's law (doubling every 18 months). In the hard-disk industry today, the storage capacities have been rising at an even more surprising rate of doubling every nine months. Researchers have been predicting that by the year 2002, the areal density in commercial hard drive products would reach $\sim$25Gbits/in.^{2} or higher.

The basic design of a current commercial hard-disk drive still traces its origin back to the first RAMAC drive. It consists of a stack of disk platters, typically made of an aluminum alloy or glass substrate coated with a magnetic material and protective

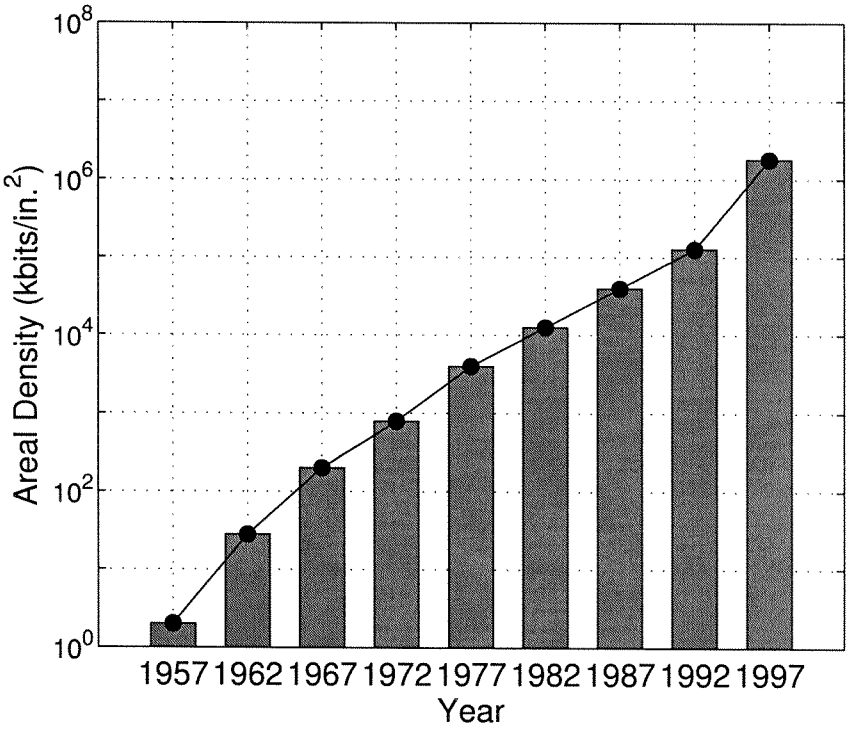

Figure 1.1: Bar chart showing the trend in the annual increase in areal density (no. of bits per square inch) in the magnetic recording industry. Data points in the graph are taken from Reference [1].

layers. The recording layer of the disk is composed of a thin, sputtered, multialloyed magnetic film that consists of many grains, each of which is the basic unit that makes up every bit of information. This stack of platters is rotated at speeds of 3600 to 10,000 revolutions per minute by a spindle motor. The process of data recording and retrieval is performed by read/write heads, which are located on both sides of each platter. The data are stored on the disks in circumferential track formats. Each of the recording heads is suspended over the medium at a distance on the order of fractions of microinches. This precise head-medium spacing control is made possible by servomechanical actuator arms as well as hydrodynamic air bearings.

So far the achievements in the continual increase in areal density in magnetic storage have largely been the result of direct miniaturization. For example, focused ion-beam milling has been used to trim the physical dimensions of recording heads. As for the media, thinner disks and smaller grains are used for higher packing density. The flying height between the head and the media has been minimized to store and retrieve weaker signals from the smaller bits. There are of course innovations, such as in the read sensor technology, that have helped keep magnetic recording on competitive ground as well. At some point, however, scaling alone will not be sufficient to meet the demand. Research efforts have been invested in all aspects of the current magnetic storage system to improve its ability for higher density storage.

One of the less obvious areas that is being heavily explored in the magnetic recording industry today is high-resolution lithography tools and large-area patterning techniques. The issue of "next generation lithography" (NGL) is a prevailing topic in the semiconductor industry these last few years. This is not surprising considering the fast-pace decrease in the critical dimensions in transistors and other electronic components found in modern semiconductor devices. Up till now, and probably for the next few years, the magnetic storage industry can continue to capitalize on the advances in lithography tools available primarily due to investments and demand from the semiconductor industry. Many people have anticipated, however, that by the year 2005 or so the storage density requirements in magnetic recording will force the minimum feature size in recording medium and heads to be smaller than that in semi-

conductor devices. The cross-over in the minimum feature size trend would indicate that the magnetic storage industry can no longer solely rely on the semiconductor industry for advances in high resolution lithography developments. In order to be equipped for this possible contingency, the magnetic recording industry has already started research on next-generation lithography tools that can be incorporated into the processes involved in the fabrication of future media and heads.

Whether the magnetic storage industry can deliver products that meet the predicted areal density trend (seen in Figure 1.1) for the next decade is still an open question. There is a physics limit that may be encountered in the coming years due to the superparamagnetic effect. This phenomenon occurs when the magnetic grains in the recording medium have become so small (to meet the areal density requirements) that they are vulnerable to thermal fluctuations. In other words, even ambient thermal energy is sufficient to randomly flip the spins (from "0" to "1" and vice versa) in the atoms that hold the recorded information. This situation is highly undesirable in any storage system, and researchers have been working persistently to keep up with the ever-increasing demand for higher storage densities and, at the same time, delay the onset of the superparamagnetic effect.

The capability of the recording medium to retain the archived information, as well as the speed at which the data is retrieved, will be the primary factors determining the destiny of magnetic storage. If and when magnetic recording can no longer meet the challenge of the areal density and data retrieval requirements, perhaps one of the alternative and more revolutionary technologies that are currently being investigated will emerge and prove itself as a viable future information storage solution and become the successor of magnetic recording.

1.2 Motivation behind patterned media

The concept of patterned media, or the lithographic patterning of arrays of individual nano-scale magnets, holds the prospect of advancing magnetic storage to areal densities exceeding the predicted limit of conventionally sputtered, multialloyed thin-film

recording media. Instead of having hundreds of magnetic grains per bit, patterned media utilizes only one larger-sized magnetic particle for every bit of stored information. Due to the larger volume of each bit, the onset of the superparamagnetic effect, a state at which the individual bit is no longer stable against thermally activated magnetization reversal, should in principle be delayed. If only superparamagnetism is the limiting factor, then patterned media can increase the current magnetic storage densities in conventional media by $\sim$100 times or more, using the same medium material. Assuming that each bit is small enough to be single domain, and large enough to be thermally stable, a square array of nano-magnets with a periodicity of 45nm or smaller would correspond to storage densities of 350Gbits/in.^{2} and beyond. There are of course additional constraints, such as lithographic patterning defects, read/write head design, and requirements in the signal-to-noise ratio and speed in data retrieval, that need to be taken into consideration for implementing patterned media in an actual recording system. Patterned media, however, is still believed to be a viable technology to extend the current magnetic storage densities to 1Tbits/in.^{2} and beyond.

1.3 Our experimental approach for high density magnetic storage

There has been a great deal of research on different approaches of fabricating patterned media, but a demonstration that bridges the gap between fabrication and the realization of patterned media as a storage medium using commercial recording heads was not evident. We feel this type of demonstration will serve as a starting point for any further commercialization if perpendicular patterned media were to become the successor of the current thin-film media in the future.

I emphasize here that the goal of our work is to demonstrate the feasibility of perpendicular patterned media as a viable solution for magnetic recording densities of 100Gbits/in.^{2} and beyond, using a similar recording architecture as the current

magnetic media. It is not, however, our intention to prove the patterned media concept on a spinning hard-disk with a suspended recording head "flying" over it, along with the proper head servomechanism, channel coding, and error detection/correction schemes.

Instead, our approach is to first identify the media requirements assuming a similar set of constraints associated with the recording head used in a commercial hard-disk drive today. Then we decide on the materials used for the magnetic columns that form each bit, as well as the appropriate substrate to support the columns. During this process, we need to also make sure that the materials selected for the columns and substrate are compatible with the fabrication tools available in our laboratory. This limits our material options, and our choice for the columns and substrate may not necessarily be optimized for commercial use. In addition, the techniques we use to fabricate the magnetic columns have a relatively low throughput compared with commercial production, and our sample area is small as well. These are not limiting factors in the fabrication process, however, and are more than sufficient for our experimental work. Once the samples are fabricated, we then move forward to demonstrate whether we can record in the individual columns using a commercial read/write head. The diameter of the columns in our design is chosen so that there is enough readback signal, and the spacing is selected such that there is sufficient clearance between neighboring columns for a commercial write element to record in and a read sensor to resolve the signals from each of the columns. This demonstration is performed in a static fashion, instead of on an industrial spin-stand, and the recording head is scanned in contact over the perpendicular patterned media sample to record in each magnetic column one at a time.

Despite some of the product-oriented shortcomings, we did demonstrate, on a research level, the fabrication of perpendicular patterned media samples that are compatible with a current recording head, as well as the controllable storage of data in our samples using commercial inductive write and spin-valve read transducers. My hope is that this thesis will give you a brief tour from where we started a few years ago to where we are now with our perpendicular patterned media project, which is a

collaborative effort with Professor Sheldon Schultz and his graduate student, Mladen Barbic, at the Center for Magnetic Recording Research at the University of California, San Diego.

Before describing my thesis work in detail, I have included some basic concepts in magnetism as well as the important aspects, mechanisms, and tools used in the recording process in magnetic storage in Chapter 2. For readers who are experts in these areas, a more appropriate starting point may be Chapter 3 instead. In Chapter 3, on-going research and development on current thin-film recording media for storage densities of 100Gbits/in.^{2} and beyond is described. The patterned media concept is also introduced in this chapter. Both the perpendicular and parallel configurations are mentioned, but the focus is on the former. Several of the main design issues in perpendicular patterned media, such as material selection and the geometry of the bits to achieve thermally stable columns, are interpreted. Alternative storage technologies for the next generation information storage are suggested, and in particular, a hybrid approach combining optical and magnetic recording is briefly explained. In Chapter 4, some of the work I was involved in during my senior year as an undergraduate on fabricating Ni columns embedded in an electron-beam resist are described. In addition, a brief description of the work between our group and two previous members of Professor Schultz's group (Drs. Steven Yamamoto and Robert O'Barr), in embedding Ni columns in SiO_2, is included. Even though recording was not demonstrated in these previous works, their results have provided us with a more solid ground for the start of our perpendicular patterned media research.

In Chapter 5, details of the fabrication of Ni columns embedded in an Al_2O_3/GaAs substrate are reported. Issues in the design of the substrate and the materials and geometry of the magnetic columns are discussed. The fabrication tools and the processing procedures involved are described. Scanning electron micrographs that show the etching and electroplating profile during the fabrication process of the embedded Ni columns are illustrated. The magnetic characterization procedures are discussed in Chapter 6, which includes explanation of the measurement techniques using magnetic force microscopy and scanning magnetoresistance microscopy. The chapter ends with

the demonstration of data storage in our perpendicular patterned media samples, as well as more details on the writing configurations and a few modeling results of the writing and reading process using a commercial head. For a more detailed description of the magnetic characterization portion of this work, refer to the dissertation by Mladen Barbic [2].

In Chapter 7, recent work on higher density structures in the Al_2O_3/GaAs substrate and other material systems are shown. Even though we are limited by the physical dimension of the commercial read/write head to demonstrate recording in these structures, they confirm the capability of our current fabrication techniques to satisfy the areal density requirements of 350Gbits/in.^{2} and beyond. Some of the limitations in high resolution lithographic patterning as well as the criteria in determining the thermal stability of the storage medium are discussed. Considering the issues from the standpoint of both lithography and magnetics, the anticipated limit of perpendicular patterned media is estimated. Finally, my thesis work is summarized in Chapter 8, along with a brief description of current technologies for atomic resolution storage.

Chapter 2 Concepts, processes, and tools in magnetic information storage

This chapter is intended to give a brief overview of some of the concepts in magnetism that have primary roles in determining the material, medium, recording processes and tools in magnetic information storage. For more in-depth study and description of the concepts and theory of magnetism and magnetic materials, see References [3, 4, 5, 6, 7, 8, 9], and References [10, 11, 12, 13, 14, 15, 16, 17] for more information on magnetic storage technology.

2.1 Single-domain particles

Single-domain particles were first postulated by Frenkel and Dorfman in 1930 [18]. Calculations of their critical size and behavior were reported subsequently by Kittel [19], Néel [20], and Stoner and Wohlfarth [21]. A simplistic way to define the single-domain state in a particle is that the magnetization needs to be uniform throughout the entire particle. The trade-off between magnetostatic and domain wall energies plays a critical role in determining whether a particle becomes single-domain.

2.1.1 Magnetostatic energy

According to Cullity [5], if a material is magnetized by an external bias field to some level denoted by A as shown in Figure 2.1, and the field is then removed, the magnetization of the material will decrease to a level denoted by C in the figure due to the influence of the demagnetizating field H_d. Here OC is the demagnetizing-field line, which has a slope of $-1/N_d$, where N_d is the demagnetizing coefficient. The amount of energy stored in the material, or the self-energy, or the energy of a magnet

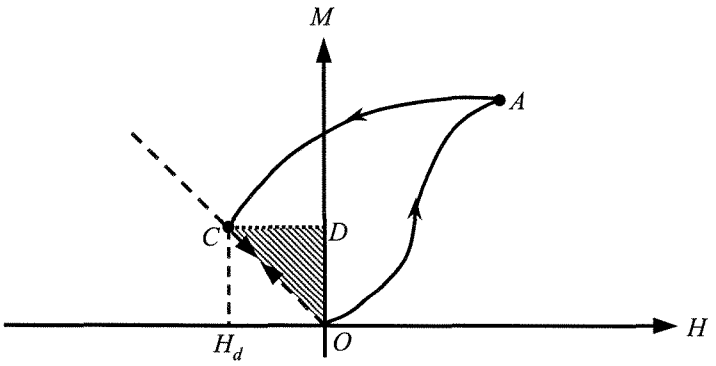

Figure 2.1: Schematic diagram showing the magnetostatic energy of a magnetized material after the removal of an external bias field [5].

in its own field, is also known as the magnetostatic energy, E_{ms}, and is given by

$$E_{ms} = \frac{1}{8\pi} \int H_d^2 dv \text{ ergs}, \tag{2.1}$$

where dv is an element of volume and the integration extends over all space. The evaluation of the integral in Equation 2.1 is difficult, and it is simpler to calculate the area inside the shaded triangle, ODC, which gives the energy density as

$$\frac{E_{ms}}{V} = \frac{1}{2} H_d M_s \text{ ergs/cm}^3, \tag{2.2}$$

where V is the volume of the material and M_s is the magnetization at point C in the figure. Since $H_d = N_d M_s$, Equation 2.2 can be written as

$$\frac{E_{ms}}{V} = \frac{1}{2} N_d M^2 \text{ ergs/cm}^3. \tag{2.3}$$

2.1.2 Domain formation and structure

Now consider a large single crystal of a uniaxial substance. The process in which the structure is divided up into domains is depicted in Figure 2.2 [5]. Suppose that the structure originally consists of only one domain, spontaneously magnetized to a direction parallel to its easy axis, as shown in Figure 2.2 (a). The free poles formed at the ends will constitute a large demagnetizing field. The magnetostatic energy

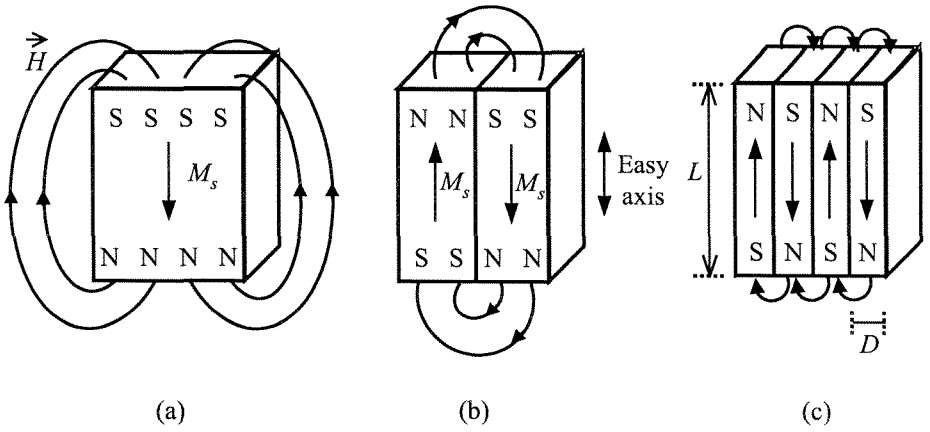

Figure 2.2: Schematic diagram showing the division into domains in a large uniaxial structure [5].

associated with this demagnetizing field is given by Equation 2.1, which is evaluated over all space where H is appreciable. And for a single-domain crystal, this energy is $E_{ms} = N_d M_s^2/2$. If the crystal is split into two domains, as shown in Figure 2.2 (b), then this large amount of energy can be lowered by approximately a factor of two, which is a more favorable energy state. If each of these smaller domains now continues to split into two, i.e., we have a total of four domains as shown in Figure 2.2 (c), then the magnetostatic energy of the crystal will be one-fourth of its original value when there is only one domain. This splitting process cannot continue indefinitely, however, as each splitting creates a domain wall, which adds energy (also called domain wall energy, E_{wall}) to the entire system.

The domain wall energy can be written as $E_{wall} = \gamma L/D$, where γ is the domain wall energy per unit area and L/D is the wall area per unit area of the top surface of the crystal. An example of the amount of energy gained by the creation of domains is given by Cullity [5] in the case of cobalt (Co). For $\gamma = 7.6$ ergs/cm^2 and $L =$ 1cm, the minimum energy occurs when the 1cm cube of Co crystal is split into some 700 domains, with domain width of 1.5×10^{-3}cm. The ratio of the energies before and after the splitting into domains varies as a function of $\sqrt{L}$, and a thousand-fold reduction in energy results from the formation of domains. So there is an advantage of creating domains to some extent, after taking in account the trade off between

losing magnetostatic energy and gaining domain wall energy in the process.

2.1.3 Critical dimension for single-domain behavior

Since the reduction in magnetostatic energy as the crystal splits into domains varies as $\sqrt{L}$, as L becomes smaller and smaller, the advantage of lowering the magnetostatic energy over gaining domain wall energy will become less significant. At some point, a critical value of L_c will be reached, below which there will be an energy penalty for any further division into domains, and the crystal will prefer to stay as single domain. Cullity [5] gives an approximate expression for L_c as follows:

$$L_c = \frac{1.7\gamma}{\pi^2 M_s^2}. \tag{2.4}$$

Equation 2.4 is not exactly valid for all materials, but it gives the correct relation between L_c and γ and M_s. If the domain wall energy per unit area of wall, γ, is large, then the energy cost for creating more domains will make it more reasonable to have a larger-sized single domain (i.e., larger L_c) than splitting the crystal into many domains. If M_s is small, then the gain in magnetostatic energy by division into domains becomes insignificant as well. So the crystal prefers not splitting into smaller divisions, thus resulting in a larger-sized single domain.

Besides the individual material properties, the shape of the crystal also affects the critical size below which a particle becomes single-domain. For instance, an elongated particle will have a lower demagnetizing field along its long axis when compared to a cubical or spherical particle. The magnetostatic energy associated with this lower demagnetizing energy will in turn be smaller as well. Similar to the case with a small M_s in Equation 2.4, an elongated particle tends to have a larger-sized single domain before breaking up into several domains.

In the case of small spherical ferromagnetic particles, the critical radius, r_c, below which the particles become single-domain is found by equating the magnetostatic demagnetizing energy of the single-domain state and the total energy for the two-domain state. To get a more quantitative value of the critical radius, we consider a

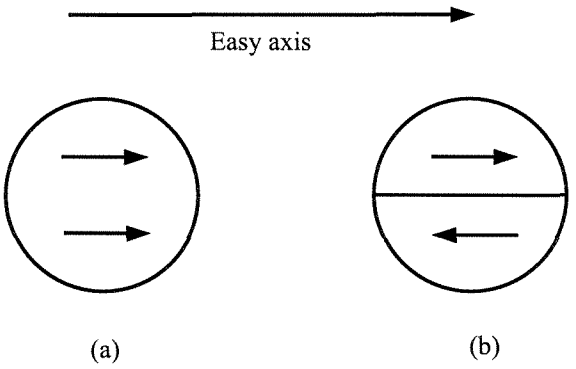

Figure 2.3: Schematic diagram showing a small ferromagnetic particle in a single domain (a) and two-domain (b) state.

Co particle with a radius of r and a domain wall energy density of $\gamma = 7.6\text{ergs/cm}^2$, as shown in Figure 2.3. The magnetostatic demagnetizing energy of the single-domain state [see Figure 2.3 (a)] is:

$$E_{ms(sd)} = \frac{1}{2} N_d M_s^2 \cdot \frac{4}{3}\pi r^3 \text{ ergs}, \tag{2.5}$$

where N_d is the demagnetizing factor, which is 1/3 for spheres. The total energy for the two-domain state [see Figure 2.3 (b)] is:

$$E_{wall(md)} = \gamma \cdot \pi r^2 \text{ ergs}. \tag{2.6}$$

The critical radius r_c is given by [10]:

$$\begin{aligned} E_{ms(sd)} &= E_{wall(md)}, \\ r_c &= \frac{9\gamma}{8\pi M_s^2} \\ &\approx 1.3 \times 10^{-6}\text{cm} \\ &= 13nm, \end{aligned} \tag{2.7}$$

where $M_s = 1422\text{emu/cm}^3$ is used for Co.

It is noted that the above argument is not a general case since it only takes two very specific domain configurations for small ferromagnetic particles into consideration.

Brown used the thermodynamic principle to prove that the single-domain state for a sufficiently small magnetic particle has a lower energy state than any other possible multi-domain states [22]. According to his theorem, the state of lowest energy for a single crystal homogeneous spherical magnetic body is a single-domain state of uniform magnetization if its radius (r) is smaller than a certain value (r_1), and a multi-domain state if r is greater than a certain value (r_2). In the intermediate range, $r_1 < r < r_2$, the behavior of the particle is evidence of both a single- and multi-domain particle. This is the size range where there may be no domain formation within the particle, but the element does not reverse coherently, as in the single-domain case. Although Brown's theorem was only rigorously proven for single-domain crystal spheres or prolate spheroids [23] that have uniaxial or cubic anisotropy, it is often applied in the general category of small magnetic particles. Wang et al. [17] noted that when working with polycrystalline magnetic materials as well as single-domain particles that are not entirely uniformly magnetized in practice, caution should be taken in applying Brown's theorem.

2.2 Superparamagnetism

In 1949, Néel [24] pointed out that when a single-domain particle is below a critical volume, thermal energy may be sufficient to reverse its magnetization from one easy (preferred) direction to the other, even in the absence of an external bias field. This occurs if the total anisotropy energy of the particle, KV, is of the order of the thermal energy, k_BT. Here, K is the anisotropic energy density constant, V is the volume of the particle, k_B is the Boltzmann constant, and T is the absolute temperature. The term "superparamagnetism" was coined by Bean to describe the behavior of single-domain particles that behave very much like normal paramagnetic particles, with the exception that a superparamagnetic particle (containing thousands of atoms) has a relatively enormous magnetic moment compared to that of an ion or atom in a normal paramagnet [25, 4]. The magnetization behavior of an array of identical superparmagnetic particles can be described by the Brillouin function of a paramagnet, which

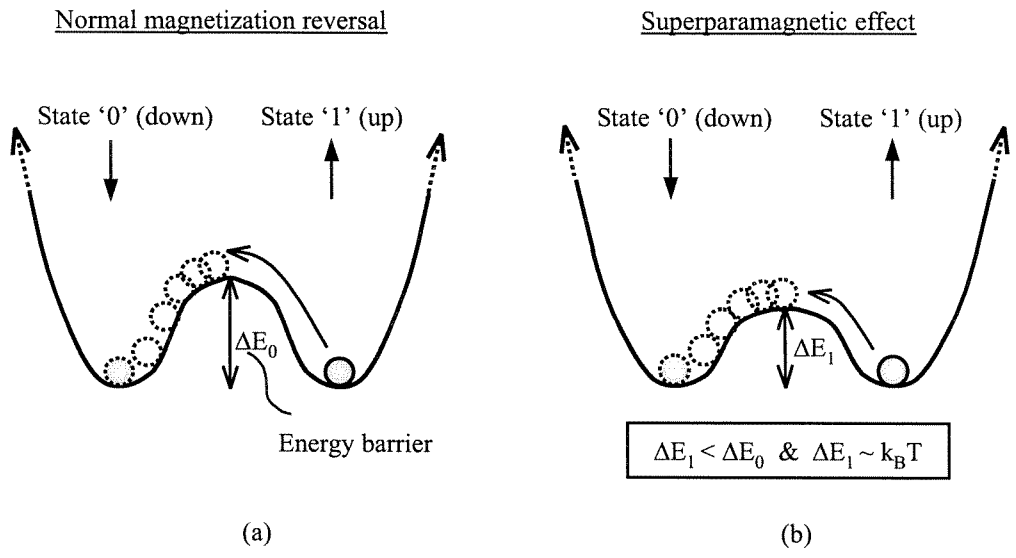

Figure 2.4: An illustration showing the difference in the energy barrier between the two possible magnetization states of a magnetic particle (a) before and (b) after the particle reaches a critical size for the onset of the superparamagnetic effect.

has no magnetic hysteresis [17].

2.2.1 Magnetization reversal

In order to better understand superparamagnetism, we need to have an insight on the mechanisms involved in the magnetization reversal process. Consider the illustration depicted in Figure 2.4 (a). The two possible magnetization states of a magnetic particle (up or down direction) occur at the two local minimum points in the energy axis of the particle. If the particle is in state "1" (up direction), a minimum energy of E_0 is necessary in order for it to overcome the energy barrier to reverse its magnetization to state "0" (down direction). As the size of a single-domain particle decreases, the energy barrier will be lowered as well. At some point, the energy barrier will drop to a value comparable to the thermal energy, i.e., $\Delta E_1 \sim k_B T$ [Figure 2.4 (b)], and thermal fluctuations alone will be sufficient to reverse the magnetization of the particle.

This energy barrier, ΔE_0, associated with the spontaneous magnetization reversal process, is primarily determined by the magnetic anisotropy energy of the particles

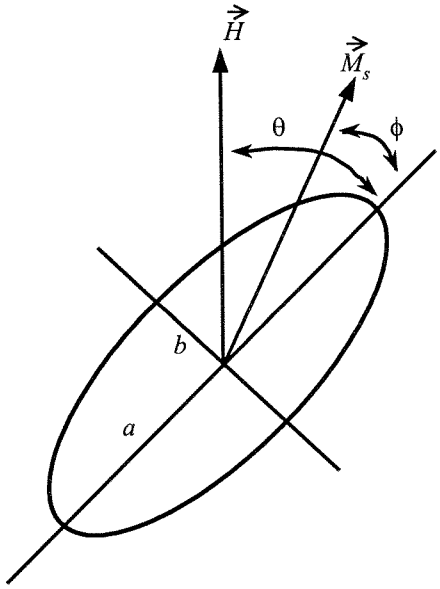

Figure 2.5: Illustration of a single-domain prolate spheroidal particle [17].

to be switched. Consider a single-domain prolate spheroidal particle illustrated in Figure 2.5. Without an external bias field, the particle will have its magnetization parallel to the easy (long) axis, and its energy at a minimum [21]. When an external field, H, that is at an angle, θ, with respect to the easy axis is applied, the magnetization of the particle rotates towards the direction of the applied field. The energy density of the particle is given by [17]:

$$\frac{E}{V} = K \sin\phi^2 - HM_s \cos(\theta - \phi) \text{ ergs/cm}^3, \tag{2.8}$$

where M_s is the saturation magnetization of the particle, V is the particle volume, and K is the uniaxial anisotropy constant.

If we now assume that the external applied field, H, is parallel to the easy axis, but in the opposite direction to the initial magnetization, i.e., $\theta = \pi$, then Equation 2.8 becomes:

$$\frac{E}{V} = K \sin\phi^2 + M_s H \cos\phi \text{ ergs/cm}^3. \tag{2.9}$$

The two local minima of energy occur at $\phi = 0$ ($E_{min} = M_s HV$) and at $\phi = \pi$

($E_{min} = -M_s HV$). In order to determine the peak value of the energy barrier, we set the derivative of Equation 2.9 with respect to ϕ equal to zero:

$$\begin{aligned} \frac{1}{V}\frac{dE}{d\phi} &= 2K\sin\phi\cos\phi - M_s H\sin\phi = 0, \\ \cos\phi &= \frac{M_s H}{2K}. \end{aligned} \tag{2.10}$$

Substituting the above expression into Equation 2.9, the energy density peak of the barrier is found to be [17]:

$$\frac{E_{max}}{V} = K[1 + (\frac{M_s H}{2K})^2] \text{ ergs/cm}^3. \tag{2.11}$$

The energy barrier is given by the difference between the maximum and minimum energy as [17]:

$$\begin{aligned} \Delta E &= E_{max} - E_{min} \\ &= KV(1 - \frac{M_s H}{2K})^2 \\ &= KV(1 - \frac{H}{H_0})^2 \text{ ergs}, \end{aligned} \tag{2.12}$$

where $H_0 = 2K/M_s$ is often known as the "intrinsic" coercivity (or anisotropy field). From Equation 2.12, we see that if the external applied field is equal to the intrinsic coercivity of the particle, i.e., $H = H_0$, then the energy barrier goes to zero, i.e., $\Delta E = 0$, and the minimum condition for magnetization reversal is satisfied. So the particle can change its state.

At first glance, the situation just depicted may seem to be true only for cases when an external field is applied for the purpose of switching the magnetization of the particle. This may be correct when considering only isolated single-domain particles. In the case of an assembly of particles, however, there will be additional fields experienced due to neighboring columns (within a certain distance) even in the absence of an external magnetic field. Consider the diagram illustrated in Figure 2.6, showing an array of nine elongated single domain particles, each with a diameter

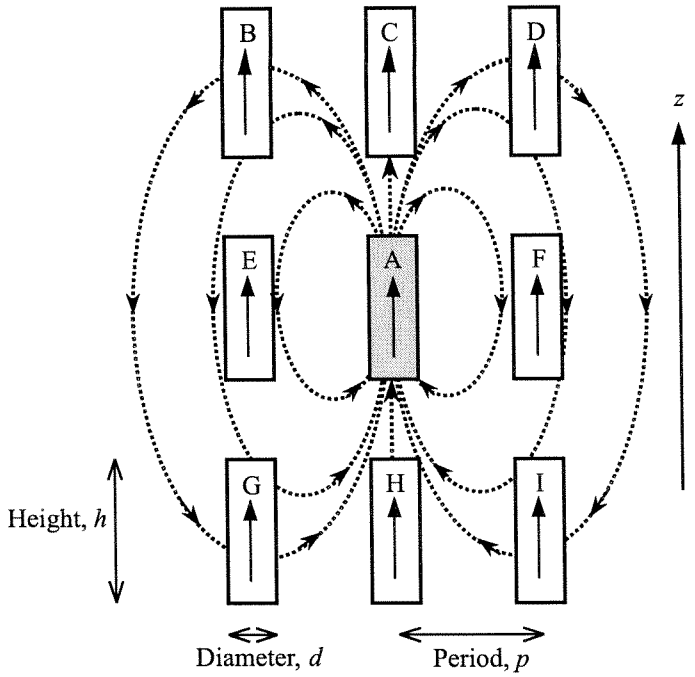

Figure 2.6: Schematic diagram illustrating particle interactions in an array of nine elongated single-domain magnetic particles.

of d and a height of h, arranged in a square pattern with a period of p. We focus our attention on the middle shaded column, labeled as A. Column A, along with its eight neighbors, columns B–I, has been magnetized by an external field in the positive (up) direction along the z-axis. The external field is then removed. The field of column A is now affecting the magnetization of columns E and F in the opposite direction (i.e., in the $-z$ direction) of their initial orientation. As a result, the energy barrier for magnetization reversal of columns E and F will be lower than in the case if each of them were an isolated particle. As for columns C and H, they will experience the opposite effect from column A compared to columns E and F. In other words, the additional field from A will act in the same direction as their initial magnetization, and the energy barrier for switching in columns C and H will increase. As for the second nearest neighbors, columns B, D, G, and H, of column A, the field of A will have a partial effect on them compared to the first nearest neighbors. Note that we have only focused on the influence of one column on its neighbors. In reality, the problem becomes much more complicated when many particles and their

mutual interactions are involved. In the remainder of this section, we will simplify the problem to considering only isolated single-domain particles so as to get an idea of the requirements involved in preventing the onset of the superparamagnetic effect, especially for applications in magnetic recording.

2.2.2 Magnetic anisotropy

One of the properties that strongly affects the magnetization characteristics of a material is its magnetic anisotropy. There are several categories of anisotropy, namely, magnetocrystalline (or crystal), shape, stress and exchange anisotropy, as well as anisotropy induced by magnetic annealing, plastic deformation, and irradiation. Among these, only magnetocrystalline and shape anisotropy will be considered here.

Magnetocrystalline anisotropy is the only anisotropy that is an intrinsic quality to a material. Its origin is mainly associated with spin-orbit coupling. This is due to interactions between the spin and the orbital motion of each electron. The result of this coupling is that when an external field is applied in an attempt to reorient the spin of an electron, its orbital motion also tends to get reoriented. The orbital motion, however, is strongly coupled to the lattice, and therefore counteracts the attempt to rotate the spin axis. The energy required to rotate the spins of a domain away from their easy (preferred) axis is termed the anisotropy energy. This is basically the energy necessary to overcome the spin-orbit interactions. In constrast to spin-spin and orbit-lattice coupling, spin-orbit coupling is relatively weak, and fields of a few hundred oersteds are usually adequate to rotate the spins. The strength of the magnetocrystalline anisotropy in a particular material is determined by the magnitude of the anisotropy constants, K_m. K_m is highly material-dependent and has a typical range of 10^5–10^7 ergs/cm^3. There is no simple method to relate the easy or hard magnetization direction and the arrangement of atoms in the crystal structure. For instance, in iron (body-centered cubic), the direction in which the atoms are most densely packed (i.e., highest atomic density) is <111>, and this is the hard axis. In nickel (face-centered cubic), however, the direction of highest atomic density is

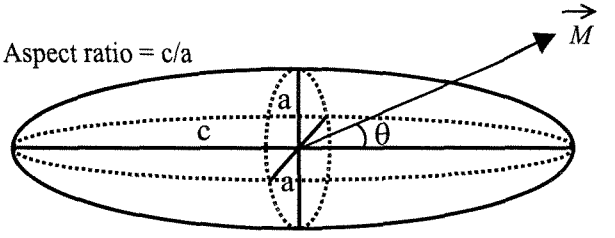

Figure 2.7: Schematic diagram illustrating a prolate spheroid [5].

<110>, and this is the medium-hard axis.

Shape anisotropy, on the other hand, is an extrinsic property. It is largely dependent on the geometry of the specimen and can be readily calculated for shapes such as ellipsoids and cylinders. Consider a prolate spheroid (rod), illustrated in Figure 2.7, with semi-major axis c and semi-minor axis of equal length of a [5]. The magnetostatic energy of the prolate spheroid when it is magnetized to a magnitude of M at an angle θ with respect to the c-axis, is given by [5]:

$$E_{ms} = \frac{1}{2}M^2 N_c + \frac{1}{2}(N_a - N_c)M^2 \sin\theta^2, \tag{2.13}$$

where N_c and N_a are the demagnetizing coefficients along the c- and a-axis, respectively. The shape anisotropy constant, K_s is given by [5]:

$$K_s = \frac{1}{2}(N_a - N_c)M^2. \tag{2.14}$$

If c becomes equal to a, i.e., the specimen becomes spherical, then $K_s = 0$ and shape anisotropy is lost. Thus the aspect ratio (c/a) of the specimen has a strong contribution to the "strength" of the shape anisotropy of a material.

2.2.3 Coercivity versus size in small particles

The coercivity, H_c, of a particle is the reverse field necessary to "coerce" the material back to zero induction after it has reached magnetic saturation in one direction [5]. A more common definition of coercivity is the magnetic field needed to switch the direction of magnetization in a material. The coercivity of magnetic particles has a

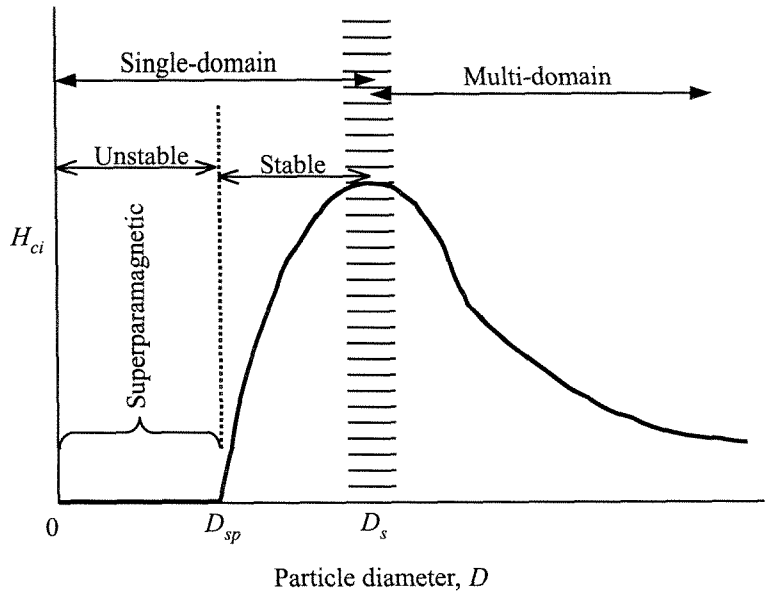

Figure 2.8: Schematic diagram showing the dependence of coercivity on particle diameter [5].

significant dependence on their size. This dependence is illustrated in Figure 2.8 [5]. Starting from a large multi-domain particle (right portion of graph), the coercivity increases as the particle decreases in size, up to a certain diameter, D_s, at which it becomes single domain. Note that the parameter D_s is equivalent to L_s used previously in Equation 2.4. After the coercivity reaches its peak value at D_s, it then starts to decrease as the particle diameter continues to become smaller in the single-domain state. The coercivity finally goes to zero when the particle becomes so small ($D = D_{sp}$) that it is no longer stable. From this point onwards, the particle displays superparamagnetic behavior as its size continues to diminish. The above coercivity versus size relation can be explained by the fact that the mechanism by which a particle reverse its magnetization differs from one size range to the the other. The two general regions are: single-domain and multi-domain.

For multi-domain particles, magnetization changes by domain wall motion. For most materials, the size dependence of coercivity is experimentally found to be given approximately by [5]:

$$H_{ci} = a + \frac{b}{D}, \tag{2.15}$$

where H_{ci} is the intrinsic coercivity of the material, a and b are constants, and D is the diameter of the particle. So for particles with diameter larger then D_s, coercivity is inversely proportional to the lateral size. For single domain particles, there are two separate regimes: stable ($D_{sp} < D < D_s$) and unstable ($0 < D < D_{sp}$). Particles of size D_s or smaller reverse their magnetization by spin rotation, and other mechanisms of rotation can be involved as well. In the size range of ($D_{sp} < D < D_s$), thermal effects are the main cause for the decrease in coercivity along with size, and the following relation is found [5]:

$$H_{ci} = g - \frac{h}{D^{3/2}}, \tag{2.16}$$

where g and h are constants. Below the critical diameter, D_{sp}, the coercivity becomes zero. In this range, thermal effects alone are large enough to spontaneously demagnetize an assembly of particles that has been previously driven to saturation. These particles display superparamagnetic behavior.

2.3 Current storage media, read/write processes and tools

In this section, the current storage format using thin films is described. This is the component of magnetic recording technology that is most vulnerable to the superparamagnetic effect—a phenomenon that the new storage formats are proposing to delay. In the remainder of this section, the concepts behind the read/write processes as well as the recording heads are illustrated and explained. Only the most current commercial heads are described here, as these are the types that are being used for the magnetic characterization procedures in our experiments. It is important that these concepts be clear in the mind of the reader before the magnetic recording data are presented in Chapter 6.

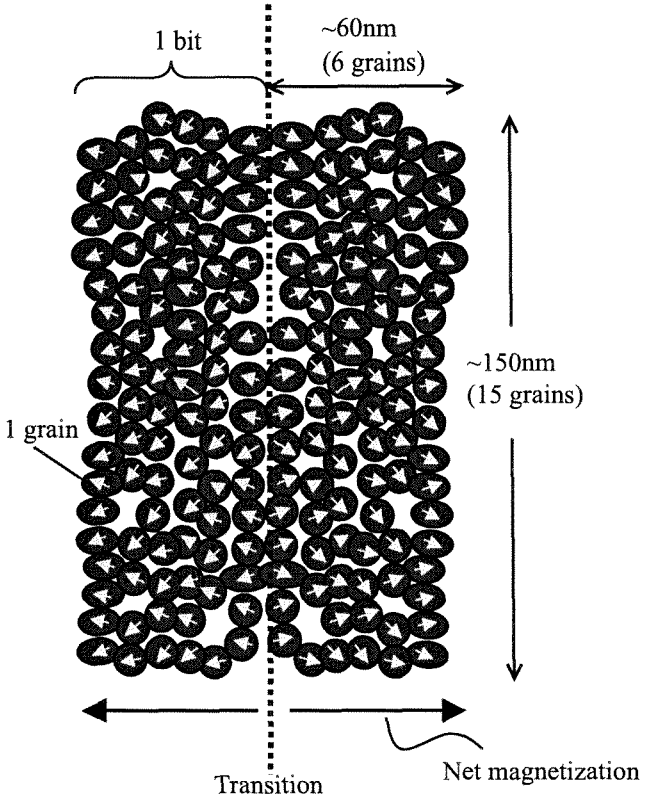

Figure 2.9: An illustration of a conventional thin-film medium consisting of single-domain grains. Each bit of information is represented by tens to hundreds of grains.

2.3.1 Longitudinal thin-film media

Since the late 1980s, thin-film disks have been used for the recording media in hard-disk drives. They are multilayer structures made up of aluminum substrate, amorphous NiP undercoat, underlayer (chromium, NiAl, NiP, etc), magnetic film (e.g., Co-based alloy), overcoat (e.g., carbon), and lubricant [17]. The most important part of this multilayer film is the magnetic recording layer. This layer is comprised of a sputtered, multialloyed thin film that is made up of many grains of sizes much smaller than a recording bit cell. An illustration of a conventional thin-film medium consisting of single-domain grains is shown in Figure 2.9. Patterns of remanent magnetization are formed using a recording transducer along circumferential tracks in the film. Each bit of information is represented by tens to hundreds of grains. In the figure, each grain has an average size of 10nm, so a bit that consists of 15×6 grains

would have a dimension of 150nm×60nm, which gives a bit size of 9000nm^2. Intergranular exchange coupling is minimized by the addition of alloying components, so that the grains are isolated from one another magnetically. It is also preferable that the grains be uniform in size to minimize the variation in their coercivity and other magnetic properties. This is especially important when the individual grain size is very close to the critical dimension at which they may become thermally unstable.

2.3.2 Inductive magnetic writer

There are mainly two categories of inductive heads. One type known as the ring heads; an example is the ferrite heads, in which the magnetic poles are machined, with coils wound around a magnetic pole, and the recording head gaps are formed by glass bonding [17]. The other type is the thin-film heads, in which the magnetic poles and coils are fabricated on a large scale utilizing techniques similar to that in the semiconductor integrated circuit (IC) industry. By the early 1990s, thin-film heads have been used to replace ring heads predominantly in hard-disk drives. A photograph of a commercial inductive write head with an 11-turn coil, which is also used in the recording demonstration in our samples, is shown in Figure 2.10. Thin-film inductive heads can be used as both a reader and a writer. It has been proven, however, that thin-film magnetoresistive read-back heads can offer much larger signal amplitude per trackwidth, which in turn allows higher areal densities for recording [17]. As a result, inductive-write and MR-read dual-element heads have become the desired recording heads for hard-disk drives in the late 1990s. In addition to the large read-back signal amplitude, the dual-element heads also allow independent optimization of the read and write performance since the requirements of each of the functions are not necessarily compatible.

The write transducer is basically a ring-shaped electromagnet that has a gap at the surface facing the medium. This gap in the pole pieces is designed to generate a magnetic field with enough strength in order to record in the magnetic medium to a sufficient depth. When a current representing the signal to be recorded is passed

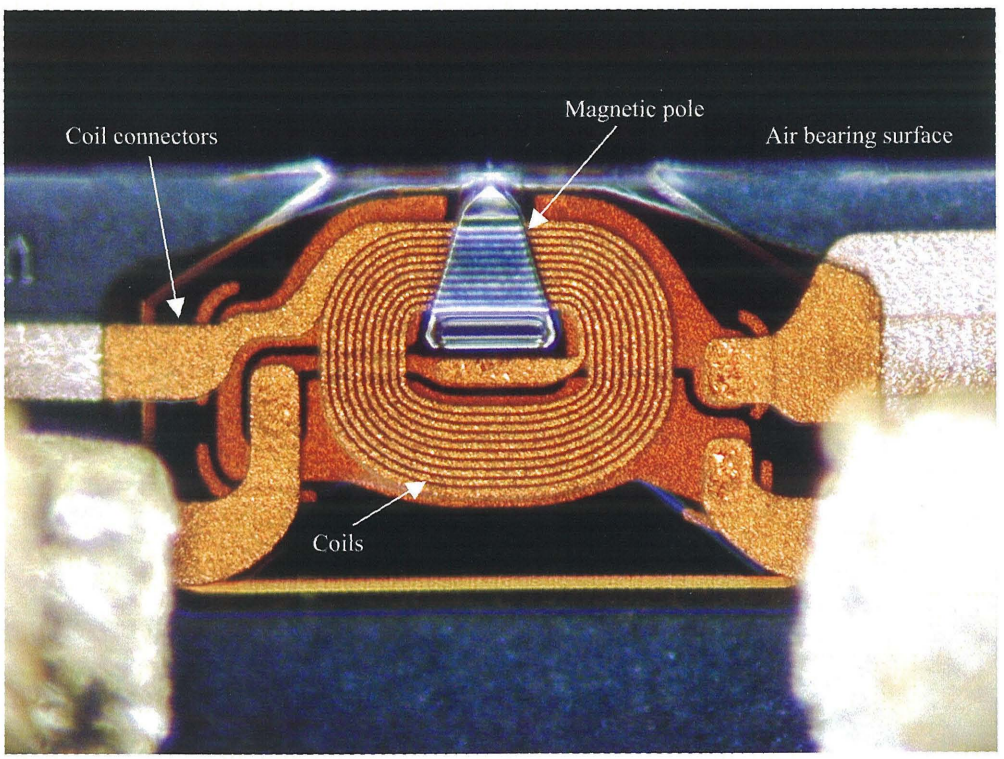

Figure 2.10: Photograph of an 11-turn coil thin-film recording head.

through the coil that is wrapped around the core (or magnetic yoke) of the electromagnet, the fringing field emanating from the gap between the pole tips of the magnet magnetizes the medium directly underneath it. This fringing field has a certain orientation depending on the polarity of the current applied. The magnetization orientation can be determined using a right-hand rule. If the current in the coil is driven in the clockwise direction, then the magnetic field induced would point down into the center of the coil.

A schematic diagram illustrating the writing process in magnetic recording using an inductive transducer is shown in Figure 2.11 [17]. The magnetic medium moves at a constant velocity to the right relative to the recording head, as shown in the figure, while the write transducer records the desired signal by creating remanent magnetization patterns in the medium. The polarity of the current applied is initially chosen to produce a fringing field from the pole gap which magnetizes the medium to the right [Figure 2.11 (a)]. The direction of the current is then switched, which in turn switches the head field direction to the left [Figure 2.11 (b)]. The magnetization of the

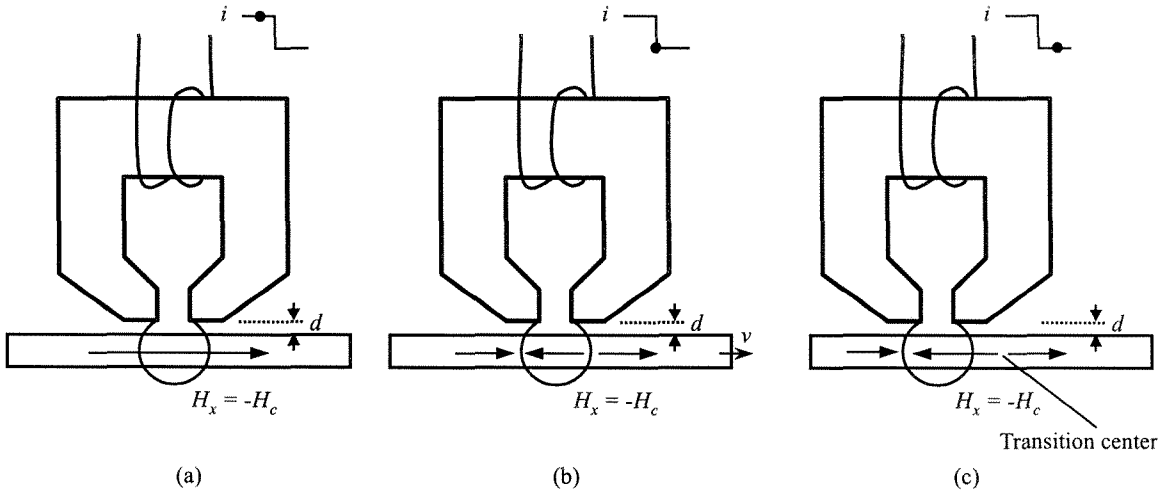

Figure 2.11: Schematic diagram showing the writing process in magnetic recording using an inductive transducer [17].

medium immediately below the head gap, enclosed by the $H_x = -H_c$ contour (also known as the "write bubble"), is now reversed to the left. Hence a magnetic transition is formed at the right (trailing) edge of the bubble. As the medium continues to move to the right, the write bubble travels with the pole gap, and the magnetic transition that was just formed is now outside of the bubble [Figure 2.11 (c)]. This is a written (recorded) magnetic transition in the medium. The transition at the left (leading) edge of the write bubble, however, does not get written, and is continuously erased as the bubble travels to the left (or the medium moving to the right) [17].

2.3.3 Magnetoresistive reader

Up until the 1990s, inductive read-head technology was being used in commercial hard drives. Although these heads were capable of demonstrating recording with an areal density that exceeded what was thought to be possible, they were eventually replaced by the magnetoresistive (MR) heads that have proven to be more promising for future high density magnetic storage. The concept of the MR head was first proposed by Hunt in 1971 [26]. Due to the sophisticated engineering work involved in the design and mass production of the MR head, they were not introduced in hard-disk drives until the 1990s by IBM, and then followed by the rest of the magnetic storage industry.

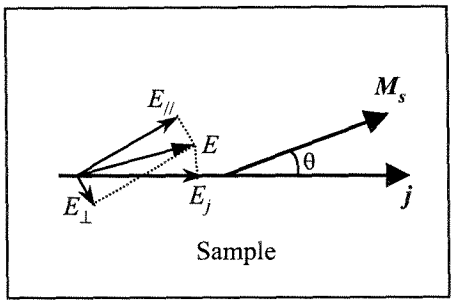

Figure 2.12: Schematic diagram illustrating anisotropic resistivity between the parallel and perpendicular magnetization directions [17].

Some of the advantages of MR heads over the previous inductive heads are increased signal amplitudes and the potential to be extended to the giant magnetoresistance (GMR) technology, which will allow recording in much higher density media in the rapid growing field of magnetic storage.

Due to spin-orbit coupling, some ferromagnetic materials display anisotropic resistivity, which means that their resistivity changes as a function of the orientation between current and magnetization [27]. Consider the illustration in Figure 2.12 [17]. According to Ohm's law, the electric fields parallel and perpendicular to the magnetization can be expressed as follows:

$$E_{||} = \rho_{||} j_{||}, \quad E_\perp = \rho_\perp j_\perp,$$
$$\text{where} \quad j_{||} = j\cos\theta, \quad j_\perp = j\sin\theta.$$

The electric field $\vec{E}$, as shown in the figure, has components in the current direction, represented by:

$$E_j = E_{||}\cos\theta + E_\perp \sin\theta = \rho_{||} j\cos^2\theta + \rho_\perp j \sin^2\theta.$$

The resistivity along the current direction is given by:

$$\rho_j \equiv \frac{E_j}{j} = \rho_{||} j\cos^2\theta + \rho_\perp \sin^2\theta$$
$$= (\rho_{||} - \rho_\perp)\cos^2\theta + \rho_\perp$$

$$= \rho_0 + \Delta\rho_{max}\cos^2\theta, \tag{2.17}$$

$$\text{where} \quad \rho_0 \equiv \rho_\perp, \quad \Delta\rho_{max} \equiv \rho_{||} - \rho_\perp.$$

The value of $\Delta\rho_{max}/\rho_0$ is known as the magnetoresistance (MR) ratio. This ratio is dependent on the thickness as well as the deposition method of the ferromagnetic film. Typical MR ratios of permalloy (~81% Ni, ~19% Fe) deposited on a titanium (Ti) seed layer using ion beam sputtering are 1.2–2.6% with resistivities of 31–21$\mu\Omega$cm for film thickness that range from 50–250Å, respectively [17]. From Equation 2.17, it can be seen that as the magnetization orientation changes with respect to the current direction, the resulting resistivity of an anisotropic MR material will vary according to a cosine function.

A schematic diagram of an MR head and its transfer curve are shown in Figure 2.13 [17]. The MR head is basically a magnetic flux-sensing device that detects fields emanating from the recording medium below it. A transition that has been previously recorded in the medium by the write transducer produces a magnetic field at the surface of the medium. This magnetic field is then averaged over the height, D, of the MR element. If the applied current, I_s, through the MR sensor is kept constant, then any change in the magnetic field direction of the medium will result in a change in the MR resistance, which is measured as a change in voltage across the element. As seen in Figure 2.13 (b), the slope of the MR transfer curve is zero when the magnetic field is zero. So if the MR sensor is operating at $H = 0$, then any change in either direction of the magnetic field will result in an identical change in the MR ratio (assuming the amplitude of the field is constant), which is then translated to an equivalent change in the MR read-back voltage. Therefore, a bias field of H_b is applied to the MR element in order to shift its operating point from $H = 0$ to a location where the slope of the transfer curve is at a maximum. From Equation 2.17, the MR resistivity, ρ, is related to the angle, θ, between the magnetization and current direction by the equation:

$$\rho = \rho_0 + \Delta\rho_{max}\cos^2\theta.$$

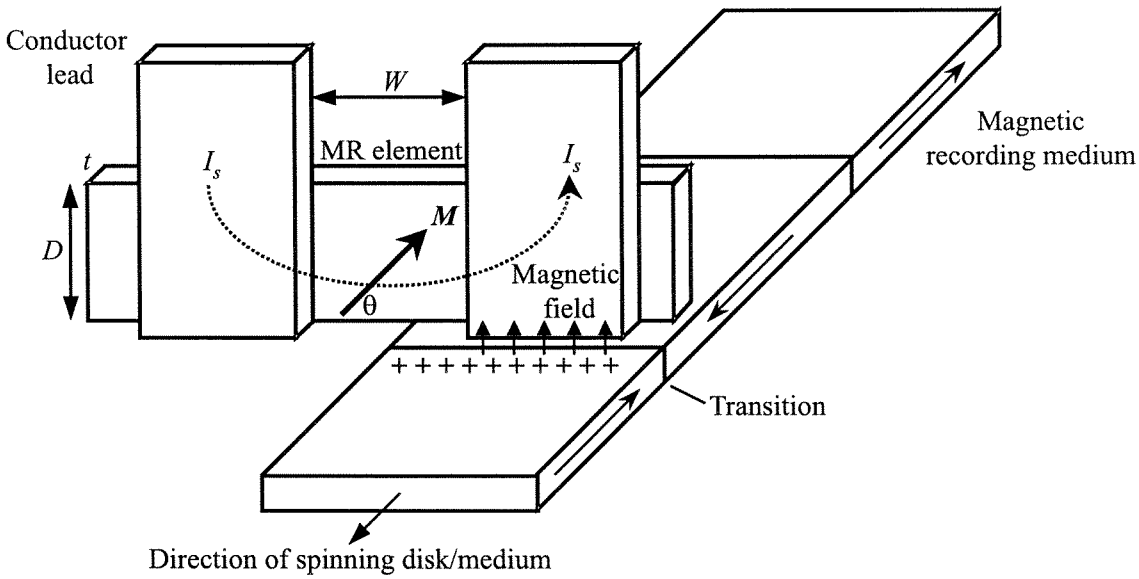

(a)

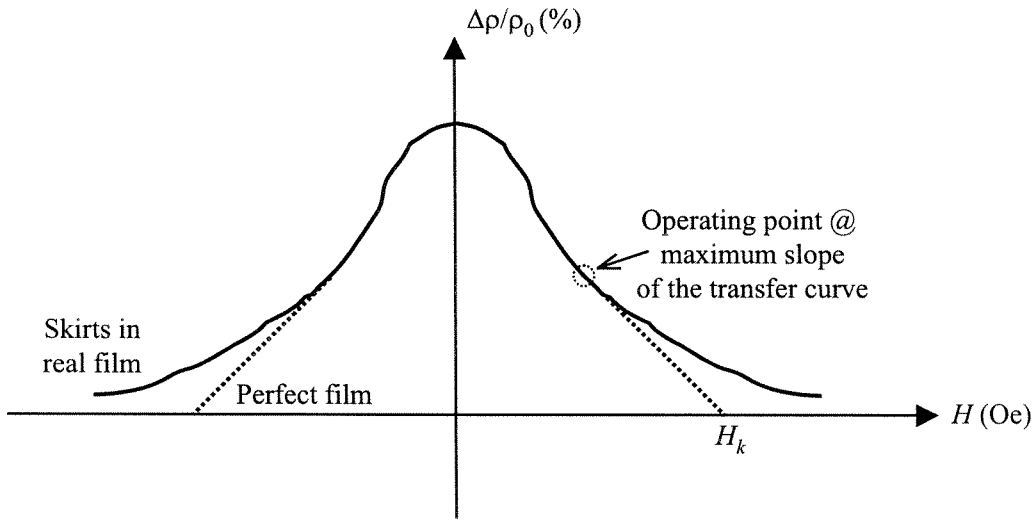

(b)

Figure 2.13: Schematic diagram showing the MR read transducer (a) and its transfer curve (b) [17].

Taking the derivative of the resistivity with respect to the angle gives us:

$$\frac{\partial \rho}{\partial \theta} = -\Delta\rho_{max} \sin^2 \theta. \tag{2.18}$$

From Equation 2.18, we see that the bias angle should be $\theta_0 = 45°$ for the slope of the transfer curve to be maximized. Note that the MR head shown in Figure 2.13 (a) is an unshielded version. In order to prevent the MR head from detecting magnetic fields from neighboring transitions, high-permeability shields are needed on both sides of the MR element.

Assuming that the MR element is biased to its optimum operating point, this magnetization direction will be rotated when it senses the emanating field from the recording medium. This rotation results in a change in the MR ratio, which is then measured as a corresponding change in the MR voltage (given the sense current is kept constant across the element). If the MR element is biased at an angle, θ_0, then the read-back voltage is [17]:

$$V(\overline{x}) = I\Delta R = JW\Delta\rho_{max}(\cos^2 \theta - \cos^2 \theta_0), \tag{2.19}$$

where W is the length of the MR element (trackwidth) defined by the conductor leads, $\overline{x} = vt$ is the relative head-medium position, and J is the current density (this is assumed to be uniform across the sensor). For conventional thin-film media, a typical MR read-back voltage on the order of 200μV is expected for track sizes of $\sim 2\mu$m.

When examining the transfer curve in Figure 2.13 (b), we see that it is intrinsically nonlinear. So one needs to take precaution when operating an MR element, and should avoid driving it into saturation, which would shift the operating point outside of the small dynamic range where the transfer curve is linear. One of the results of MR nonlinearity is that two almost identical magnetic fields (same amplitude but opposite in orientation) sensed from the recording medium may result in different read-back voltages measured. Another characteristic of the MR element that needs

to be taken in account is its resistivity as a function of temperature. The magnitude of the sense current through the transducer would determine the amount of Joule heating resulted. Excessive Joule heating as well as any thermal asperity (instantaneous temperature variation) in the MR element can give rise to distorted read-back voltage waveforms. Similar to most electronics, the MR sensor is easily damaged by electrostatic discharge. To prevent inconsistency in the measurement, the recording head should be handled with properly grounded operators, as well as any materials or equipment that may be in contact with them.

2.3.4 Giant magnetoresistive read head

After the introduction of the magnetoresistance effect, researchers started to look for sensor materials that would give a much more significant change in the MR ratio when the sensor experiences an external magnetic field. This material, named giant magnetoresistance (GMR) material, was first discovered in 1988 by Baibich et al. on their work on GMR effect in Fe/Cr multilayers [28]. The type of GMR structure investigated by Baibich et al. consists of a sandwich of magnetic and nonmagnetic metal materials. The two magnetic layers (separated by the nonmagnetic layer) are oriented antiparallel (an antiferromagnetic state) to each other when there is no external magnetic field. When the GMR multilayer experiences an external field that is strong enough to align the two magnetic layers such that they are parallel to each other (a ferromagnetic state), then the resistance across the multilayer material will drop (up to a factor of 2). This drop in resistance in the ferromagnetic state is mainly due to a decrease in spin-dependent scattering at the magnetic/nonmagnetic metal interface as well as within the ferromagnetic layers.

To find an expression for the GMR ratio, we take into account the maximum difference between the resistance of the antiferromagnetic and ferromagnetic state, as well as the minimum resistance of the ferromagnetic state, and result in the following:

$$\text{GMR ratio} \equiv \frac{R_{\uparrow\downarrow} - R_{\uparrow\uparrow}}{R_{\uparrow\uparrow}}, \tag{2.20}$$

where $R_{\uparrow\uparrow}$ is the resistance across the GMR multilayer when the magnetization of the two ferromagnetic layers are parallel, and $R_{\uparrow\downarrow}$ is the resistance when the magnetizations are antiparallel [17].

Since the discovery of the GMR effect, there have been numerous reports on various combinations of ferromagnetic and nonmagnetic metal multilayers that display extraordinarily large GMR ratios. One example is in a $Co_{95}Fe_5$/Cu multilayer reported by Parkin [29], where GMR ratios of ~110% at 295 K and ~220% at 4.2 K have been observed. Despite the large GMR ratios observed, the large saturation field necessary to overcome the antiferromagnetic coupling between the two magnetic layers makes the GMR multilayer insensitive to small magnetic fields. These multilayer structures are also difficult to implement into actual magnetic recording heads. With these factors considered, a new type of GMR structure consisting of various combinations of ferromagnetic/nonmagnetic/ferromagnetic/antiferromagnetic materials is being investigated. These GMR sandwiches are also known as "spin valves". A schematic diagram showing a cross-sectional view of a bottom spin-valve structure, a spin-valve GMR read head, as well as its magnetic hysteresis loop and transfer curves are shown in Figure 2.14.

An example of the materials used in a bottom spin-valve structure such as the one illustrated in Figure 2.14 (a) is NiFe/Cu/NiFe/FeMn, starting from the ferromagnetic layer on top. The purpose of the antiferromagnetic layer is to pin the magnetization direction of the bottom ferromagnetic layer by exchange anisotropy [30]. Since the interactions between the two ferromagnetic layers are much weaker than that found in the GMR multilayer, the top ferromagnetic layer can respond to an external magnetic field with a magnitude as small as ~6Oe. Note that a top spin-valve structure would have the antiferromagnetic layer at the top, followed by two ferromagnetic layers with a nonmagnetic metal layer sandwiched between them. Its working principles are similar to that of a bottom spin-valve structure. A schematic cross sectional diagram of a spin-valve GMR read head design with an exchange-pinned bottom ferromagnetic layer and longitudinal hard bias is illustrated in Figure 2.14 (b). In this case, the pinned layer is at a 90° with respect to the top free ferromagnetic layer, which is

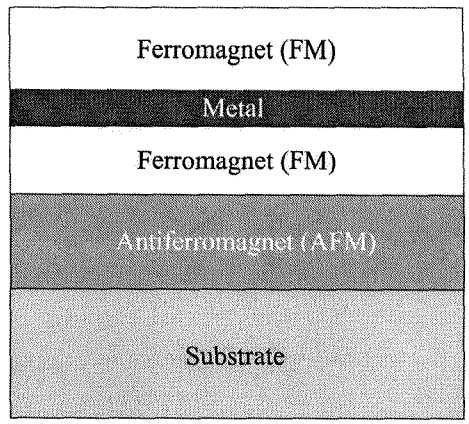

(a)

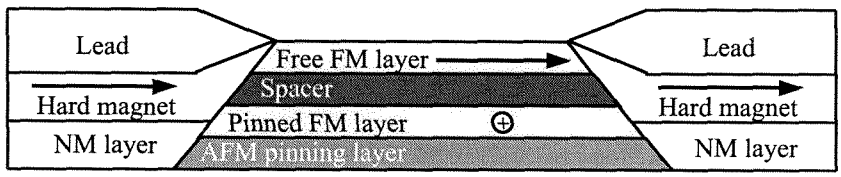

(b)

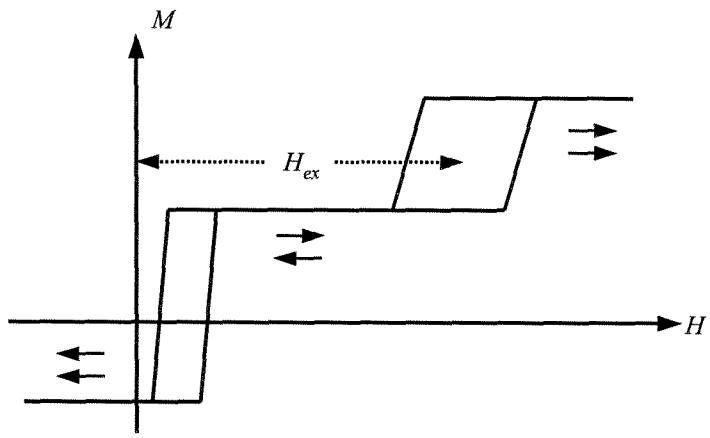

(c)

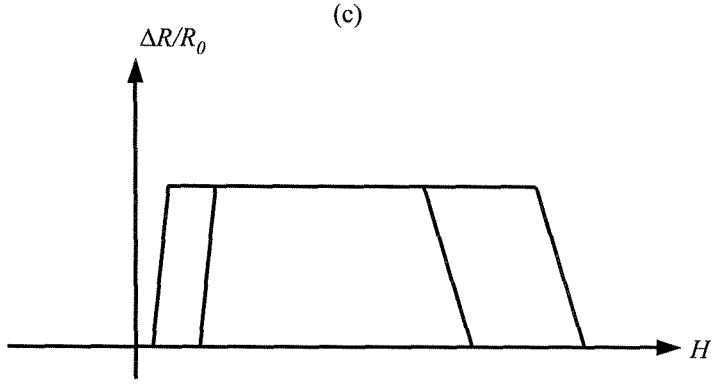

(d)

Figure 2.14: A schematic diagram showing the cross-sectional view of a bottom spin-valve structure (a), a spin-valve GMR read head (b), as well as its magnetic hysteresis loop (c), and transfer curves (d) [17].

biased in the longitudinal direction by the hard magnets on both sides of the spin-valve sandwich. The dynamic range in this type of configuration (from -90° to +90°) is much larger compared to the previous type of AMR head (from 0° to 90°, if biased at 45°), as shown in Figure 2.13.

The magnetic hysteresis loop and MR transfer curve of spin valves are shown in Figures 2.14 (c) and (d), respectively. The hysteresis loop near the origin is associated with the switching of the top free ferromagnetic layer, while the one at a higher field is associated with the switching of the bottom pinned layer. The resistance of the spin valve is at its maximum when the top and bottom ferromagnetic layers are antiparallel to each other, and the minimum occurs when both layers are parallel. The GMR ratio of a spin valve can be expressed as [17]:

$$\frac{\Delta R}{R_0} = \frac{\Delta R_{max}}{R_0}[\frac{1-\cos(\theta_2-\theta_1)}{2}], \tag{2.21}$$

where θ_1 and θ_2 are the magnetization orientation angles of the pinned and free ferromagnetic layers in the spin valve structure, respectively. In the initial state as shown in Figure 2.14, $\theta_1 = 0°$ and $\theta_2 = 90°$, such that $\theta_2 - \theta_1 = 90°$ and the GMR ratio is half of its maximum value.

2.4 Single-domain particles suitable for magnetic recording

An important parameter for any storage medium is its ability to retain the recorded information, i.e., magnetization direction of each bit, for a desired amount of time. Hard drives today typically have a storage time of at least 10 years. However, if thermal fluctuation causes spontaneous magnetization reversal to occur, then part or all of the stored information will be lost. According to Wang et al. [17], the probability of magnetization reversal per unit time can be approximated by the Arrhenius

equation:

$$f = f_0 \exp(-\frac{\Delta E}{k_B T}), \tag{2.22}$$

where ΔE is the energy barrier, associated with the switching process, and f_0 is the "attempt frequency" to cross the barrier. The estimated value of f_0 is 10^9 Hz, and is calculated from the precession frequency of magnetic materials and spin-lattice relaxation time. The Arrhenius equation indicates that the mean time for the spontaneous magnetization reversal to occur is [17]:

$$\tau = \tau_0 \exp(\frac{\Delta E}{k_B T}), \tag{2.23}$$

where $\tau_0 = 1/f_0 = 10^{-9}$s.

In the absence of an applied magnetic field, the energy barrier of a prolate spheroidal particle is $\Delta E = KV$. As Wang et al. [17] suggested as an example, in order to retain one bit of stored information in a spheroidal particle for $t > 10$ years (3×10^8s), then $f < 3.33 \times 10^{-9}$Hz. This means that $\Delta E > 40 k_B T$, or $V > 40 k_B T/K$. For a typical thin-film magnetic recording medium, with an anisotropy constant of approximately 2×10^6 ergs/cm^3, $k_B T = 4.14 \times 10^{-14}$ erg at room temperature, the particle volume should be greater than 828 nm^3. Assuming a cubic grain, this implies that the individual grain should be larger than ~9nm in each dimension. This is known as the superparamagnetic limit in the magnetic recording industry. Nonetheless there are variations to the exact value of this limit due to differences in the anisotropy constant and other material and engineering parameters of the medium.

Another criterion that needs to be taken into account when considering the superparamagnetic limit is the thermal decay of the magnetization of the grains in the media due to opposing fields such as those from adjacent transitions. Consider a collection of small particles. The probability of the magnetization not having hopped the energy barrier is [17]:

$$P(t) = e^{-t/\tau}, \tag{2.24}$$

whereas the probability of the magnetization having hopped the barrier is:

$$1 - P(t) = 1 - e^{-t/\tau}, \tag{2.25}$$

So the magnetization of the array of particles is expected to vary as:

$$M(t) = M_0 e^{-t/\tau} + M_\infty (1 - e^{-t/\tau}), \tag{2.26}$$

where M_0 and M_∞ are the initial and final saturated magnetization, respectively. With an opposing field of $M_\infty = -M_0$, the magnetization of the array will decay as [17]:

$$M(t) = M_0[2\exp(-t/\tau) - 1] = M_0[2\exp(-f_0 t \exp(-\frac{\Delta E}{k_B T})) - 1]. \tag{2.27}$$

The "exponential of exponential" term in Equation 2.27 indicates that the magnetization decay is extremely sensitive to the energy barrier and any thermal fluctuations. The former implies that the variation in grain size and anisotropy in the media will have a drastic effect on the thermal decay rate of the stored information. The numerical distribution of these two parameters is more evident as the grain size decreases to accomodate for ultrahigh density requirements in the media. The result is that the magnetization decay resembles a superposition of exponential decays with different rates due to the grain volume distribution. This is a very serious issue that needs to be addressed as the areal density continues to rise. In spite of all the above challenges, however, many researchers still believe that the oncoming superparamagnetic limit using conventional thin films can be further extended to around 100–150Gbits/in.^{2}.

Chapter 3 Storage formats for 100Gbits/in.^{2} and beyond

The individual grain size in the conventional thin-film media is already approaching the critical volume for the onset of the superparamagnetic effect. As the demand for higher areal density continues to increase, researchers in the magnetic industry are continuously searching for solutions to achieve areal densities of 100Gbits/in.^{2} and beyond.

3.1 Conventional media with modifications

With so many resources already invested into the development of conventional storage media utilizing thin films, and with the unavoidable lag time involved when transferring a laboratory demonstration to an actual commercial product, it is understandable that the magnetic recording industry continues to push the storage capacity of thin-film media to its limit. To satisfy the demand for higher areal density, a straight forward strategy is direct miniaturization.

The immediate target for scaling is the magnetic grains that make up each bit in the storage medium. As the grains have already been shrunk to sizes that are close to the limit at which superparamagnetic behavior may be triggered, researchers are shifting gears toward improving the anisotropy constant, K, of the ferromagnetic material instead. With an increased K, the coercivity, H_c, of the media will be strengthened as well, following the relation: $H_c = 2K/M_s$ [5]. Another parameter of the storage medium that is being heavily researched on is the product of thickness, δ, and remanence, M_r, of the magnetic film. The smaller the $M_r\delta$ product, the sharper the transition between regions of opposite magnetization, and higher density along each track becomes possible. The transition parameter, a, which is characteristic of

the width of a transition, is defined as $1/\pi$ times the minimum nonoverlapping bit size, and is given approximately by $[(M_r\delta/0.8\pi H_c)(d+\delta/2)]^{0.5}$, where d is the head-medium spacing [31, 12]. H_c cannot be increased indefinitely, however, since the recording head must be capable of producing a large enough field to write the medium. Current media have $H_c > 2500$Oe. In addition, $M_r\delta$ cannot be scaled down arbitrarily since there is a certain threshold signal-to-noise ratio required in the read-back process for accurate data retrieval. At an areal recording density of ~10Gbits/in.^{2}, the $M_r\delta$ product is calculated to be $\sim 0.5\times10^{-3}$emu/cm^3 with a medium thickness of ~15nm [17]. It is now at the regime where continual decrease of film thickness is an increasingly challenging task, as the coercivity of the film drops off drastically with the onset of the superparamagnetic effect fast approaching.

Alongside all the development work in improving the media for higher areal density storage, the industry has also diversified its efforts to the other aspects of the magnetic recording process. With smaller bits holding the stored information in the media, narrower write heads are required, which have so far been achieved by physical trimming using focused ion beam etching. Smaller read sensors are also preferable, but they are a rather complex sandwich of thin film elements, and pose a more difficult manufacturing problem for the reduction in their size. Packing in a larger number of tracks per square inch on a disk platter will also enforce a more stringent positioning requirement on the head driven by actuators. Lastly, smaller bits in thinner tracks will result in weaker signals for the read sensor. New algorithms will become necessary to facilitate the accurate retrieval of the stored data based on a much smaller signal than what is available from current media. Nevertheless, many experts in the industry believe that the ongoing work on all the above aspects should allow the current thin-film media to reach 100 to 150Gbits/in.^{2} recording densities.

3.2 Patterned media

One of the several proposed alternative solutions to postpone the superparamagnetic limit is patterned media [32, 33]. The idea of patterned media actually dates back to

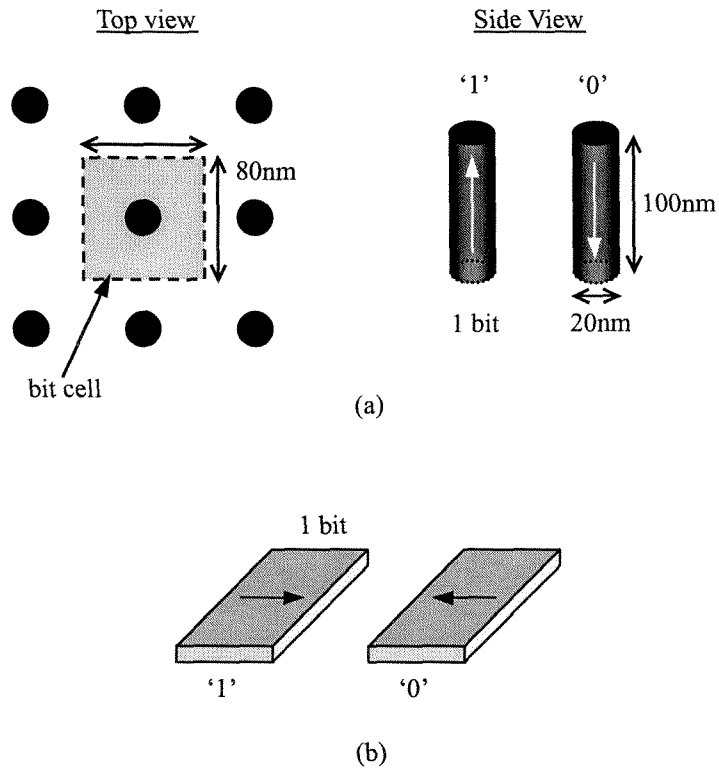

Figure 3.1: An illustration of (a) perpendicular and (b) longitudinal patterned media format. In both cases, each magnetic column or island represents one bit of stored information.

1963 when Shew [34] proposed to physically etch discrete tracks in order to improve head positioning capabilities. As for the rewritable patterned magnetic media with a single-bit-per-island format, research and discussions have only been active in the last decade or so, and especially in the last few years when the magnetic recording industry has been expeditiously searching for a solution for the oncoming superparamagnetic limit.

A patterned medium is comprised of a periodic array of discrete magnetic structures that are defined lithographically on a substrate. Researchers have investigated in both the perpendicular and longitudinal recording schemes, shown in Figure 3.1. The main advantage of a patterned medium is that it has the potential to delay the superparamagnetic limit by several orders of magnitude. In a conventional thin-film medium, each bit contains $\sim$100 magnetic grains that are exchange-decoupled from one another in order to provide a certain signal-to-noise (SNR) ratio. However, in

patterned media where exchange coupling noise is eliminated, each bit can contain just one or more exchange-coupled grains, and still achieve a reasonable SNR. Assuming the same magnetic material being used for the grain or bit, patterned media are then capable of achieving areal densities of $\sim$100 times or more than conventional media. Other advantages of patterned media include the reduction of medium noise, as well as the elimination of nonlinear transition shift and track edge noise.

In the perpendicular patterned media format [as illustrated in Figure 3.1 (a)], each element or column is a single magnetic domain, with its magnetic anisotropy axis perpendicular to the plane of the substrate. The top view of a square array of 3×3 columns is shown on the left side of Figure 3.1 (a), where each column has a diameter of 20nm and height of 100nm (5:1 aspect ratio), with a spacing of 80nm between the columns. This configuration is equivalent to an areal density of 100Gbits/in.^{2}. The magnetization of each column in this perpendicular format should point only in one of the two directions [either up or down, as indicated in the columns on the right portion of the figure in (a)] at remanence. This magnetization orientation represents the stored binary data of either a "1" or "0" in each column or bit.

The same principle holds true for the longitudinal patterned media format [as shown in Figure 3.1 (b)]. The difference is that the magnetic anisotropy axis for the longitudinal islands should be parallel to the plane of the film. Note that the magnetization is aligned along the short axis, and not the long axis, parallel to the surface of the thin magnetic islands. The shape anisotropy along the long axis of these small islands is quite minute so that additional anisotropies such as stress anisotropy can be induced to align the magnetization along the short axis [35]. Prototype longitudinal patterned media have been reported by various researchers (see for example, References [36, 37]), where shape and magnetocrystalline anisotropies have been used to achieve in-plane magnetization in the individual patterned islands.

Compared to the perpendicular format, however, the in-plane elongation of magnetic islands is more costly in terms of surface area occupied on a disk, and will pose an upper limit in the bit packing density sooner than what is predicted in the perpendicular bit arrangement. Also, if in-plane magnetocrystalline anisotropy is required,

there will be a more limited selection of magnetic materials that are suitable, since the material may need to have a particular epitaxial relationship with the substrate during the deposition process in order to satisfy the anisotropy requirements. Additional requirements on the magnetic material properties may be necessary if in-plane magnetoelastic anisotropy is employed. Magnetic islands in the parallel format typically have smaller volumes, and there are less mutual interactions among neighboring bits, but require higher anisotropy to enable thermal stability compared to the perpendicular represenatation [31]. The focus of this thesis will be on the perpendicular version of the patterned media approach.

3.2.1 Perpendicular patterned media design

Utilizing the perpendicular patterned media format, we envision that the recording scheme will still consist of a spinning disk and a slider, as shown in Figure 3.2. The disk itself will be made up of individual magnetic columns, which are oriented perpendicular to the surface, and are isolated from one another by a non-magnetic substrate. Considering that the distance between the slider and the medium is already down to ~20nm in current media, the columns should be in an embedded form if possible so as to minimize any accidental crash of the recording head into the medium and destroying the stored data. In this format, each column represents a "0" or "1" logic when its magnetization is oriented either parallel or antiparallel to the long axis of the particle. The slider will host a writer, which can be an inductive element, and a reader, which can be a magnetoresistive or spin-valve transducer, or whatever the current read/write technology may offer. A diagram of an inductive write element is shown in the upper left corner of Figure 3.2. For longitudinal thin-film media, the parallel component of the fringing field (shown in green arrows in Figure 3.2) is used for recording information in the medium. In our perpendicular patterned media samples, however, the perpendicular component of this fringing field (shown in red arrows in Figure 3.2) is used instead.

In the design of perpendicular patterned media, parameters such as the column

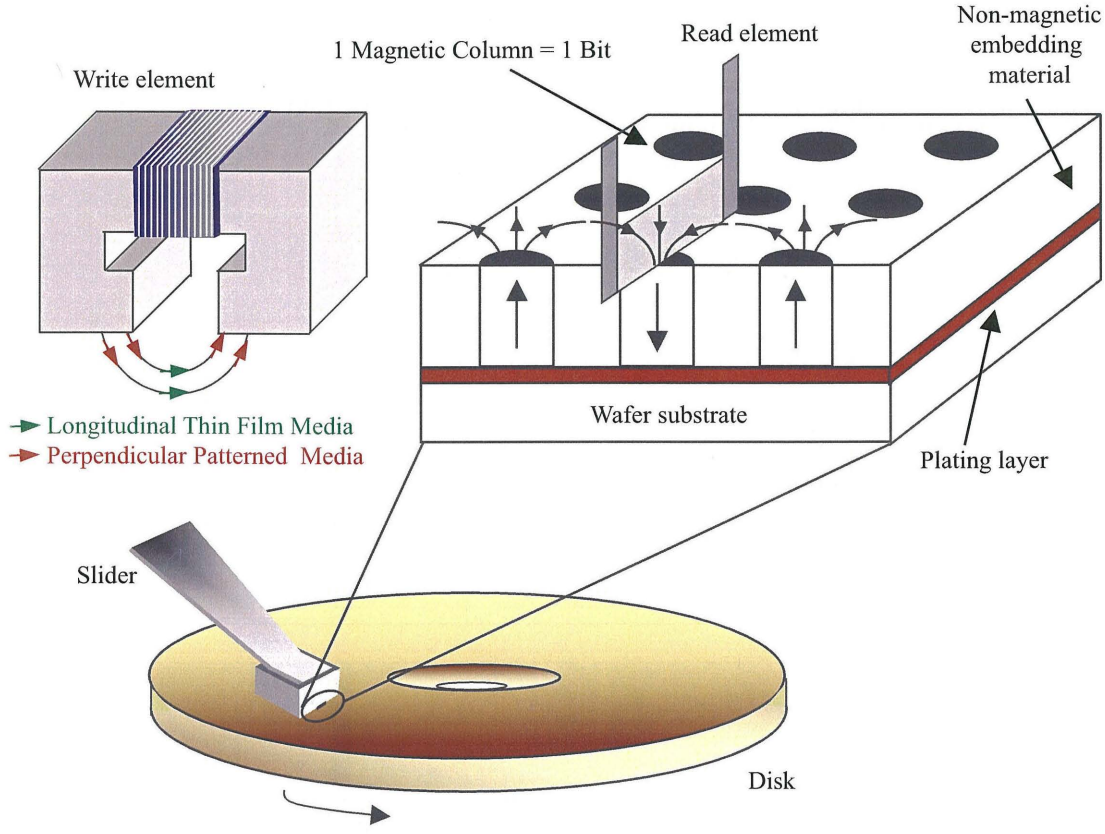

Figure 3.2: Schematic diagram of the perpendicular patterned media recording scheme

geometry, periodicity, and the material selection are determined so that the magnetic anisotropy and saturation moment result in interaction fields from neighboring columns that are insufficient to switch the magnetization of the column of interest. In other words, the column needs to be strong enough magnetically to resist against thermal switching which corrupts the stored information.

We now consider this mutual interaction field in a square array of columns, with diameter d, height h, and periodicity p. An illustration of the column arrangement can be found in Figure 2.6 in the previous chapter. Following a similar argument as in Reference [31], we approximate each particle as a magnetic dipole [5, 38]. If each particle has a volume V, then its moment is $m = M_s V$, and it exerts a field of $H_i = m/p^3$ on its neighboring column. From this relation, we see that the interaction field increases as the column diameter and the aspect ratio. This field is also dependent on the saturation moment, M_s, characteristic of the specific material used for the column. A set of calculated values of the interaction fields, H_i, from a neighboring Ni column of diameter d, height $h = ad$, with periodicity $p = d/b$, is tabulated in Figure 3.3 (a). Here, the variables, a and b, represent the aspect ratio and the ratio of diameter and period of a column, respectively. The simplified expression for H_i in terms of a and b is: $H_i = ab^3(M_s\pi/4)$. A plot of the calculated interaction fields, H_i, versus b for various aspect ratios (1:1 up to 6:1) is shown in Figure 3.3 (b). It is evident from the cubic relation between H_i and b that the effect of variations in the column diameter with respect to the spacing between the columns is much more dramatic than that of the aspect ratio a (linear scaling). For a 5:1 aspect ratio Ni column, if the column is 20nm in diameter ($a = 5$) with a periodicity of 100nm ($b = 0.2$), then according to the table in Figure 3.3 (a), an interaction field of ~15Oe is experienced from its neighbor. If the column is now 50nm in diameter ($a = 5, b = 0.5$), then the interaction field increases by more than an order of magnitude to ~238Oe. These values of the interaction field decrease to ~6 and 95Oe, respectively, if the aspect ratio is reduced to 2:1 instead. The array of columns should be designed such that the interaction fields experienced by a single column from all of its surrounding neighbors (which is approximated to be $9H_i$ for a square lattice) do not exceed the switching field of the

Calculated interaction fields, H_i, from a neighboring Ni column of diameter d, height $h = a\,d$; period $p = d/b$

	a=1	a=2	a=3	a=4	a=5	a=6
b	*Hi* (Oe)	*Hi* (Oe)	*Hi* (Oe)	*Hi* (Oe)	*Hi* (Oe)	*Hi* (Oe)
0.1	0.38	0.76	1.14	1.52	1.90	2.28
0.2	3.04	6.08	9.13	12.17	15.21	18.25
0.3	10.27	20.53	30.80	41.06	51.33	61.60
0.4	24.33	48.67	73.00	97.34	121.67	146.00
0.5	47.53	95.05	142.58	190.10	237.63	285.16
0.6	82.13	164.25	246.38	328.50	410.63	492.76
0.7	130.41	260.82	391.23	521.64	652.05	782.46
0.8	194.67	389.34	584.01	778.68	973.35	1168.02
0.9	277.17	554.34	831.51	1108.68	1385.85	1663.02

Saturation moment, M_s = 484 emu/cm^3

(a)

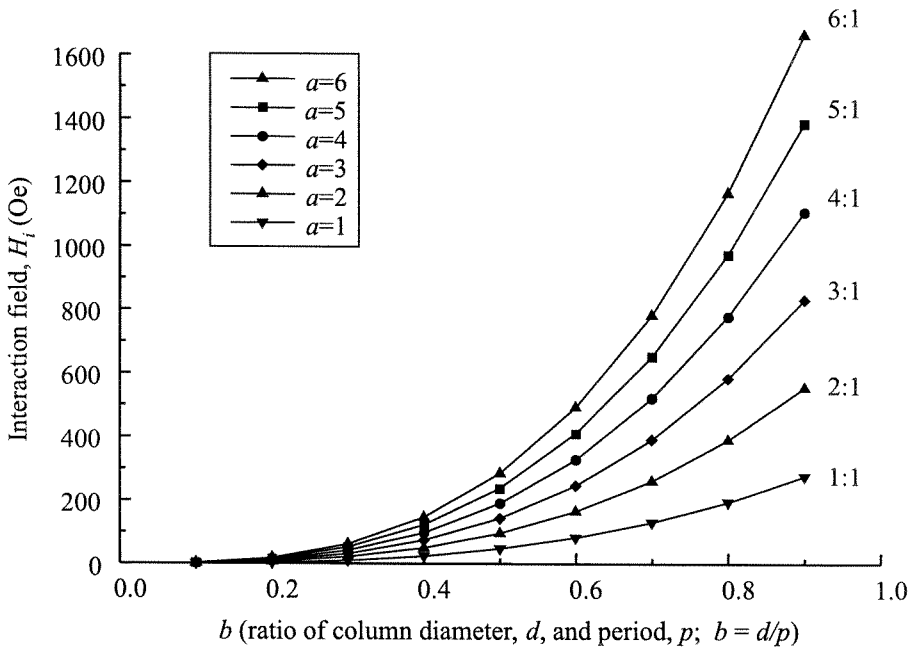

(b)

Figure 3.3: (a) Calculated interaction fields from a neighboring Ni column, approximating each Ni column as a magnetic dipole. (b) Plot of interaction field versus the ratio of diameter and period for different aspect ratio.

column itself.

In addition to the mutual interaction fields among columns, the switching field of an individual column is also influenced by the total anisotropy K, the switching mechanism, and on the angle of the applied magnetic field with respect to the anisotropy axis of the column [31]. The main contributors to K are shape anisotropy K_s and magnetocrystalline anisotropy K_m. Shape anisotropy is geometry-dependent, and is proportional to M_s^2, given by Equation 2.14 for ellipsoids or cylinders. For a 5:1 aspect ratio ellipsoid of pure Ni or Co, K_s would have values of $\sim 6\times10^5$ and 5×10^6 erg/cm^3, assuming M_s of 484 and 1422 emu/cm^3, respectively. Whereas for a 2:1 aspect ratio column, these values would decrease to $\sim 3.5\times10^5$ and 3×10^6erg/cm^3. As mentioned in the previous chapter, K_m is dependent on the material of the column, and has typical values of 10^5–10^7erg/cm^3. Assuming that magnetization reversal occurs coherently, i.e., the spins of all the atoms within the particle remain parallel to one another throughout the rotation [21], elongated particles with the applied field aligned parallel to their anisotropy axis have switching fields of $H_{sw} = 2K/M_s$. For Ni or Co ellipsoids with a 5:1 aspect ratio, the values of H_{sw} are $\sim$2520 and 7450Oe, respectively. These numbers drop to $\sim$1440 and 4220Oe for a 2:1 aspect ratio column.

One might imagine that these switching fields should be more than sufficient to prevent a column from becoming unstable due to interactions from its neighboring columns. In practice, however, incoherent rotation can be the operative reversal mechanism instead. In this case, the spins of the atoms in the column do not all rotate in unison, as in coherent reversal. Curling, which is one of the incoherent rotation modes, has been investigated both analytically [39, 40] as well as using micromagnetic modeling [41, 42] to simulate switching behaviors. The spins are not parallel to one another during a curling reversal, therefore no magnetostatic energy is involved, and the energy barrier is entirely exchange energy [5]. Whereas for coherent rotation, free poles are formed since the spins within a particle are always parallel during reversal, and the barrier is due to magnetostatic energy, not exchange energy.

One of the conclusions drawn by researchers on reversal mechanisms is that small particles tend to switch coherently while large particles rotate by curling. The critical

dimension that distinguish the two modes of reversal is called the exchange length, λ_{ex}, which has values of 10–20nm for common magnetic materials [43]. In addition to the the particle size relative to the exchange length, there are also external non-uniform fields encountered in magnetic recording which will promote incoherent switching. So we do not expect that particles in perpendicular patterned media would switch coherently, unless they are extremely homogeneous and their sizes are small compared to the exchange length. Calculations by various groups show that the coercivity of a particle in the curling mode is remarkably size-dependent. As the diameter of a particle becomes larger, the mean angle between adjacent spins averaged over the cross section of the particle is less, and the exchange energy per unit volume is smaller. This gives rise to decreasing coercivity as the particle diameter increases [5].

As a result, the switching field of particles that reverse by incoherent rotation is highly dependent on the size of the particles in relation to the exchange length. As Ross et al. [31] suggested as examples, a 40nm diameter Ni pillar has a switching field of $H_{sw} = 900$Oe, but at diameters of 150–1000nm, the switching field rapidly decreases to $H_{sw} = 450$–100Oe [44, 45]. For Co bars, H_{sw} decreases from 3000 to 1000Oe as the diameter increases from 30 to 100nm [37]. For the 150–230nm diameter Ni columns that we will mainly be investigating in our perpendicular patterned media samples, we expect that they would reverse incoherently, and have switching fields of 100–300Oe, approximating from the data taken by O'Barr et al. [45].

3.3 Alternative storage formats

So far the primary focus up to this section has been on magnetic recording, and hard-disk drives in particular. Within magnetic storage, there are many variations such as magnetic floppy disk drives, magnetic tape drives, and removable hard drives. Outside of magnetics, there are even more avenues of information storage solutions that are under development. Among them are optical disk recording [46], near-field optical recording [47], holographic storage [48], semiconductor flash memory [49], magnetic random access memory (RAM) [50], scanning probe recording [51], electron

trapping optical memory (ETOM) [52], etc.

One of the alternatives that has been under rapid research and development during the last five years (and perhaps production in the coming year) is a hybrid approach that supplements the magnetic-disk drive with optical technology [1]. This approach is a variation of magneto-optical technology, in which a laser beam heats a tiny spot on a magnetic disk so that information can be written there. In this technique, a solid-immersion lens (SIL) is used to focus the laser beam to a spot smaller than a micron in the lateral dimension, allowing the bits to be written onto the disk at an extremely high density. The read/write head, however, must be in close proximity (less than a wavelength away) to the recording medium, similar to a "near field" optical setup. The medium consists of a layer of magnetic material on top of a plastic substrate. The bits are written perpendicular to the plane of the disk surface, which allows a higher packing density per unit area than the current longitudinal configuration in thin-film media. The domains are also arranged in an overlapping fashion, resulting in a series of crescent-shaped bits, which then doubles the number of bits stored in each track on the disk. Both factors enable a higher storage density compared with conventional media. Data retrieval is achieved using the Kerr effect, in which a beam of light is reflected off a written domain on the disk and is polarized in a direction dependent on the magnetization of the bit. Researchers in favor of this approach are foreseeing that this type of recording technology can extend the anitcipated limit on current storage using thin-film media (due to the superparamagnetic effect) to 200Gbits/in.^{2}.

Chapter 4 Previous perpendicular patterned media approaches

Miniaturization of magnetic storage media can be explored through the use of high resolution microfabrication techniques such as high voltage electron beam lithography, which allows us to routinely generate masks in resist materials with lateral dimensions of 50nm and below [53, 54, 55, 56]. For the fabrication of magnet arrays with in-plane magnetic shape anisotropy, we can use a lift-off process in which the magnetic material is vapor-deposited through a line mask. The width and length of the magnets are determined lithographically, and the thickness of the magnets is controlled during the magnet deposition process. However, for the fabrication of small magnets with shape anisotropy perpendicular to the substrate surface, the use of metal lift-off techniques is limited since the organic resist layer must be substantially thicker than the vapor-deposited magnetic layer.

The problem of obtaining high aspect-ratio perpendicularly anisotropic nanomagnets has been solved in the past by electroplating magnetic metals to create vertical magnetic pillars [57, 33, 58]. The smallest size and shape of the resulting nanomagnets are ultimately determined by the interaction of the electron beam with the resist layer by forward and backscattered electrons (proximity effects). For conventional electron beam exposure energies, forward scattering of electrons in the resist and proximity effects limit the aspect ratio and ultimate density of magnet arrays. To improve this anisotropy, we can either use a trilevel resist technique or high voltage electron beam lithography on a single-level resist microplating mask. Here two different approaches to fabricating arrays of small magnets using a single-level electron beam resist are described.

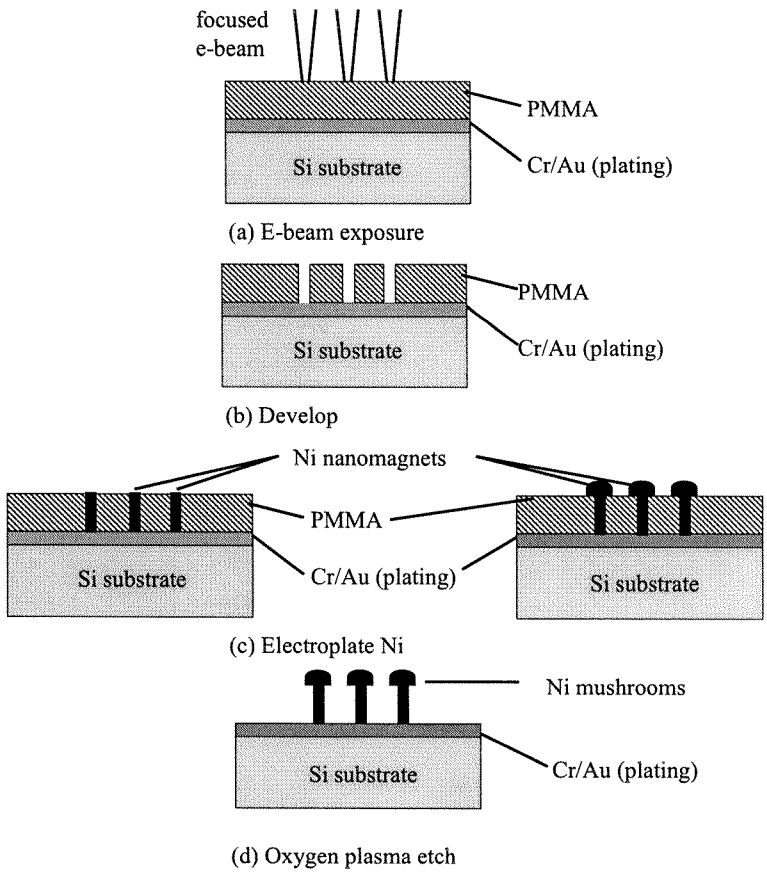

Figure 4.1: Schematic diagram of the fabrication procedure used to generate ultra-small magnets.

4.1 Ni columns in PMMA

In our initial work [59], we have focused on creating free-standing magnets of 20nm diameter and 100nm spacing (representing a particle density of 65Gbits/in.^{2}) using a combination of high resolution electron beam lithography and metal electroplating with optical end-point detection.

4.1.1 Fabrication

The procedure used for the electrodeposition of nickel (Ni) is shown in Figure 4.1. First, we prepare our semiconducting or insulating substrate by vapor-depositing a thin conducting gold layer in a pattern, which electrically connects a beam-writing pad with a probe contact pad. We then spin on a single high molecular weight

(950,000) PMMA resist layer. This resist is then exposed by using a Philips EM-430 scanning electron transmission microscope (STEM) with an acceleration voltage of 250kV. Following the lithographic exposure, the beam-written patterns are developed in a 3:7 cellusolve-methanol mixture. We then electrodeposit Ni, either from a nickel sulfamate or nickel sulfate electrolyte, into the holes formed in the PMMA resist. Electroplating is done under a probe station without agitation, which allows us to optically observe the deposition process. The cathode contact is made by using a photoresist-coated probe, whereas the anode consists of an annular nickel cup with an opening cut in the center. Depending on the electroplating time, we either obtain high aspect ratio nickel pillars or mushroom-like structures. Although the individual magnets are much smaller than the wavelength of light, a transition between these two geometries gives rise to an abrupt change in the reflectivity from the magnet array surface and can immediately be detected under the optical microscope.

Finally, when the electroplating process is completed, the PMMA can be removed by an oxygen plasma etch, which reveals the magnetic nanostructures. This procedure is not necessary or desirable unless the magnetic arrays are to be subsequently measured by electron microscopy, since the PMMA serves as an excellent matrix providing mechanical and chemical stability to the magnets. To exam the magnetic nanostructures, we use scanning electron microscopy (SEM) and relection electron microscopy (REM) [60, 61] in the Philips EM-430 STEM. We use these techniques to measure the size, the anisotropy, the surface quality, and the crystallinity of the nickel nanostructures. The magnetic quality of the structures can also be measured using a magnetic force microscopy [62].

4.1.2 Characterization of uniform magnet arrays

After electrodeposition, scanning electron microscopy allows us to image only the top of the magnets [Figure 4.2 (a)]. To reveal the complete magnetic structure, the PMMA can be removed with an oxygen plasma etch [Figure 4.3 (a)]. Alternatively, the magnets can be imaged with high voltage (100kV) scanning electron microscopy

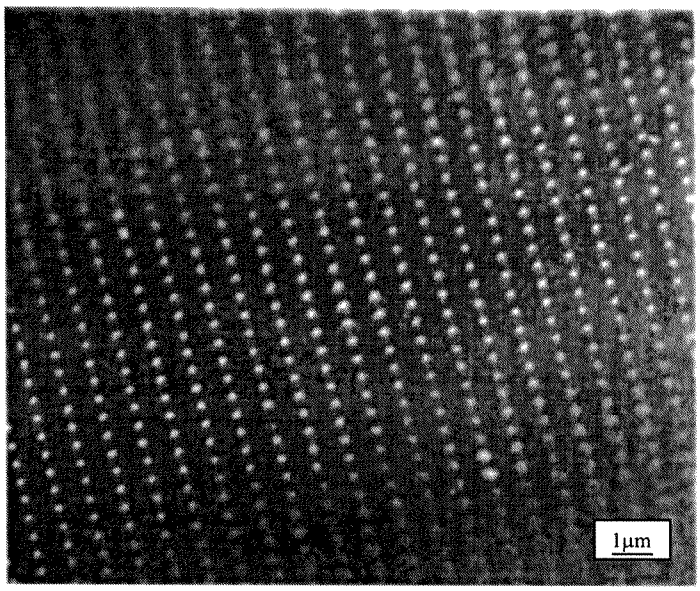

(a)

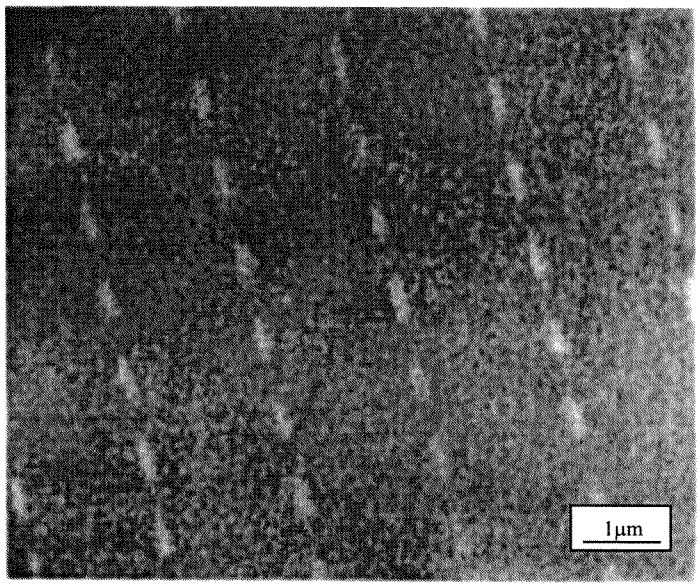

(b)

Figure 4.2: (a) SEM micrograph of a Ni magnet array before the removal of PMMA resist. (b) High-voltage backscattered electron micrograph showing the nickel posts underneath the PMMA layer.

using the backscattered electron detector [shown in Figure 4.2 (b)]. Since the electron beam resist serves as a mold into which the magnetic material is deposited, it is necesssary to determine the time at which the electrodeposited metal completely fills the holes in the resist to prevent isotropically plated metal, or mushrooms, from forming on top of the magnet [Figure 4.3(b)]. As in macroscopic plating processes, the electrodeposition rate is dependent on the current density, the nickel concentration in the electrolyte, the temperature, and the agitation of the solution [63]. We find that in lithographic samples, where extremely small areas are electrodeposited, it is very difficult to precisely predict the surface area to be plated, and therefore no reproducible value for the current density is obtained. Moreover, the deposition rate is also found to be dependent on the size of the feature that is to be plated.

4.1.3 In situ observation and end-point detection

As the deposition rate cannot be accurately determined a priori, it is necessary to develop an in situ end-point detection system that can be used to determine the optimum electroplating time. By measuring the height and the width of electroplated magnets and relating these to the exposure dose, we have found a systematic relationship between the deposition rate and the size of the nanostructure to be plated (Figure 4.4). We find that the electroplating rate is slightly faster in larger holes than in small structures, and therefore it is possible to use arrays of larger (150nm-diameter) magnets as sacrificial internal standards to stop the electrodeposition process when these test regions are filled. As the plated nanostructures change from pillars to mushrooms, we observe a significant change in contrast in the optical microscope probe station. Since a series of different sized magnet arrays are usually defined for optimization of the lithographic dose, this end-point detection is a convenient method for reproducibly obtaining highly anisotropic magnets.

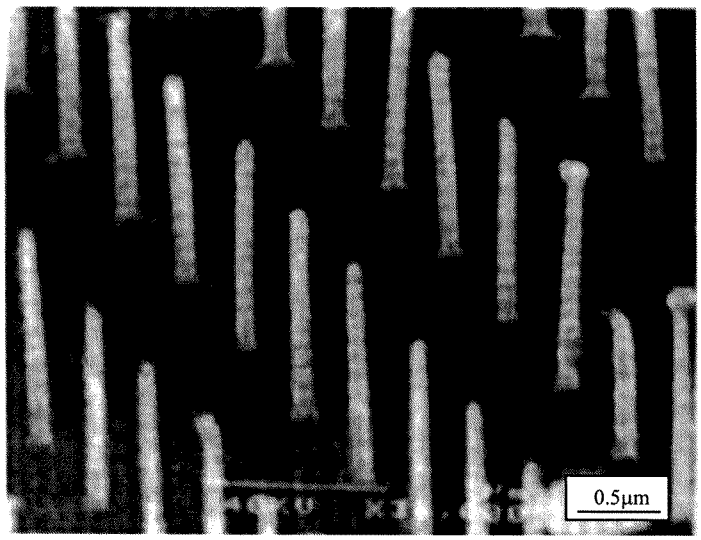

(a)

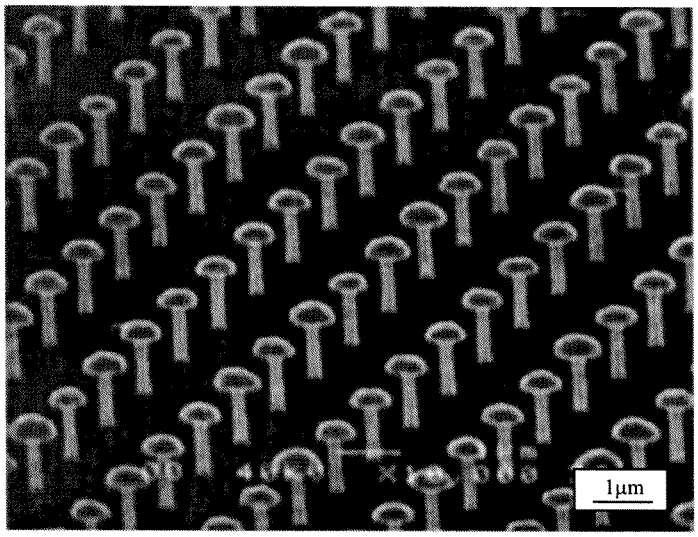

(b)

Figure 4.3: (a) SEM micrograph of a Ni column array after oxygen plasma etching to remove the PMMA. (b) SEM micrograph of an overplated micromagnet array showing the mushroom shape characteristics of isotropic metal deposition.

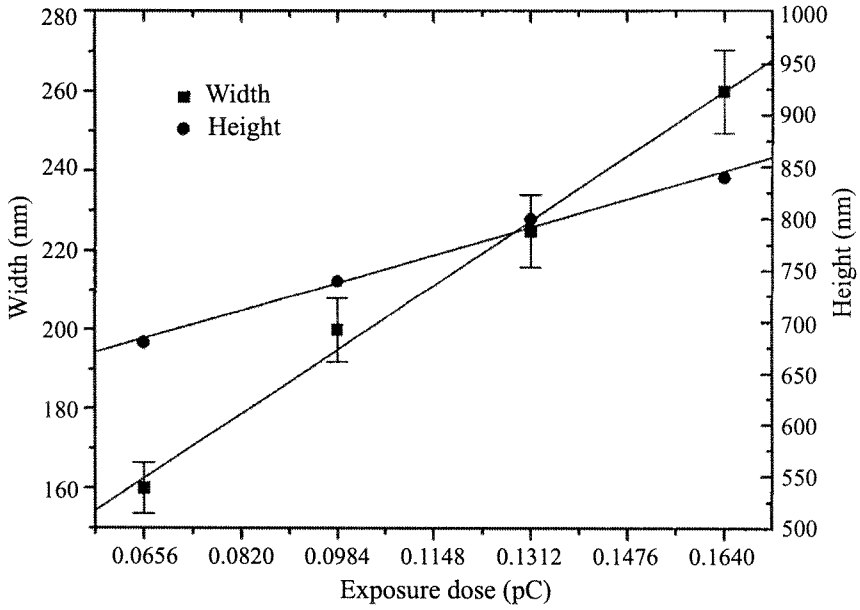

Figure 4.4: Measured dependence of the height and width of the electroplated nanomagnets on the electron-beam exposure dose (in μC).

4.1.4 Electroplated etch mask

Since nickel is an excellent etch mask, we have used the electroplated nickel posts to transfer anisotropic structures into the underlying semiconductor. The large thickness of the nickel masks makes electroplating a convenient method for defining very robust dry etch masks without the use of complex multilayer contrast enhancement schemes. We demonstrate this technique in Figure 4.5, where we show plated nickel pillars that were used to etch a silicon substrate to a depth of 1.5μm using a CCl_2F_2/NF_3 reactive ion etch. During the etching process, the thin vapor-deposited gold membrane onto which the mask was plated was removed almost immediately, leaving the substrate to be etched as deep as is desired. For the deposition of similar thicknesses of metal mask, significantly thinner resist layers can be used when electroplating than when using an evaporation/lift-off process. This can result in correspondingly higher pattern resolution and/or etch anisotropy.

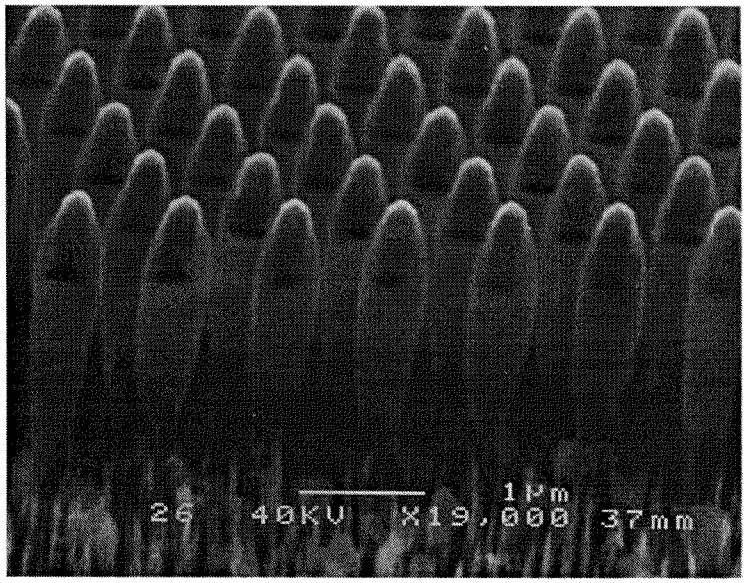

Figure 4.5: Etched silicon pillars defined by using a 1-μm-thick electroplated nickel etch mask.

4.1.5 Ultrasmall magnets, mushroom structures, and reflection microscopy

Arrays of uniform nanomagnets as small as 20nm in diameter have been produced and were examined through scanning electron microscopy and reflection electron microscopy. The current density during electroplating is very difficult to determine, and the most common failure mode of this process lies in the incorrect timing of the electrodeposition, which results in plating of mushroom-like structures. In Figure 4.6, we show a 30-nm-wide and 0.4-μm-tall lithographic column after such an electroplating and resist removal. Plated magnets were also examined by reflection electron microscopy, a technique that allows us to obtain a dark-field transmission electron micrograph from the sample surface and image the crystalline structure of the pillars. From the reflection electron micrograph of Figure 4.7 we observe a microcrystalline plating morphology after nickel sulfamate deposition of 100-nm-wide magnetic pillars. Other REM images and diffraction patterns confirm that the nickel crystallite size is approximately 5nm. In addition to fabricating metal structures, electroplating is also an excellent method for determining the shape of the electron

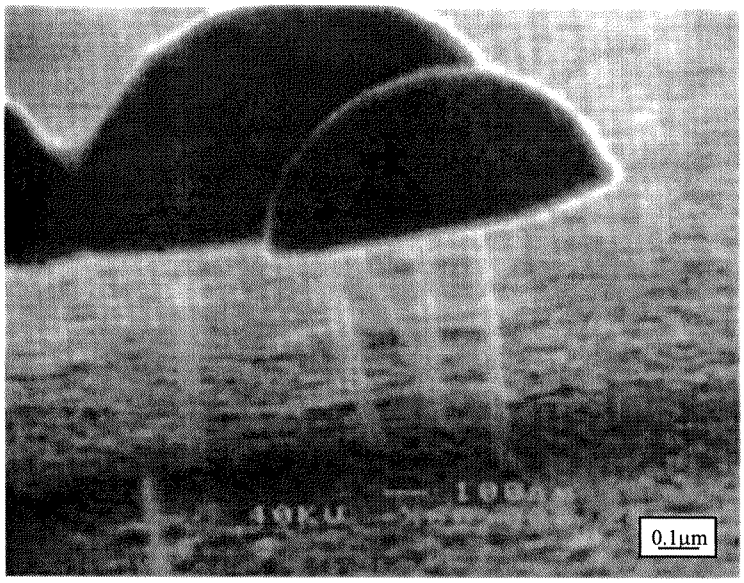

Figure 4.6: Overplated 30nm-wide magnetic columns showing the resolution of the electron-beam writing and electroplating process.

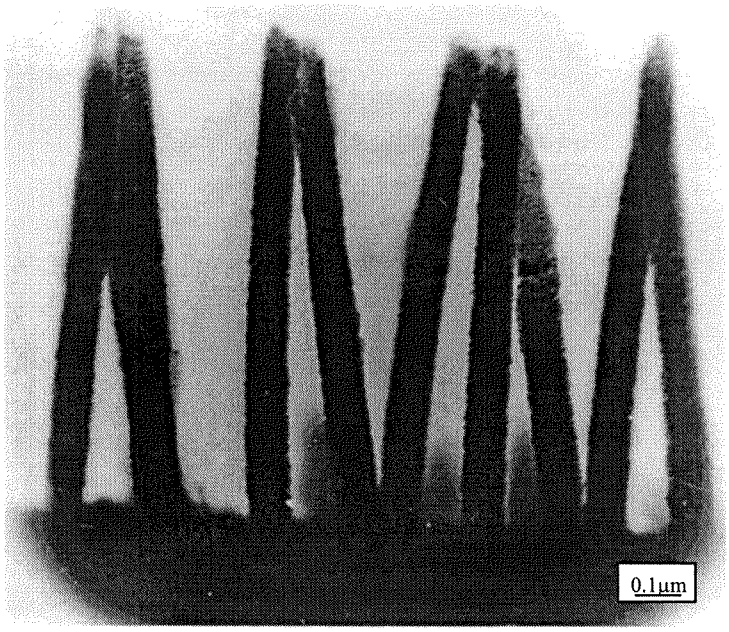

Figure 4.7: Reflection electron micrograph of 100-nm-wide and 1-μm-tall magnets.

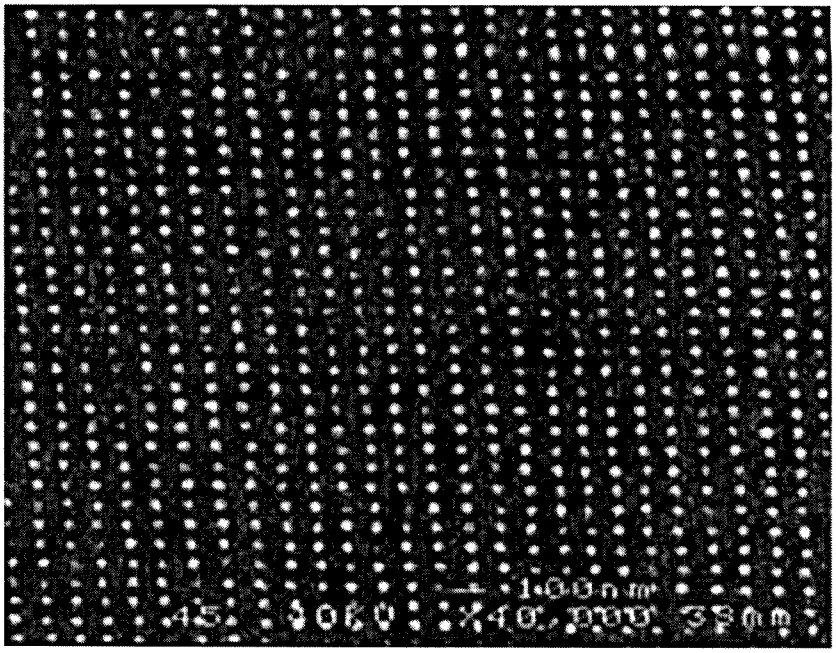

Figure 4.8: High density (65Gbits/in.^{2}) magnetic recording media. Nanomagnet arrays of 20nm Ni pillars with 100nm spacing were microfabricated.

beam interaction volume in the electron beam resist. When we compare the sidewall angle of magnets defined through electron beam lithography at 30 and at 250kV, we observe significantly lower anisotropy as a result of forward scattering of the incident electron beam during low-voltage exposure [64], which results in magnets with shapes resembling truncated cones. At higher electron beam energies, it is possible to define high aspect ratio magnets with vertical sidewalls.

4.1.6 Dense magnetic arrays for storage media

The inherently high contrast of high voltage electron beam lithography allows the fabrication of very dense arrays of small structures. Since the density of magnetic particles limits the memory storage capacity, it is desirable to explore the highest possible density of magnetic structures in regular arrays. We have used e-beam lithography to define arrays of 20nm magnets with 100nm pitch (Figure 4.8). This packing density translates into an equivalent of 65Gbits/in.^{2}. The density of the magnets can be further increased by optimizing the electron beam lithography parameters.

Although the densities achieved using this approach of embedding Ni magnets in PMMA is quite attractive for future magnetic storage, PMMA is not robust enough for the commercial chemical mechanical polishing process to planarize the surface of the disk. Because of the low "flying" height between the recording head and the medium, the latter needs to be ultraflat in order to avoid any accidental head crash due to protruding columns. Also, if the plating process is stopped before the columns are above the surface of the substrate (i.e., start to mushroom), some columns may be underplated and are too far away from the surface to be properly recorded by the read/write head, which may be hundreds of nanometers above them. The ideal situation will be to overplate the Ni columns and then polish them down to the desired height, which is determined by the thickness of the embedding material. There are several material systems that may be more suitable for use as the embedding material. Almost all of them require additional mask amplification following electron beam lithography. In these cases, PMMA only serves as an e-beam sensitive polymer and an initial ion etch mask, but not the final mold into which the magnetic material is being deposited. We will be describing structures utilizing silicon dioxide (SiO_2) as the embedding material, in the following section.

4.2 Ni columns in SiO_2

More realistic structures, made of embedded Ni columns in a durable SiO_2 substrate, have been investigated by several groups [33, 65]. The collaborative effort between O'Barr and co-workers at UCSD and our group have concentrated on embedding Ni columns in SiO_2 using a combination of high resolution e-beam lithography, dry etching, and electroplating. The fabrication procedures are summarized in Figure 4.9. The techniques involved are e-beam lithography to define the hole array patterns, the transfer of patterns into the embedding material (SiO_2) using C_2F_6 reactive ion etch (RIE), followed by electroplating of Ni from a Cr/Au seeding layer, and chemical mechanical polishing. A more detailed description of the procedures can be found in Reference [65].

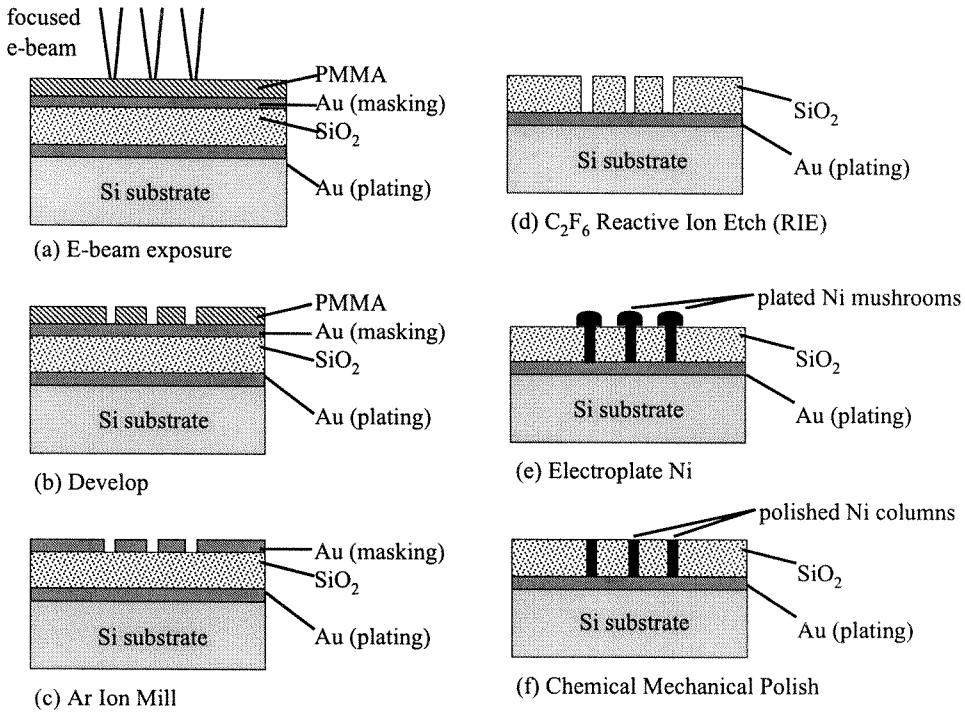

Figure 4.9: Schematic diagram of the fabrication procedure for Ni column arrays embedded in SiO_2.

Figure 4.10 (a) shows an SEM image of an electroplated 23×23 Ni column array of 400nm diameter (at the surface) and 2μm spacing [65]. Figure 4.10 (b) shows an illustration of a single column before (left) and after (right) polishing. The column has a nominal diameter of 150nm, with a 400nm diameter at the surface. This widening of the lateral dimension of the column is suspected to be caused by corrosion of the top Cr/Au masking layer during etching of SiO_2 using C_2F_6 reactive ion etching (RIE). Note that there is a ~10nm depression of the column from the surface of the SiO_2 after polishing. This depression will add slight variations to the surface profile of each Ni column, and will decrease the signal detected using a commercial read/write head in the scanning magnetoresistance microscopy characterization, which will be described in more detail in a later chapter.

Using this approach of embedding Ni columns in SiO_2, O'Barr et al. have demonstrated the feasibility of using conventional magnetoresistive (MR) sensors to detect the fields coming out of the individual magnetic columns [65]. They have successfully

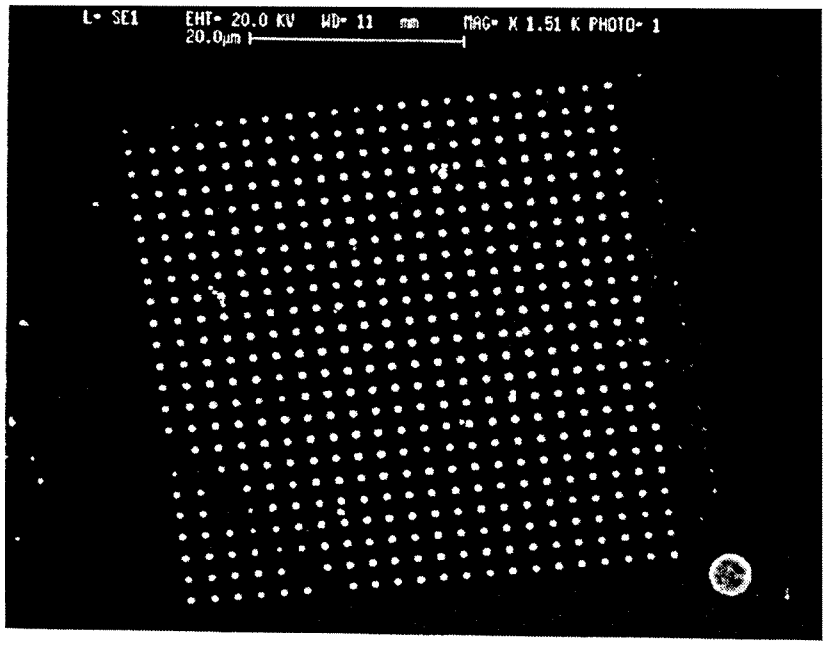

(a)

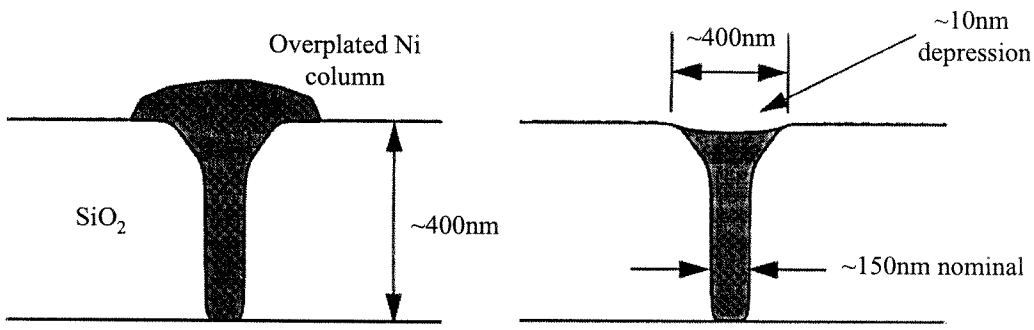

(b)

Figure 4.10: (a) SEM of an array of Ni columns embedded in SiO_2. (b) An illustration of a single column before (left) and after (right) polishing.

proven the compatibility of this type of patterned media samples with a commercial recording head, provided that an external applied magnetic field is present to aid the magnetization orientation of the columns during the readback process. In the absence of an external field, however, Yamamoto and co-workers [66] have found that the coercivity of the resulted columns was not high enough to achieve the magnetic stability required for reliable reading and writing of this form of media. With these results at hand, our goal is to design a material and substrate system that can support higher coercivity, hence more stable, magnetic columns in which binary data can be stored and retrieved nondestructively.

Chapter 5 Perpendicular patterned media in an Al_2O_3/GaAs substrate

In order to improve the coercivity of the individual magnetic columns without switching to a different magnetic material system such as cobalt (Co), we have re-examined the fabrication process, and have developed an alternative approach for creating high aspect ratio Ni magnets that are embedded in an Al_2O_3/GaAs substrate [67]. Instead of using e-beam resist (PMMA) or silicon dioxide (SiO_2), we employ Al_2O_3 and GaAs. In this approach, we take advantage of the shape anisotropy of the Ni columns to achieve the stability required for the media to be useful for information storage. It has been found that the etch rate selectivity of Al_2O_3 over GaAs is in excess of 30:1 [68]. Thus, by combining the robust Al_2O_3 mask, high resolution electron beam lithography, and the directional chemically assisted ion beam etching (CAIBE), it is now possible to achieve small diameter and high aspect ratio holes in the GaAs substrate, which are then filled with Ni by electrodeposition.

5.1 The importance of high coercivity in media

For permanent magnetic storage applications, larger values of coercivity of the recording material are preferable in order to retain the written information for a long period of time. On the other hand, the coercivity should not be so large that it becomes difficult for the recording head to produce enough field to write information in the medium. The issue of having too large of a coercivity in the storage medium is more critical in the magnetic recording industry at this point than in the research and development of alternative storage media. This is because the grain size in current thin-film media is already at a dimension small enough to start displaying the superparamagnetic effect. This possible detrimental outcome has prompted the industry

to investigate exceptionally high coercivity materials suitable for storage.

In our perpendicular patterned media research, however, the dimension of the magnetic columns is still relatively large compared to the grain size in current thin-film media. Thus, even though the magnetic structures under investigation are single-domain (perhaps not under the definition in which only particles that rotate coherently during the entire reversal process are truly single-domain), we expect them to switch incoherently and have a lower coercivity than in the case of coherent reversal. In other words, higher coercivity is a desirable property in our perpendicular patterned media work, and the point at which the head field becomes insufficient for writing the columns is still distant. The results by Yamamoto et al. have reminded us of the importance of coercivity in our patterned media design. We realize that it is crucial that each magnetic column in our sample be strong enough to resist the demagnetizing fields from its surroundings. Opposing magnetic fields in recording can originate from the neighboring columns as well as the nonuniform magnetization in multi-domains found in the write poles of the recording head.

The magnetic hardness, or coercivity, of most fine particles is a direct result of the forces due to shape and/or magnetocrystalline anisotropy. In order to examine the effect of either of these contributions alone, one can try to make spherical particles to eliminate shape anisotropy, or elongated particles using a material having low or zero magnetocrystalline anisotopry [5]. When shape anisotropy dominates, the coercivity, H_{ci}, decreases as the packing fraction (defined as the volume fraction of magnetic particles in the array), p, according to the relation [5]:

$$H_{ci}(p) = H_{ci}(0)(1 - p), \tag{5.1}$$

where $H_{ci}(0)$ is the coercivity of an isolated particle ($p = 0$). Equation 5.1 is not regarded as theoretically sound and does not apply to all materials, but it gives a general trend for the relation between the coercivity and the packing density of an array of magnetic particles dominated by shape anisotropy. For the spherical particles in which magnetocrystalline anisotropy prevails, the coercivity is expected

to be independent of the packing density, p [5]. The reasoning behind this is that magnetocrystalline anisotropy is due to spin-orbit coupling which are forces "internal" to the particle. Whereas for shape anisotropy, the forces originate from magnetostatic fields, which are "external" properties.

5.2 The importance of high aspect ratio in fabricating Ni columns

Despite its small magnetocrystalline anisotropy, we choose to use Ni for the magnetic material in our samples due to the less stringent control parameters in the electroplating process compared to cobalt (Co). Co has a much higher magnetocrystalline anisotropy than Ni, which means that high aspect ratio structures are not necessary to get the desired stability in the magnets. In order to electroplate Co with the correct magnetization orientation, however, an applied magnetic field during plating as well as careful control of the pH of the plating solution are both necessary requirements. For research demonstration purposes, a smaller parameter space for processing optimization is preferable, and we also believe that Ni will provide us with the necessary coercivity in our columns for reliable recording and reading back of information.

With Ni as the candidate for the magnetic material for the embedded columns, we need to capitalize on the contribution of the shape anisotropy constant in the coercivity of the columns. From Equation 2.14, $K_s = 0.5(N_a - N_c)M^2$, it can be seen that the "strength" of the shape anisotropy of a material strongly depends on the axial ratio, c/a, of the specimen, which contributes to the term $N_a - N_c$. The coercivity of a column dominated by shape anisotropy is given by $H_{ci} = (N_a - N_c)M_s = 2K_s/M_s$. A table of calculated coercivities of single-domain particles (considering only shape anisotropy) as well as a plot of H_c versus aspect ratio (c/a) in the three common ferromagnetic material, Ni, Co, and Fe are shown in Figures 5.1 (a) and (b), respectively. It can be seen from the plot in Figure 5.1 (b) that the effect of aspect ratio on the coercivity of a particle is more dramatic for aspect ratios of 4:1 and below, after

Calculated coercivities of single-domain particles
(considering only shape anisotropy)

		Ni	Co	Fe
c/a	***Na -Nc***	***Hci* (Oe)**	***Hci* (Oe)**	***Hci* (Oe)**
1	0	0	0	0
1.1	0.472	228	671	810
1.5	1.892	916	2690	3240
2	3.012	1458	4283	5163
3	4.234	2050	6021	7257
4	4.861	2353	6912	8332
5	5.231	2532	7438	8950
6	5.469	2647	7777	9374
7	5.631	2726	8007	9652
8	5.748	2783	8174	9852
9	5.835	2825	8297	10001
10	5.901	2857	8391	10100
15	6.081	2944	8647	10423
20	6.156	2980	8754	10500
∞	6.283	3042	8934	10800

Saturation moment, M_s, Ni: 484 emu/cm^3
Co: 1422 emu/cm^3
Fe: 1714 emu/cm^3

(a)

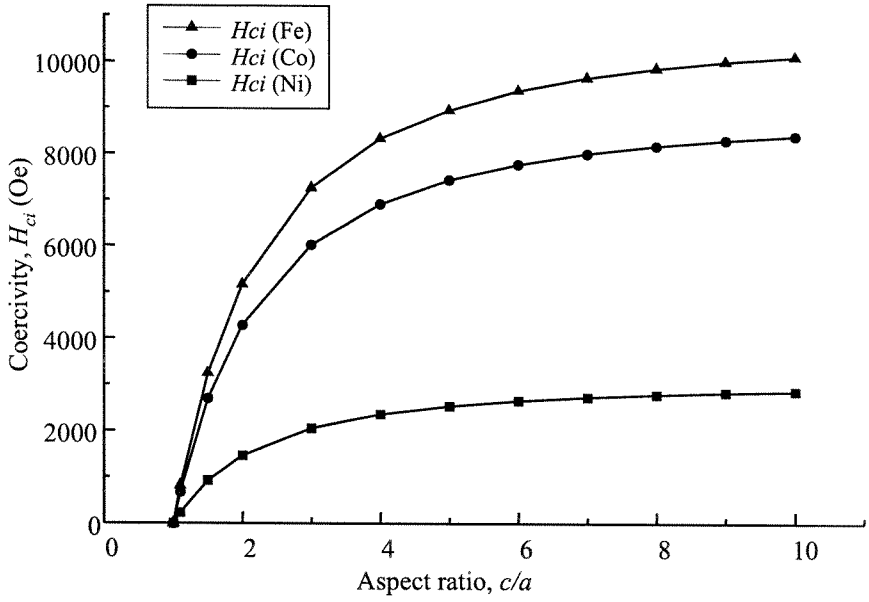

(b)

Figure 5.1: (a) Table listing the calculated coercivities of single-domain particles of Ni, Co, and Fe, of various aspect ratios. (b) A plot of coercivity, H_{ci} versus aspect ratio, c/a, of Ni, Co, and Fe using values from table in (a).

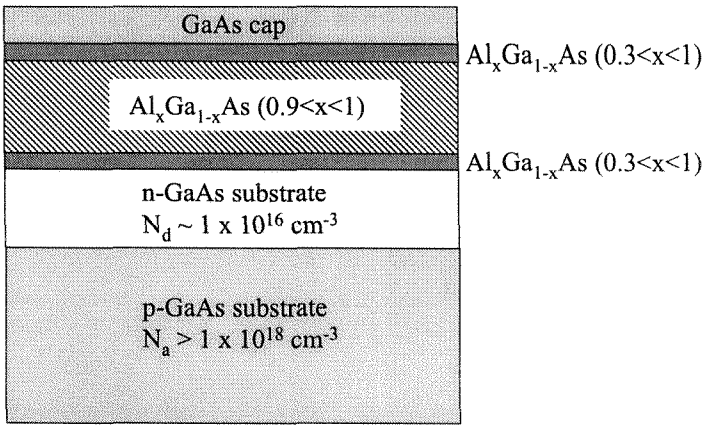

Figure 5.2: Schematic diagram showing the composition of the AlGaAs/GaAs substrate design.

which the coercivities continue to increase with aspect ratio but at a slower rate. For Ni in particular, the coercivity increases from 1458Oe for a 2:1 column to 2627Oe for a 6:1 column, the latter being the geometry of preference for the Ni columns in our perpendicular patterned media design.

5.3 Substrate design

With the requirement of having high aspect ratio Ni columns embedded in the substrate, we first need to design the substrate and the subsequent masking layers to allow pattern transfer to the desired depth into the substrate. The substrate is custom grown by molecular beam epitaxy (MBE) or metal-organic chemical vapor deposition (MOCVD), and the composition of the different layers is illustrated in Figure 5.2. The substrate is a p-type GaAs, using Zn as a dopant with carrier concentration of $>1\times10^{18}$cm^{-3}. The resistivity of the p-substrate is $1\text{–}8\times10^{-2}\Omega$-cm. Its orientation is (100)2°(110). The subsequent layer is an n-type GaAs, using Si as a dopant with carrier concentration of 1×10^{16}cm^{-3}. Above the p-n junction is an $Al_xGa_{1-x}As$ (90–100% Al) layer. The thickness of this AlGaAs layer increases as the aspect ratio specification for the resulting structure becomes higher. This AlGaAs layer is sandwiched between two optional thin graded regions of $Al_xGa_{1-x}As$ (30–100% Al) to promote its adhesion to the GaAs substrate. The top-most layer is a thin capping

GaAs to protect the underlying AlGaAs from room temperature oxidation to form $(AlGa)_2O_3$. All the AlGaAs and GaAs layers grown above the p-n junction are undoped. The composition and thickness of the masking layers above the AlGaAs/GaAs substrate are also dependent on the aspect ratio of the desired structures. The masking materials typically consist of SiO_2 and/or Cr/Au and PMMA (which serves as an e-beam resist as well as an ion etch mask). More details of the masking layers will be described in a later section of this chapter.

5.3.1 Function of a p-n junction in the GaAs substrate

Generally, it is undesirable for electroplating to proceed conformally with the etched semiconductor surface, since the top of the etched holes can be closed up before the bottom of the holes are completely filled. To avoid this problem, plating is often conducted on a substrate coated with a seeding layer, e.g., Au or Ti. To achieve high aspect ratio structures, an insulating material, such as SiO_2, is deposited on the seeding layer. This insulating layer is then perforated by dry etching or other techniques to define the desired patterns to be electroplated. However, we found that our dry etching capabilities allow us to define higher aspect ratio structures in semiconductors than in insulating materials. The high aspect ratio feature of the electroplated structures are desirable since this will enable us to take advantage of the shape anisotropy of the Ni columns we fabricate to achieve higher coercivity magnets. As a result, we have developed a new method to include a p-n junction in the GaAs substrate to facilitate proper filling of magnetic material into the etched holes in the semiconductor.

The introduction of a doped p-n junction in the semiconductor, which is reverse-biased during the plating process, allows us to plate metals into the etched holes in the substrate from the bottom of the hole upwards, thereby defining dense plated material. In this method, a p-n junction is either grown or defined through implantation or diffusion, to form a surface layer which can become insulating during the electroplating process. After this procedure, lithography and ion etching are used

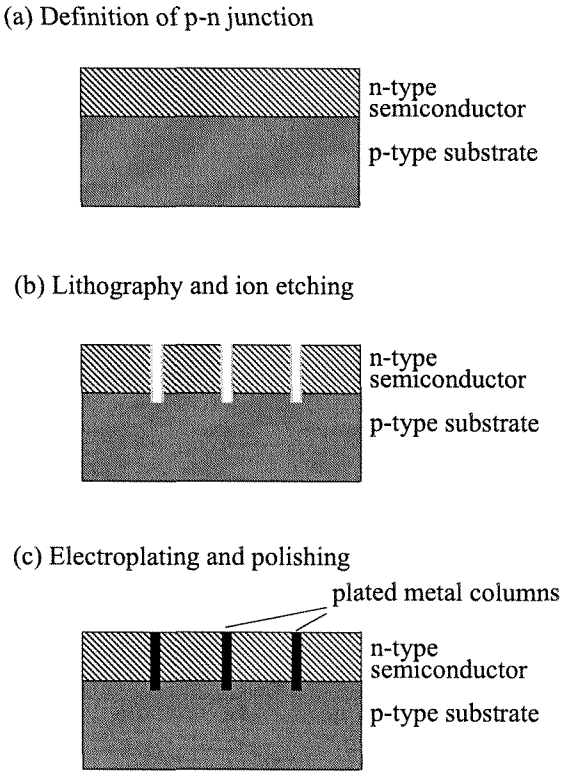

Figure 5.3: Schematic diagram showing the procedure for electroplating metal columns directly into an etched hole in a semiconductor substrate incorporating a p-n junction design.

to define holes through the p-n junction. When this layer is designed properly, it becomes depleted during the application of the electroplating voltage, and this allows current to flow only through the fabricated holes. This will force the electroplating to be limited only to the areas in which the p-n junction is perforated, and will avoid plating onto the sidewalls of the holes. Figure 5.3 shows the proposed procedure for the electroplating through fabricated holes in a p-n junction.

5.4 Fabrication procedures

A schematic flow diagram of the fabrication procedures in defining the Ni column arrays embedded in an Al_2O_3/GaAs substrate is shown in Figure 5.4 [67]. A 200nm layer of AlAs and a 50nm GaAs cap layer are grown by Molecular beam epitaxy (MBE) on top of GaAs substrate (consisting of a p-n junction described in the previous section). A 200nm layer of SiO_2 is then sputter deposited, and 10nm of Cr and 40nm of Au are subsequently evaporated onto the sample [Figure 5.4 (a)]. The Cr/Au evaporation should be carried out immediately after the SiO_2 sputter deposition to ensure good adhesion between the layers. Poor adhesion of the Cr/Au layer will result in delamination after any temperature cycling in the subsequent processing steps, such as the baking of PMMA prior to e-beam exposure. Dot array patterns are defined on the PMMA (baked at 150°C for 1-1/2h) coated sample by vector-scanned electron beam lithography. The electron beam lithography system used in the fabrication procedure is a commercial scanning electron microscope (SEM), Hitachi S–4500 II, that has been converted into an e-beam writer by a former member of our group [69]. The user implements the desired patterns in an AutoCAD file, which is then converted into voltage signals that are sent to the x/y scanning coils in the microscope to deflect the focused electron beam. Thus, the electron beam is scanned over the sample surface, exposing the PMMA layer to generate the designed structures in the AutoCAD file.

Following e-beam lithography, the patterns are developed in a 3:7 cellulose-methanol mixture [Figure 5.4 (b)], for an amount of time which is dependent on the exposure

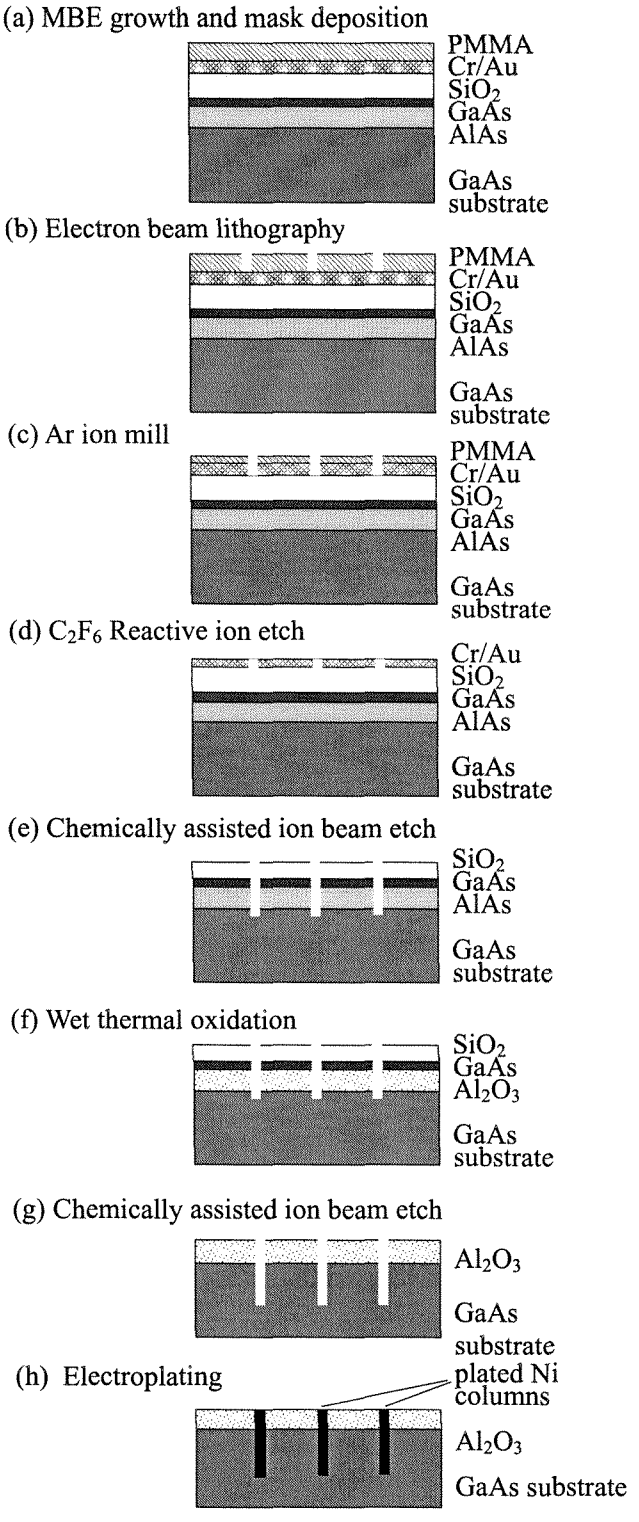

Figure 5.4: Schematic diagram of the fabrication procedures for high aspect ratio Ni columns embedded in an Al_2O_3/GaAs substrate.

dose and the PMMA thickness. The patterns are transferred into Cr/Au by Ar^+ ion milling [Figure 5.4 (c)] with a milling rate of ~70Å/min for Cr and ~400Å/min for Au, and then into SiO_2 by reactive ion etching (RIE) [Figure 5.4 (d)] with an etching rate of ~100Å/min using 20sccm of C_2F_6 at 60mTorr. The SiO_2 layer acts as an etch mask for further pattern transfer into AlAs by Cl_2 assisted ion beam etching [Figure 5.4 (e)]. In our chemically assisted ion beam etching (CAIBE) system, a Kauffman Ar^+ ion source is used in conjunction with a gas introduction nozzle to accelerate high energy ions toward the substrate covered with an etch mask. This allows us to achieve a high etching rate and selectivity of the semiconductor substrate, as well as the directionality necessary for defining high aspect ratio structures. Without the addition of a corrosive gas such as Cl_2, the system functions as a physical etching tool using only Ar^+ for ion bombardment. The etching rate of AlAs/GaAs in our CAIBE system is ~800 and 50nm/min with and without the addition of Cl_2, i.e., chemical vs. physical etching, respectively.

Immediately following CAIBE, the AlAs layer is converted into Al_2O_3 by wet thermal oxidation in a 1-in.-diameter tube furnace at 380°C for 15min [Figure 5.4 (f)][70]. Water vapor is supplied to the tube by bubbling nitrogen gas at 0.5L/min through deionized water heated at 85°C. This robust layer of Al_2O_3 is the final mask for pattern amplification in the perpendicular direction into the GaAs substrate by using further CAIBE [Figure 5.4 (g)]. Figure 5.5 shows an SEM image of an array of holes (left) defined by electron beam lithography, produced by the procedures just described. On the right side of Figure 5.5, we present a 10× enlarged view of a single hole of approximately 60nm in diameter.

Electroplating is then used to deposit Ni into the holes that have been etched into the GaAs substrate [Figure 5.4 (h)]. A schematic diagram of the plating apparatus is shown in Figure 5.6. This setup is almost identical to the one in [65], where the probe contacts the sample outside of the plating bath and does not disturb the electrodeposition of the Ni columns. In our case, a small Ni piece is used as the anode and the conductive GaAs substrate is used as the cathode. The Ni anode is etched in HCl immediately before each plating session so as to minimize any contaminants to

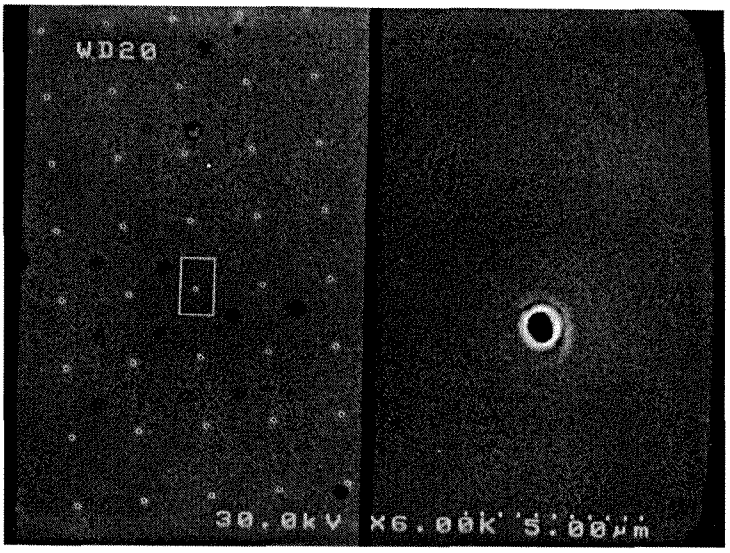

Figure 5.5: SEM image of an array of etched holes (left) before filling by electroplating with Ni, and a 10× enlargement of a single hole (right) of approximately 60nm in diameter.

be deposited into the hole arrays. A commercially available nickel sulfamate solution from Technic Inc. (with proprietary additives included in the solution to promote the magnetic properties of the plated material) is used as the plating medium. A pulse current with a duty cycle of 80% (2s on and 0.5s off) is applied to the p layer of the conductive GaAs substrate. We find that if the duty cycle is close to 50%, the accumulation and dissolution rate of Ni in the etched holes become comparable to each other and the plating rate is jeopardized as a result. A plating current of 1μA is typically used for an e-beam exposed region with 300 sets of 100×100 dot arrays of 170nm hole diameter. The exact current density is difficult to determine since the area of the conductive p-GaAs substrate that is being contacted varies with the etch depth of the defined holes. There may also be scratches on the sample where the conductive GaAs layer is exposed to the plating solution. As a rough guideline, we adjust the plating current such that we do not see mushrooms appearing from the top of the etched holes, which would indicate a very rapid plating rate. The plating is conducted under an optical microscope, and end-point detection is possible through the change in optical contrast of the plated Ni columns. Precise end-point detection is not critical in our case as any overplated Ni column can be polished to the desired

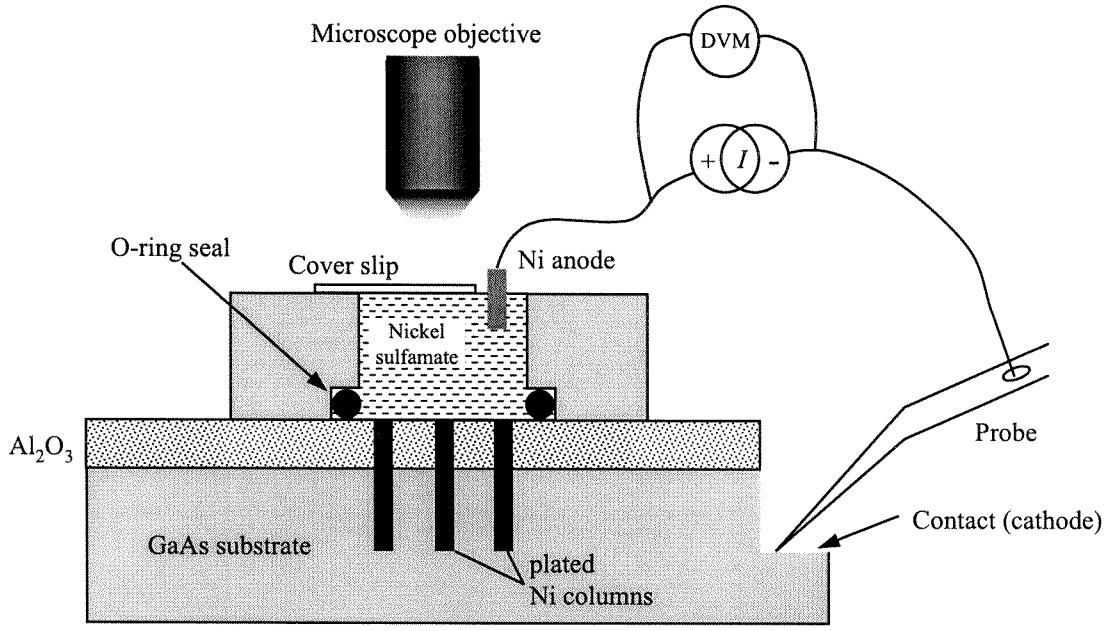

Figure 5.6: Schematic diagram showing the apparatus used for electroplating Ni into the holes defined in the Al_2O_3/GaAs substrate.

height, which is determined by the thickness of the Al_2O_3 layer, using a mechanical polish.

Using this new approach, we have fabricated arrays of 80×80 Ni columns of 6:1 aspect ratio that are embedded in a hard Al_2O_3/GaAs substrate. Figure 5.7 shows an SEM image of an electroplated Ni dot array of 100nm diameter and 2.5μm spacing (a) before and (b) after polishing. The plating seems to be very uniform over a large area and the mechanical polishing procedure results in a clean and smooth Al_2O_3 surface. Atomic force microscopy shows that the columns protrude 20–50nm out of the surface, and the area around the columns has a surface roughness of 5nm. We have also fabricated dot arrays of the same diameter (100nm) but smaller spacing (215nm) using the same technique. However, we chose a 2–2.5μm column spacing in our structures to match the sizes of the magneto-resistive sensors used in the magnetic characterization. Figures 5.8 (a) and (b) show cross-sectional views of an etched line of 225nm width and 1.65μm depth before and after electroplating Ni respectively. It is believed that the etched holes have similar cross section profiles as the etched lines, with the exception of slightly smaller diameters and depths, which, however,

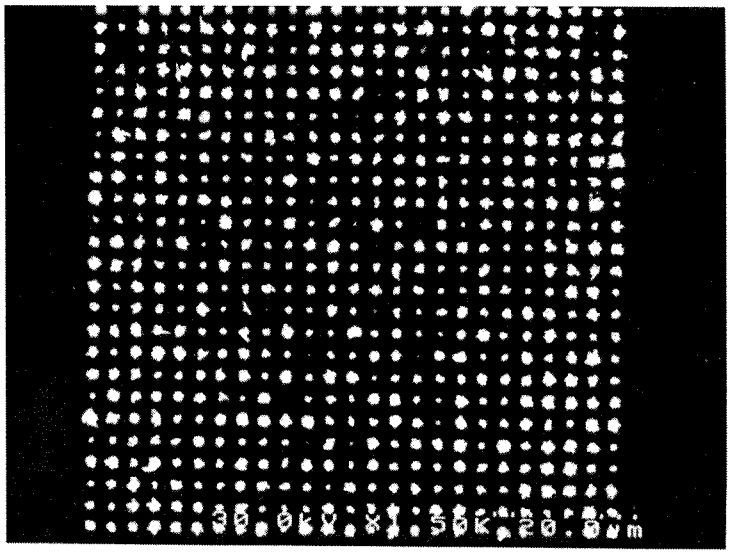

(a)

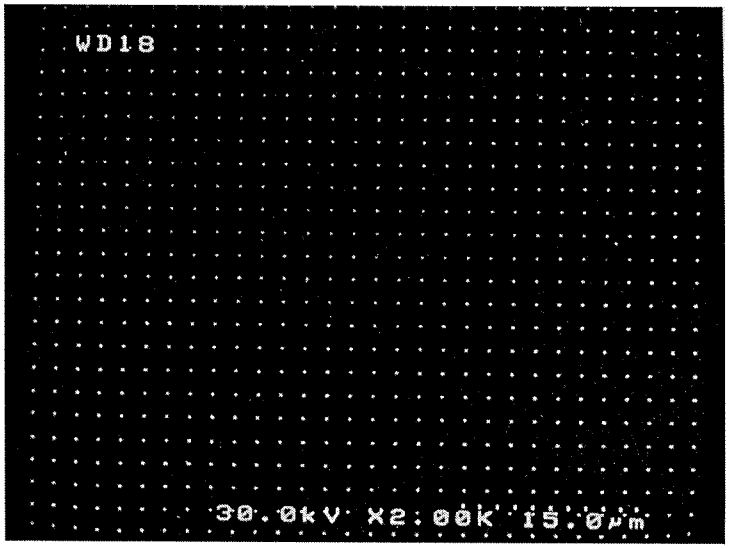

(b)

Figure 5.7: SEM images of an electroplated Ni dot array of 100nm diameter and 2.5μm spacing embedded in an Al_2O_3/GaAs substrate (a) before and (b) after polishing.

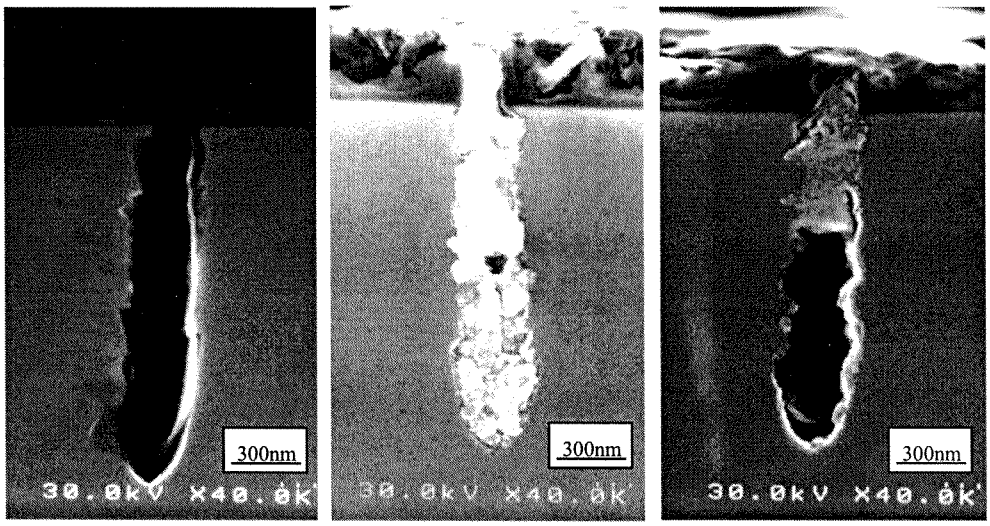

(a) (b) (c)

Figure 5.8: Series of cross-sectional SEM images of an etched line in an Al_2O_3/GaAs substrate (a) before electroplating, (b) electroplated with Ni utilizing an embedded p-n junction, and (c) closed up with Ni before the bottom of the etched line is completely filled.

correspond to similar aspect ratios. Figure 5.8 (c) shows a cross-sectional SEM image of an etched hole in the GaAs substrate closed up with Ni before the bottom of the hole is completely filled. This is the result of electroplating directly into the etched semiconductor without an embedded p-n junction.

We find that a good adhesion of the Al_2O_3 layer to the semiconductor substrate is very important in the electrodeposition procedure. If the Al_2O_3 delaminates from the substrate, especially near the etched holes, the plating electrolyte can then propagate into the grooves between the oxide and the semiconductor, and the nucleation of nickel may be promoted inside the grooves. Ni disks may be formed underneath the oxide layer in addition to the formation of the regular Ni cylinders in the etched holes. Figure 5.9 shows SEM micrographs of the identical lower left corner of a 50×50 array of embedded Ni columns in an Al_2O_3/GaAs substrate after plating, before (a) and after (b) polishing to remove the overplated mushrooms. The disks are not visible in Figure 5.9 (a) as their diameters are similar to those of the mushrooms on the surface. After polishing, however, it is clear in the SEM image in Figure 5.9 (b) that disks have been formed underneath the surface in a large portion (except around the

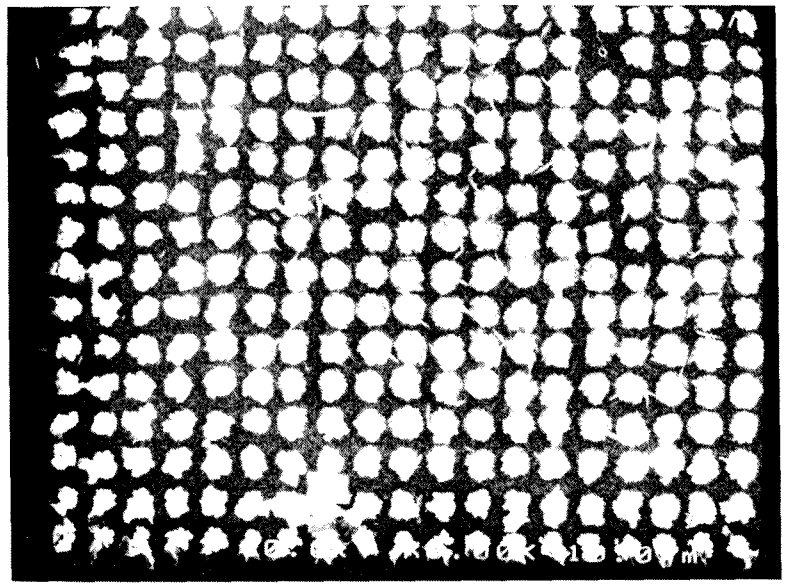

(a)

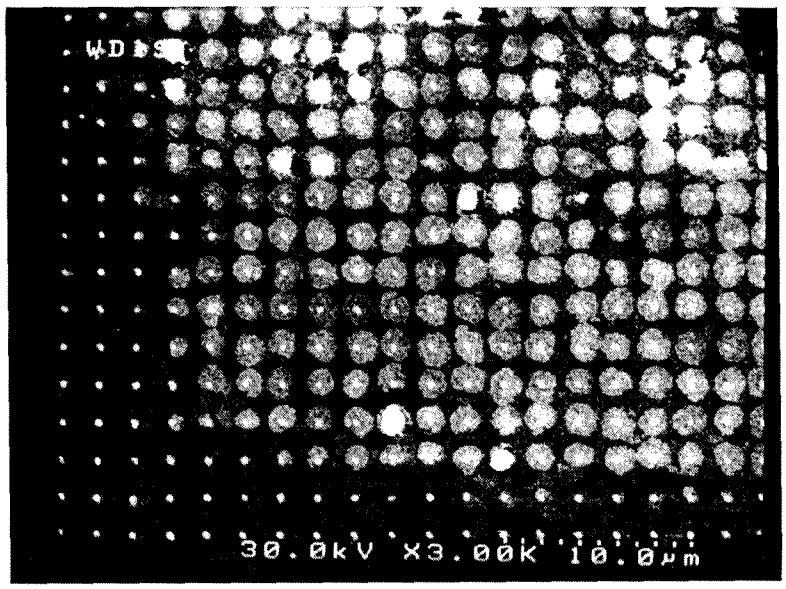

(b)

Figure 5.9: SEM images of the same array of embedded Ni columns in an Al_2O_3/GaAs substrate after electroplating, before (a) and after (b) polishing to remove the over-plated mushrooms. Ni disk formation between the Al_2O_3 layer and GaAs substrate is evident in the image in (b).

borders) of the array. This situation is undesirable, since even though the Ni columns are still cylindrical in shape, the magnetization throughout the column may not be uniform due to the influence of the randomly oriented fields radiating from the disks. This potentially catastrophic side effect of the disk formation has prompted us to use $Al_{0.9}Ga_{0.1}As$ instead of AlAs for the masking layer. It has been found that the oxide formed from AlGaAs alloys tends to be more mechanically stable against delamination along the oxide/semiconductor interfaces after any post-oxidation thermal cycling or processing steps which require temperatures of >100°C [71]. In addition to the AlGaAs composition change, a 15nm graded (30% to 90%) layer of AlGaAs has also been added to both sides of the $Al_{0.9}Ga_{0.1}As$ layer in the new structure to promote adhesion during the post-etching oxidation process. Furthermore, we have simplified our fabrication procedure from the previous one shown in Figure 5.4, which still allows us to achieve the required high aspect ratio columns embedded in the substrate.

The modified fabrication procedure is shown schematically in Figure 5.10 [72]. A 250nm layer of $Al_{0.9}Ga_{0.1}As$ and a 100nm GaAs cap layer are grown by metal-organic chemical vapor deposition (MOCVD) on top of a conductive GaAs substrate (consisting of a p-n junction as described in the previous section). Instead of using Cr/Au and SiO_2 as etch masks [67], we now employ only a thicker layer (550nm) of high molecular weight (950,000) PMMA, which serves as both an e-beam sensitive resist and an ion etch mask [Figure 5.10 (a)]. Similar to the previous procedures, dot array patterns are defined on the PMMA coated sample by vector-scanned e-beam lithography, followed by development in a PMMA developer [Figure 5.10 (b)]. The patterns are then selectively transferred into both the GaAs cap and the underlying $Al_{0.9}Ga_{0.1}As$ layer by Cl_2 CAIBE [Figure 5.10 (c)].

Following CAIBE, the sample is rinsed in acetone and dichloromethane to remove the remaining PMMA. To ensure complete removal of the PMMA after etching, cross-linking of PMMA is avoided by using a lower ion beam current (20mA instead of 30mA) and keeping the sample stage cooled during CAIBE. The $Al_{0.9}Ga_{0.1}As$ layer is subsequently converted into $(Al_{0.9}Ga_{0.1})_2O_3$ by wet thermal oxidation at 380°C for 1-1/2h [Figure 5.10(d)] [70]. The water vapor and nitrogen supplies are identical to

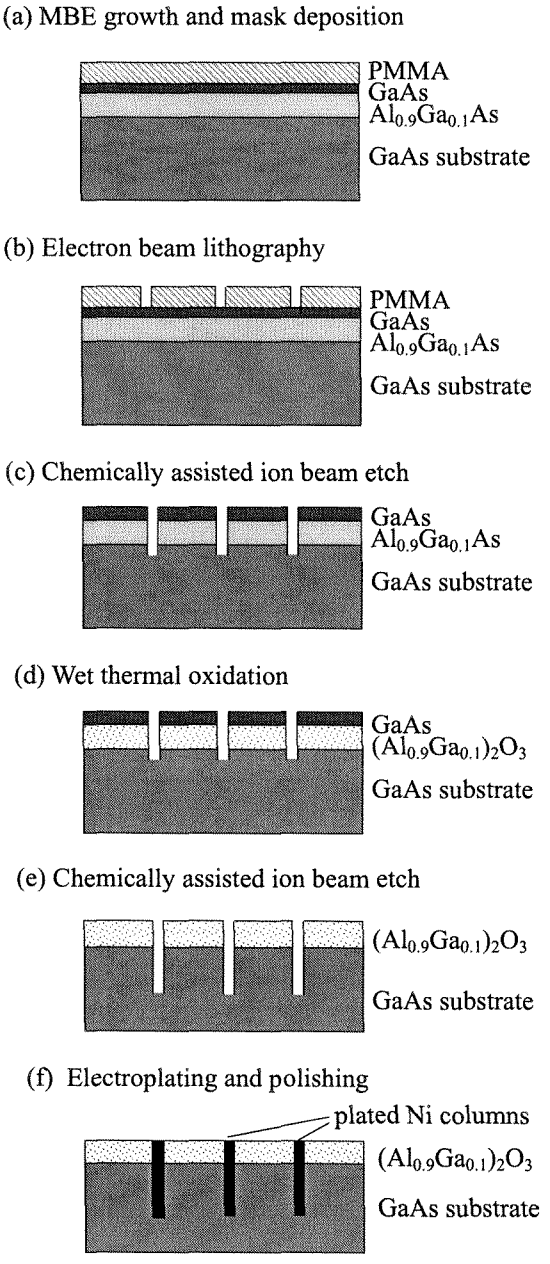

Figure 5.10: Schematic diagram of the fabrication procedures for high aspect ratio Ni columns embedded in an $(Al_{0.9}Ga_{0.1})_2O_3$/GaAs substrate.

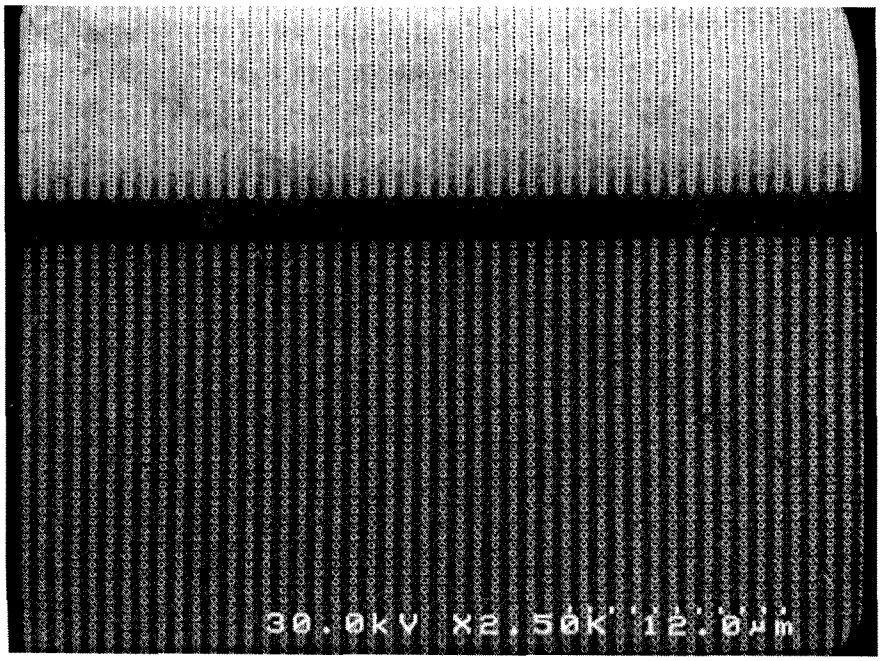

Figure 5.11: SEM image of two arrays of holes of 150nm in diameter defined in an $(Al_{0.9}Ga_{0.1})_2O_3$/GaAs substrate. The holes are 0.25 and 0.5μm apart (top and bottom array, respectively) in the down-track direction, and 1μm apart in the cross-track direction.

the conditions described in the previous procedures. To enable a more reproducible oxidation process, each sample is etched immediately before oxidation, and nitrogen gas and water vapor are allowed into the furnace 1/2 hour prior to each run. The resulting robust layer of $(Al_{0.9}Ga_{0.1})_2O_3$ is again the final mask for pattern transfer to the desired depth into the GaAs substrate by using further CAIBE [Figure 5.10 (e)]. Figure 5.11 shows an SEM image of two arrays of holes of 150nm diameter defined in the $(Al_{0.9}Ga_{0.1})_2O_3$/GaAs substrate. The holes are 0.25 and 0.5μm apart (top and bottom array, respectively) in the down-track direction, and 1μm apart in the cross-track direction.

Once the hole array patterns are transferred to the desired depth into the GaAs substrate after additional CAIBE, electroplating is then used to deposit Ni into the holes [Figure 5.10 (f)]. Any overplated Ni columns can be removed down to the $(Al_{0.9}Ga_{0.1})_2O_3$ surface, using a chemical mechanical polish (CMP). For polishing, we use a CMP pad SIP2000A in combination with a polishing slurry that consists of a

liquid dispersion of 20–30nm colloidal silica spheres at a concentration of 28% and a pH of 11.3 [73].

5.5 Two-dimensional masking

Using this modified procedure, we have fabricated arrays of Ni columns that are embedded in a robust $(Al_{0.9}Ga_{0.1})_2O_3$/GaAs substrate. Figures 5.12 (a) and (b) show SEM images of arrays of etched holes, 120nm in diameter, in the form of $0.25\mu m \times 1\mu m$ (a) and $0.5\mu m \times 1\mu m$ (b) tracks, in the GaAs cap/$(Al_{0.9}Ga_{0.1})_2O_3$/ GaAs substrate after oxidation and additional CAIBE (left). The right portion of each figure represents a 10× enlargement of the etched holes on the left. To monitor the etch rate and other processing conditions of the individual samples, we have also investigated in larger diameter e-beam exposed markers that are defined adjacent to the smaller diameter hole array patterns of interest. Their large diameter allows us to image any roughness on the sidewalls and bottom of the etched hole without having to cleave (and destroy) the sample. We can also estimate from the etch depth of the markers whether the p-GaAs substrate in the smaller sized hole patterns has been penetrated. This aids us in determining the stopping point of the CAIBE procedure. Figure 5.13 (a) shows a 38° tilted view of a 5-μm diameter hole after CAIBE and oxidation. The right portion is a 5× enlargement of the left, showing the GaAs cap, $(Al_{0.9}Ga_{0.1})_2O_3$, and the GaAs substrate. Figure 5.13 (b) shows the same 5-μm diameter hole after an additional CAIBE, with the $(Al_{0.9}Ga_{0.1})_2O_3$ masking layer still preserved. The etch depth in the GaAs substrate has increased from 550nm [in Figure 5.13 (a)] to 1.1μm [in Figure 5.13 (b)] after the second CAIBE etching.

As the rates and anisotropy of the etching vary with the size of the structures, these relatively large markers only give us a rough idea of the etch depth and profile of our samples. To get a clearer picture of the actual etching process in small holes, we have also fabricated line gratings that have similar lateral dimensions as the hole arrays. The line gratings are etched using the same procedures, and are cleaved prior to electroplating. Figure 5.14 shows a cross-sectional view of eight lines that have been

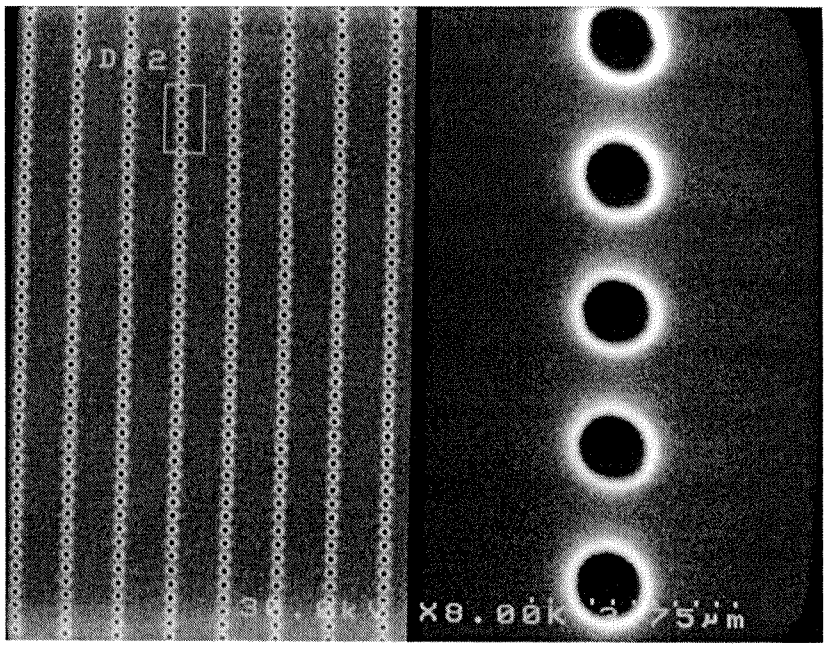

(a)

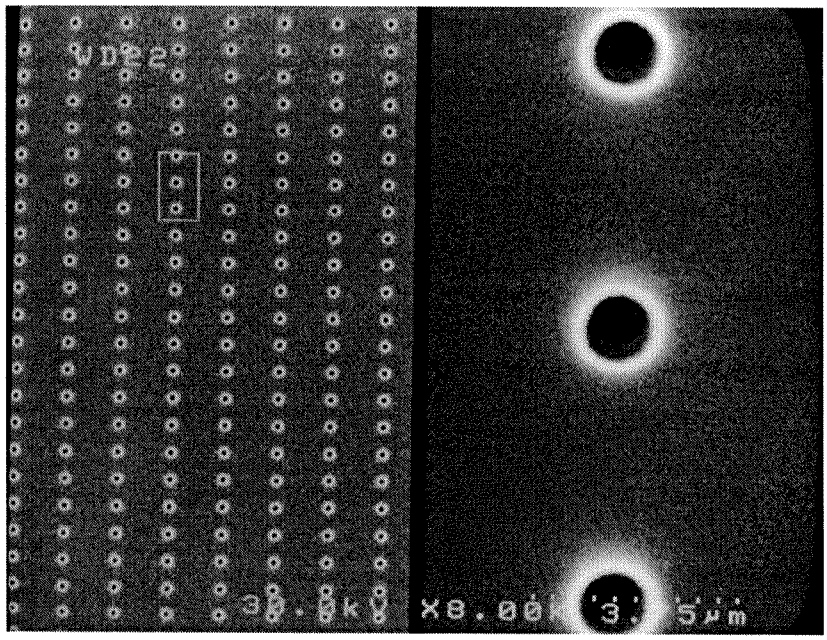

(b)

Figure 5.12: SEM images of arrays of etched holes in the GaAs cap/$(Al_{0.9}Ga_{0.1})_2O_3$/GaAs substrate after CAIBE and oxidation (left). The holes are 120nm in diameter, with a 0.25 (a) and 0.5μm (b) spacing in the down-track direction and 1μm spacing in the cross-track direction. The right portion of each figure represents a 10$\times$ enlargement of the etched holes on the left.

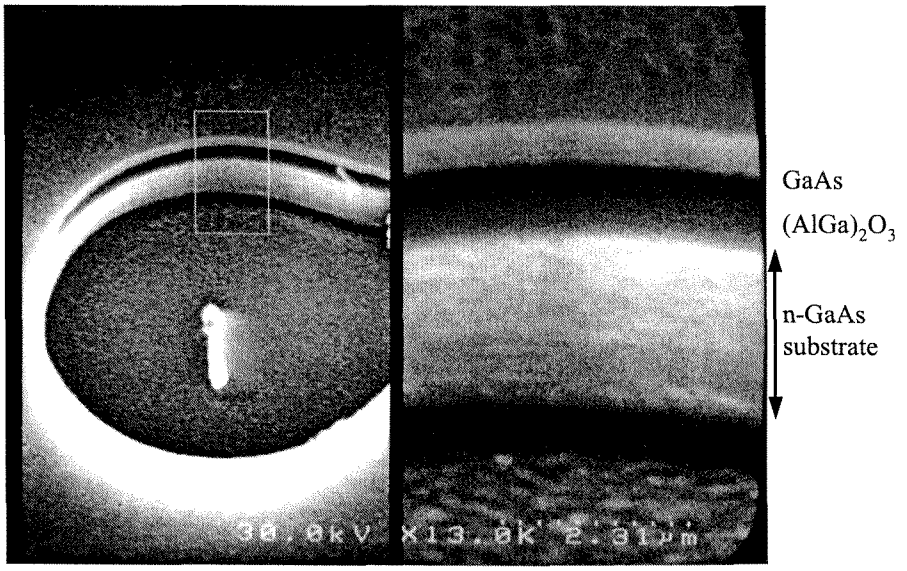

(a)

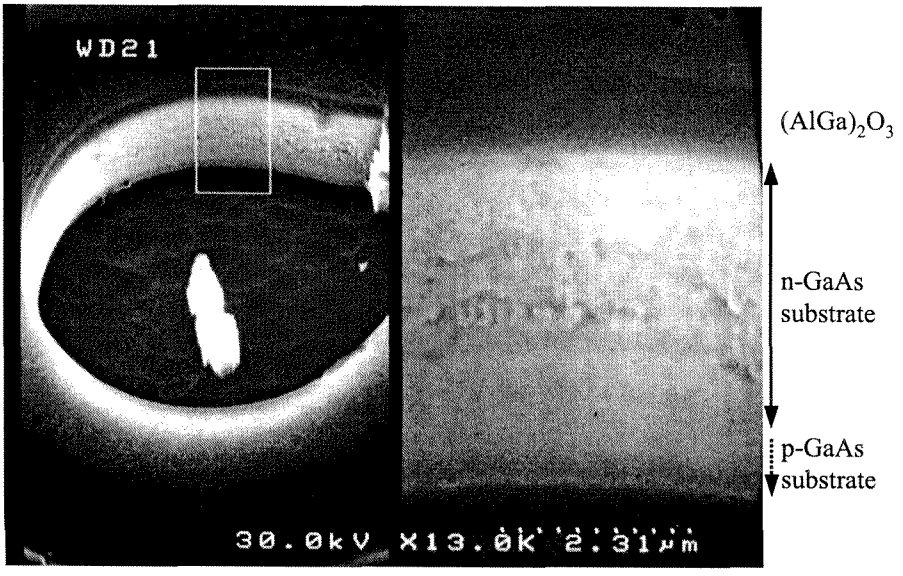

(b)

Figure 5.13: (a) A 38° tilted view of a 5-μm diameter marker after CAIBE and oxidation. The right portion if a 5× enlargement of the left, showing the GaAs cap, $(Al_{0.9}Ga_{0.1})_2O_3$, and the GaAs substrate. (b) The same marker after additional CAIBE etching.

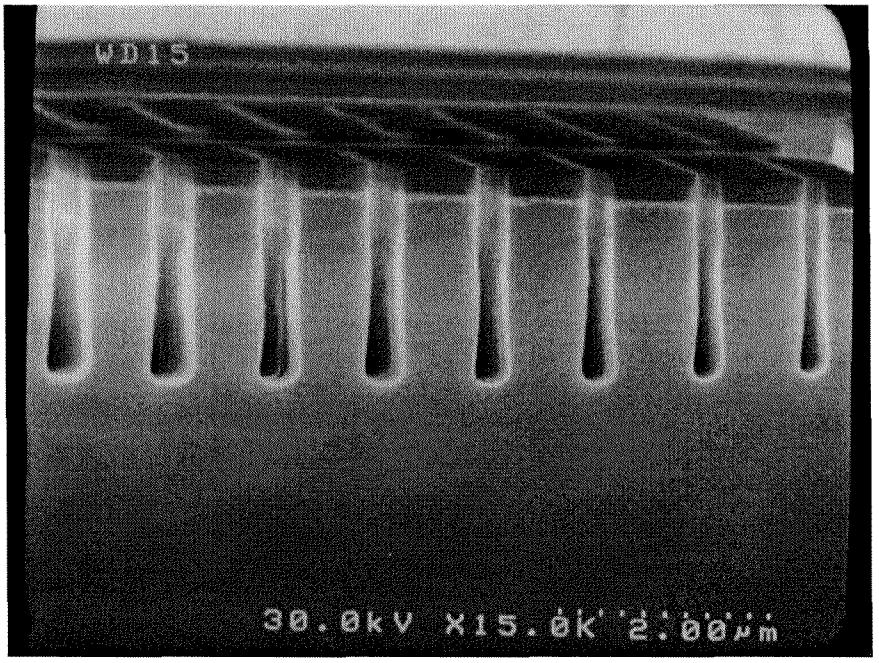

Figure 5.14: Cross-sectional view of eight cleaved lines after oxidation and two addition CAIBE.

cleaved after three CAIBE procedures (2min each run), with the top darker layer being the remaining $(Al_{0.9}Ga_{0.1})_2O_3$ mask. The lines have average widths that increase from 190nm (right) to 410nm (left) in the image, and etch depths that range from 1.8μm (right) to 2.1μm (left). These correspond to aspect ratios of approximately 9:1 to 5:1 respectively. The sidewall profile and etch depth of the trenches in the figure suggest the high anisotropy of the chemically assisted ion beam etching process, as well as the robustness of the $(Al_{0.9}Ga_{0.1})_2O_3$ layer as an ion etch mask for the GaAs substrate.

5.6 Steam oxidation

5.6.1 Kinetics of thermal oxidation of AlGaAs alloys

According to Choquette et al. [70], the following reactions take place during the wet oxidation of AlAs:

$$2\,AlAs + 6\,H_2O(g) = Al_2O_3 + As_2O_{3(l)} + 6\,H_2$$

$$\Delta G^{698} = -473kJ/mol \tag{5.2}$$

$$As_2O_{3(l)} + 3\,H_2 = 2\,As + 3\,H_2O(g)$$

$$\Delta G^{698} = -131kJ/mol \tag{5.3}$$

$$As_2O_3(l) + 6\,H = 2\,As + 3\,H_2O(g)$$

$$\Delta G^{698} = -1226kJ/mol \tag{5.4}$$

If AlAs is replaced with GaAs in Equation 5.2, we then have $\Delta G^{698} = +10\,\mathrm{kJ/mol}$. So by substituting Al with Ga in $Al_xGa_{1-x}As$, Equation 5.2 will be made less favorable. Thus wet oxidation rate is retarded as the Ga content increases [70].

During the oxidation procedure, the $Al_{0.9}Ga_{0.1}As$ layer underneath the GaAs cap is oxidized laterally through the hole array patterns. The oxidation rate is highly dependent on the Al content in the AlGaAs layers as well as the furnace temperature. Thus, calibration for the specific composition and thickness of the AlGaAs layer, as well as the furnace environment is necessary. Figure 5.15 (a) shows an SEM image of an array of etched holes of 225nm diameter, 0.5μm apart in the y direction and 1μm apart in the x direction, that has been oxidized partially in the lateral direction. The oxide extent is 250nm after 30min in the furnace environment described earlier. The oxidation process seems to be isotropic in the $Al_{0.9}Ga_{0.1}As$ layer. The unoxidized portion of the AlGaAs layer has been removed by further CAIBE. This is more obvious in the 38° tilted view of the same array in Figure 5.15 (b), where the darker background is the GaAs substrate, and the brighter stripe-like structures are the $(Al_{0.9}Ga_{0.1})_2O_3$ formed around the hole array patterns. The sidewalls of the etched holes can be observed through the $(Al_{0.9}Ga_{0.1})_2O_3$ layer, and they reveal the high anisotropy of the ion etching process. Although the structures in Figure 5.15 are sufficient for electroplating Ni columns, it is preferable to have a very smooth and robust surface, including the areas between the columns, for proper slider contact in subsequent magnetic characterization. Therefore, longer oxidation times are necessary before additional CAIBE and electroplating. Figure 5.16 (a) shows the top view of two track arrays that have been completely oxidized between the columns even in

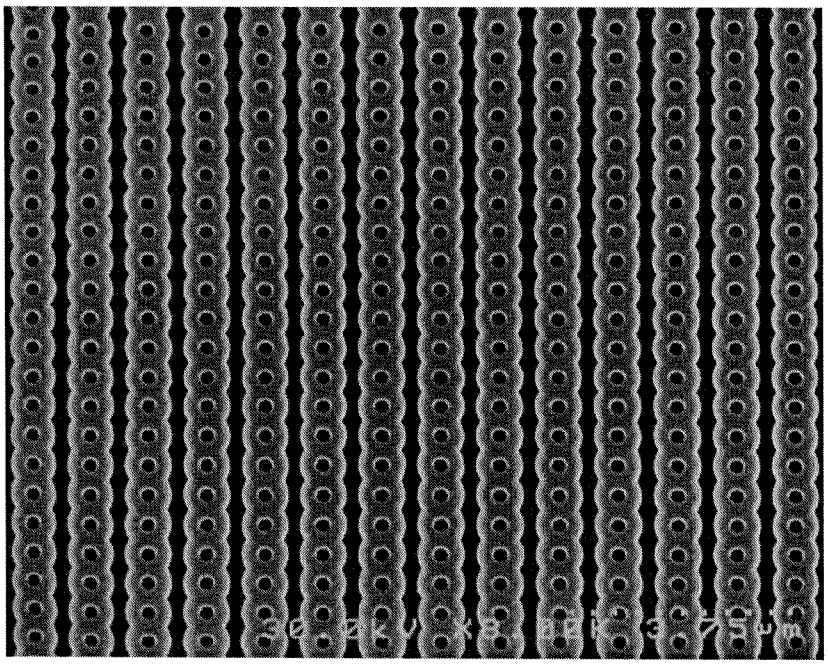

(a)

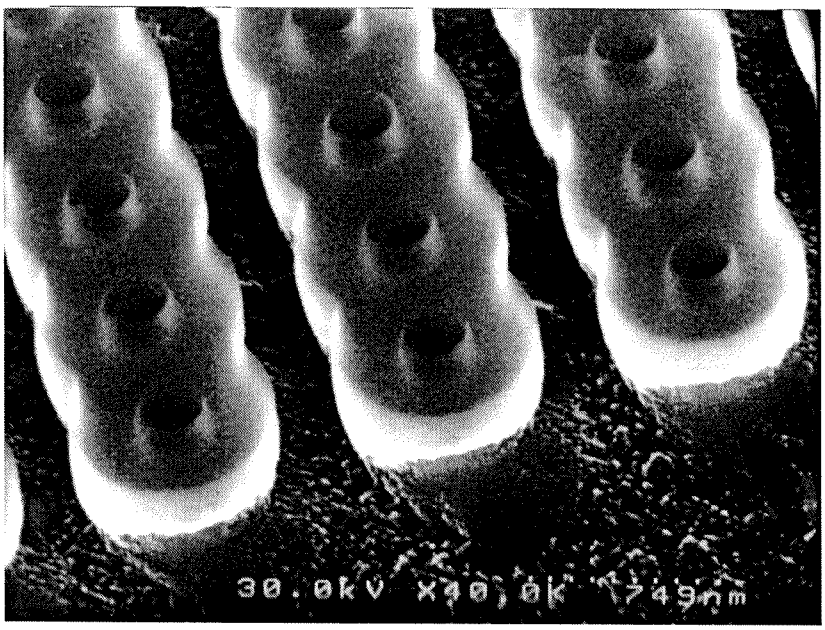

(b)

Figure 5.15: (a) SEM image of an array of etched holes of 225nm diameter, 0.5 and 1μm apart in the y and x direction, respectively, that has been partially oxidized in the lateral direction. (b) A 38° tilted view of the same array in (a).

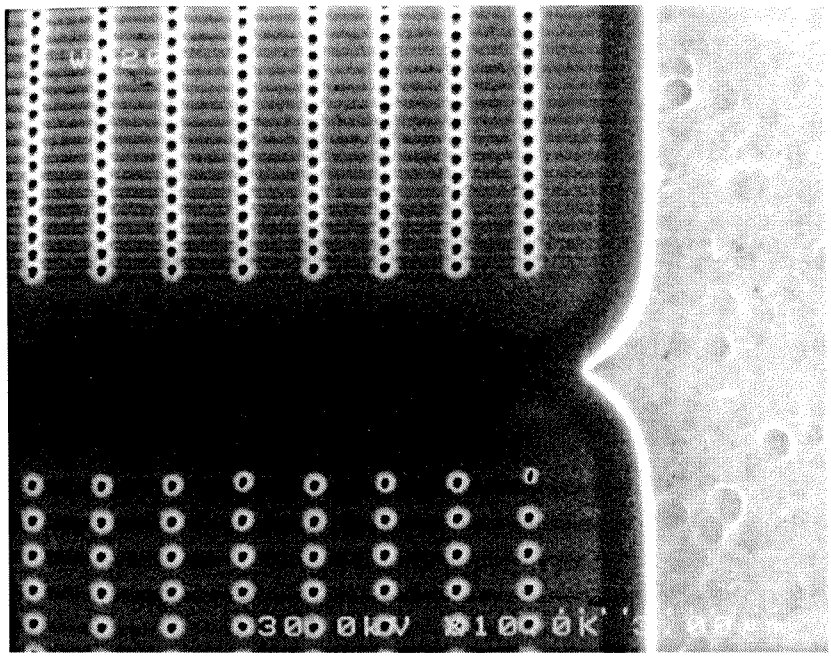

(a)

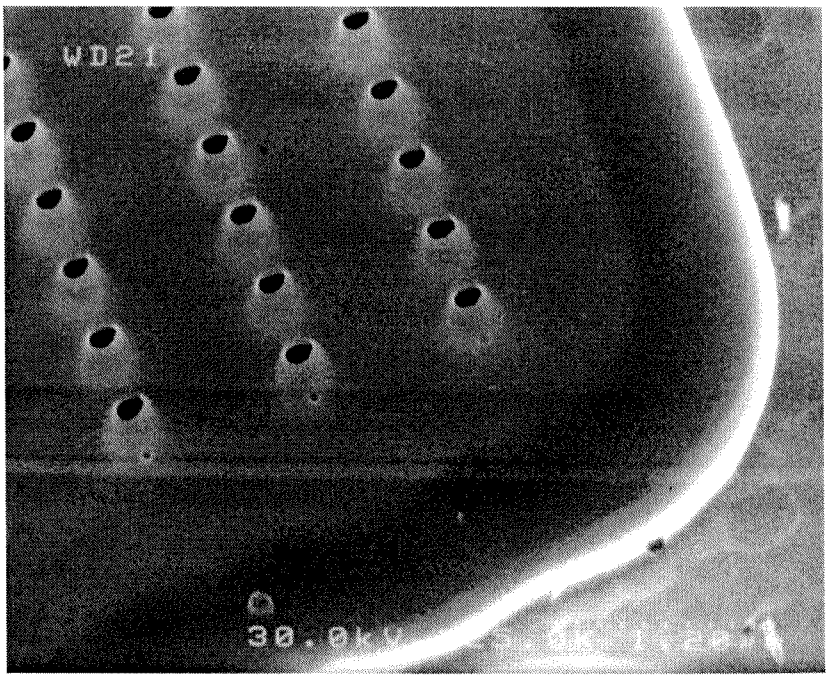

(b)

Figure 5.16: (a) Top view of two track arrays that have been completely oxidized in between the columns even in the cross-track direction (1μm spacing). (b) A 38° tilted view of the bottom array (0.5μm spacing in the down-track direction) in (a).

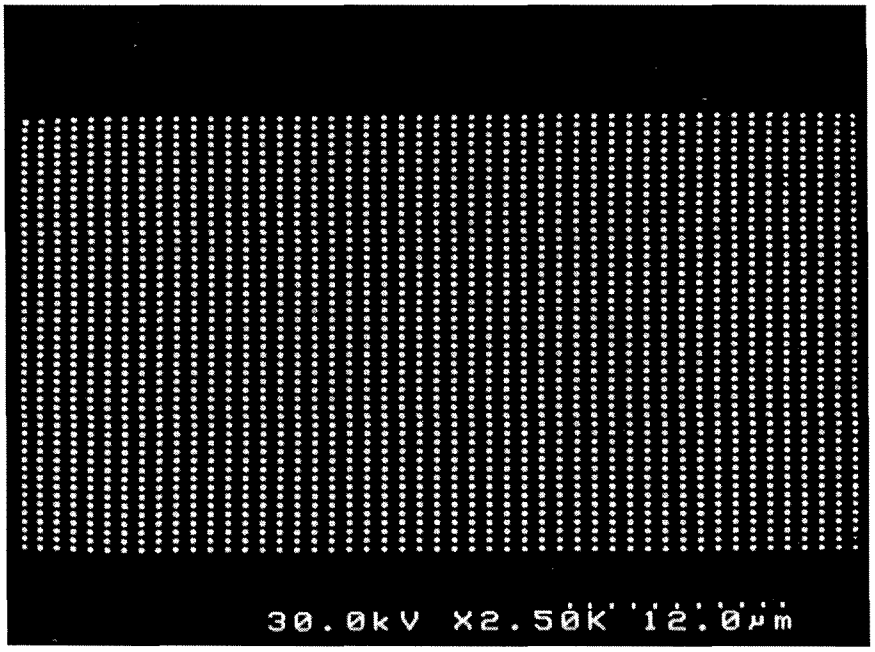

Figure 5.17: 50×50 electroplated Ni column array of 200nm diameter, with a 0.5μm spacing down track and 1μm spacing cross track.

the cross-track direction (1μm spacing). The $(Al_{0.9}Ga_{0.1})_2O_3$ extent is 1.67μm after 2h of oxidation. Once again, the unoxidized AlGaAs has been etched away by CAIBE after oxidation, and the $(Al_{0.9}Ga_{0.1})_2O_3$ mask remains intact, as can be seen in the tilted view in Figure 5.16 (b).

5.7 Electroplating into semiconductor

The electroplating of magnetic materials into semiconductors is still not a well-characterized process, and the quality of the electroplated magnetic structures was initially a concern. Our recent results [74] have indicated, however, that the Ni columns plated in etched holes in a conductive GaAs substrate have similar magnetic properties to the Ni columns plated on a metallic seeding layer. We therefore continue to use electroplating to form the Ni columns used in our patterned media work.

Figure 5.17 shows a 50×50 electroplated Ni column array of 200nm diameter, with a 0.5μm spacing down track and a 1μm spacing cross track, embedded in an $(Al_{0.9}Ga_{0.1})_2O_3$/GaAs substrate. Pulse plating is preferred over dc plating since the

former is believed to have more "throwing" power, which should facilitate the filling of Ni into the high aspect ratio holes in the substrate [75]. It can be seen from Figure 5.17 that each hole is evenly filled, and the plating seems to be very uniform over a large area. As mentioned previously, the adhesion of the $(Al_{0.9}Ga_{0.1})_2O_3$ layer to the semiconductor substrate is critical during the electroplating process. If the adhesion is poor, we find that the plating may propagate laterally between the $(AlGa)_2O_3$/GaAs layers, and Ni disks will be formed along the interface, as shown previously in Figure 5.9 (b). This type of undesirable Ni disk formation underneath the surface has not been observed after the change from 100% to 90% Al content in the AlGaAs layer. With the addition of the thin graded (30% to 90% Al) layer of AlGaAs between the GaAs and $Al_xGa_{1-x}As$, the adhesion of the mask prior to the final etch has also been further enhanced. Another advantage of using AlGaAs alloys is that the linear shrinkage of oxidized AlGaAs layers (formed above 300°C) is less than that from AlAs layers [70]. The reduced shrinkage is preferable in order to preserve the small diameters of the defined holes.

Chapter 6 Magnetic characterization

Magnetic force microscopy (MFM) [76] is initially used to characterize the magnetic properties of the patterned media fabricated using the procedures described in the previous chapter. Once the electroplated Ni columns are confirmed to be magnetic using MFM, we characterize the data storage capabilities of our structures using scanning magnetoresistance microscopy (SMRM) [77].

6.1 Magnetic force microscopy

In the MFM measurement, we use a homemade MFM utilizing electrochemically etched Ni tips [78] and a fiber-optic interferometer [79] as the vibration detector. A schematic diagram of the MFM setup is shown in Figure 6.1.

The Ni tip, which is fixed to the end of a flexible cantilever, is placed very close to the surface of the sample, on a high resolution piezoelectric stage. The spring constant, k, of the cantilever is estimated to be 1–5N/m, and the quality factor, Q, is $\sim$100 in air, with a resonant frequency of $\sim$20kHz. The MFM tip diameter varies from tip to tip, and is a tradeoff between resolution and sensitivity. For higher resolution, a typical tip diameter used is 30–50nm. For higher sensitivity, which is more crucial for detecting small signals from the nanomagnets in our samples at this point, the tip diameter used is in the range of 100 to 300nm. The tip is scanned laterally on the sample surface while interacting with the stray fields emanating from the magnetic columns embedded in the sample. The measured signal is the second derivative of the magnetic field (force gradient) in the vibration direction of the cantilever, with the vibration monitored by a fiber interferometer. As the tip is scanned over the sample, the magnetic force gradients change the resonant frequency of the cantilever, which is detected by the phase change in the resonant circuit. A common ambiguity with MFM measurement is that since it is a derivative of atomic force microscopy, one

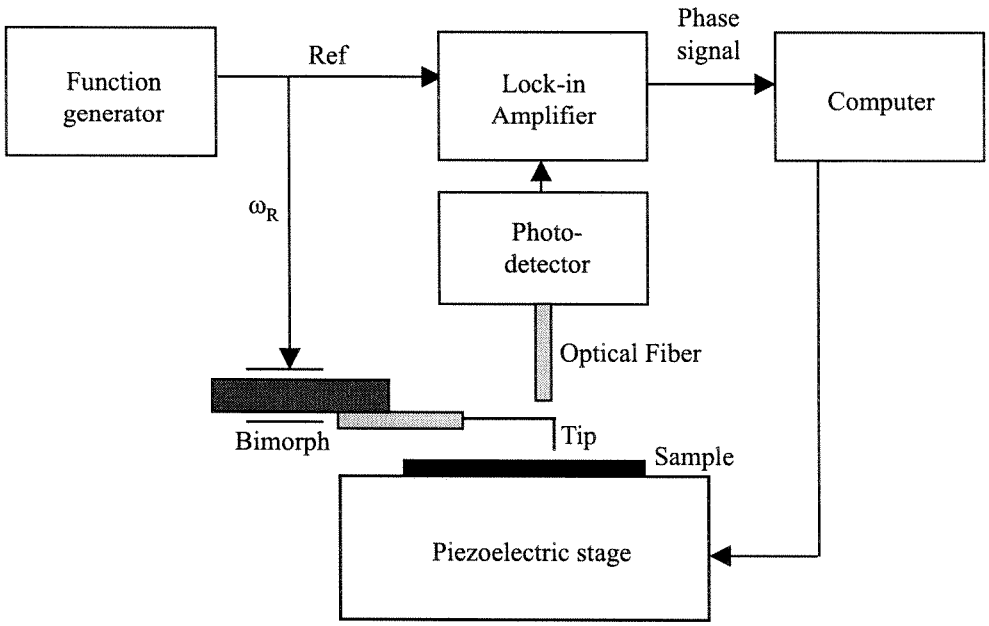

(a)

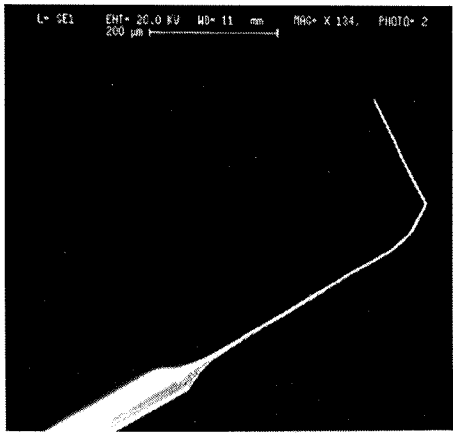

(b)

Figure 6.1: (a) Schematic diagram of a magnetic force microscope and (b) SEM image of an electrochemically etched Ni MFM tip of 100–300nm diameter.

needs to confirm that the measured forces are only due to the magnetic signal, and not the topography of the sample. A quick test can be done by lifting the magnetic tip slightly away from the sample, and rescanning it over the sample after the actual measurement. If the signal strength decreases drastically, or even disappears during the second scan, then the prior measurement is mostly likely due to the topography of the sample. Another factor that needs to be taken into account is the electrostatic signal from the sample, which can be eliminated by properly grounding both the sample and tip.

One main disadvantage of the MFM is that it is very difficult to calibrate since the signal measured is the second derivative of the magnetic field (force gradient) resulting from forces from the sample acting on the magnetic tip. Due to the second derivative nature of the measured signal, it is not possible to quantify the magnetic field from the sample [77]. With this in mind, we use the MFM only to confirm that the Ni columns embedded in our sample are magnetic, and not to obtain any quantitative information. The latter is achieved using the scanning magnetoresistive microscopy technique, described in the following section.

6.2 Scanning magnetoresistance microscopy

Scanning magnetoresistive microscopy (SMRM) is a technique in which commercial magnetoresistive read/write heads are raster scanned on the surface of magnetic samples [80]. The SMRM can be used as both a magnetic imaging device as well as a tool for evaluating whether a magnetic sample can be recorded and played back using current techniques used by the magnetic recording industry [77]. In the latter case, the SMRM acts as a static tester that emulates the recording mechanisms in a commercial hard drive. In order to convince the magnetic recording industry to consider perpendicular patterned media for future high density storage media, our first step is to demonstrate recording in prototype patterned media samples using a commercial read/write head. The SMRM is the key in providing us with the platform to accomplish this step.

Figure 6.2 shows a schematic diagram of the SMRM measurement setup [80]. In the SMRM technique, a slider (consisting of commercial inductive write poles and a magnetoresistive or spin-valve read sensor) that is used in conventional magnetic recording is raster scanned in contact with the sample. The sample is mounted on a high resolution piezoelectric stage, with a scanning range of $100\mu m \times 100\mu m$ and a nominal resolution of 1nm. The fact that the recording head has physical contact with the medium requires that the sample surface be robust and smooth, both of which are satisfied by our substrate design and sample fabrication procedures. As the areal density continues to multiply, the "flying" height will decrease drastically as well, which will in turn tighten the substrate smoothness requirement of the medium. The planarized nature of the $(Al_{0.9}Ga_{0.1})_2O_3$ surface and the embedded structure of the Ni columns both allow minimum distance between the read sensor and the medium. This is critical for maximizing the resolution and magnitude of the signal from individual magnetic columns during the SMRM measurement.

One main disadvantage of the SMRM is that its spatial resolution is limited by the physical dimensions of the read/write head. The magnetoresistive sensor used in this work has a width of $1.9\mu m$, with a shield spacing of 240nm, while the poles of the write element are 200nm apart and $2.2\mu m$ wide. Figure 6.3 (a) shows the side view of an MR element, with shields on both sides to block the emanating fields from neighboring columns, over a Ni column (left), and a schematic diagram illustrating the scanning direction of an MR read sensor during the reading process (right) in the SMRM measurement. A typical SMRM scan of a circular-shaped magnetic particle is shown in Figure 6.3 (b), in which an elongated stripe instead of a point response is resulted. The wider spatial response in SMRM images is a result of the convolution of the finite width of the MR head response with the signal from the magnetic columns. This limited spatial resolution in the y direction [according to the coordinate shown in Figure 6.3 (a)] will eventually become one of the main factors in preventing us from studying higher density patterned media configurations using SMRM with a commercial read/write head.

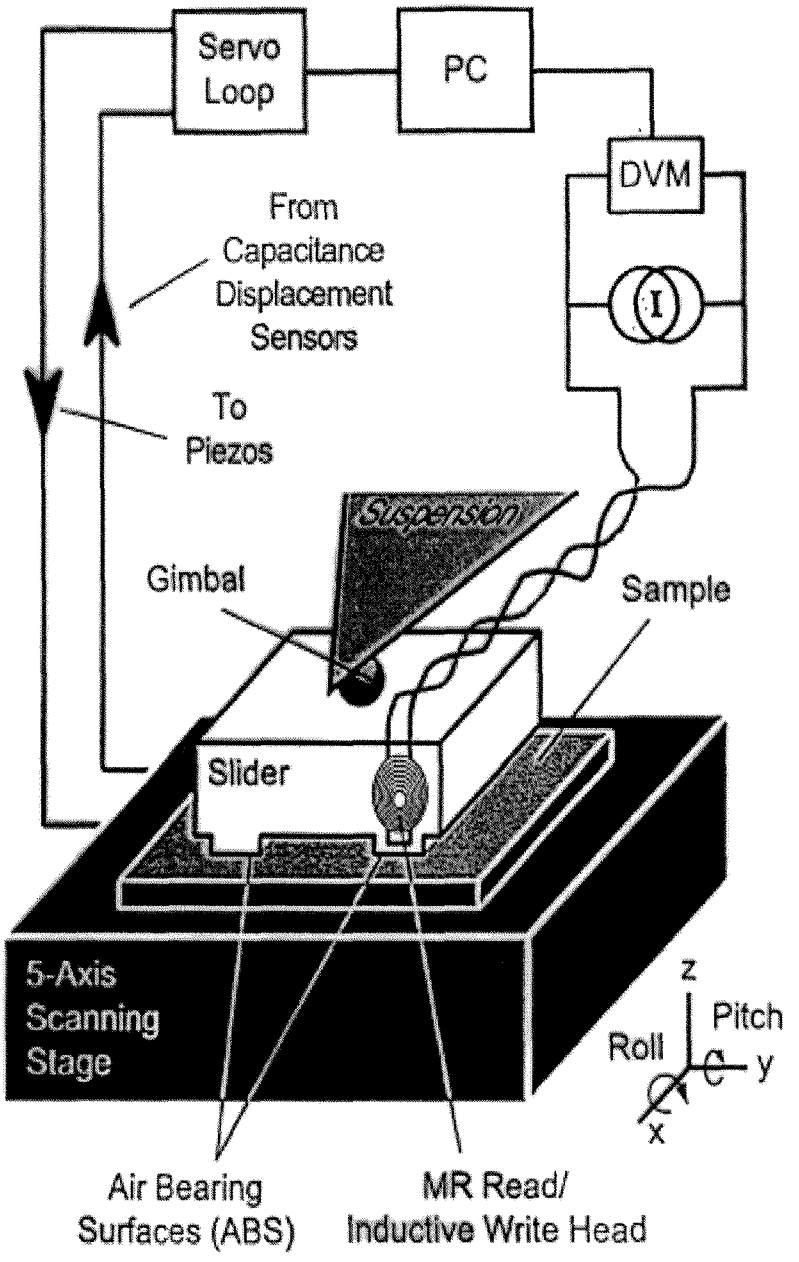

S.Y. Yamamoto and S. Schultz, Appl. Phys. Lett. **69** (21), 1996.

Figure 6.2: Schematic diagram of a scanning magnetoresistance microscope [80].

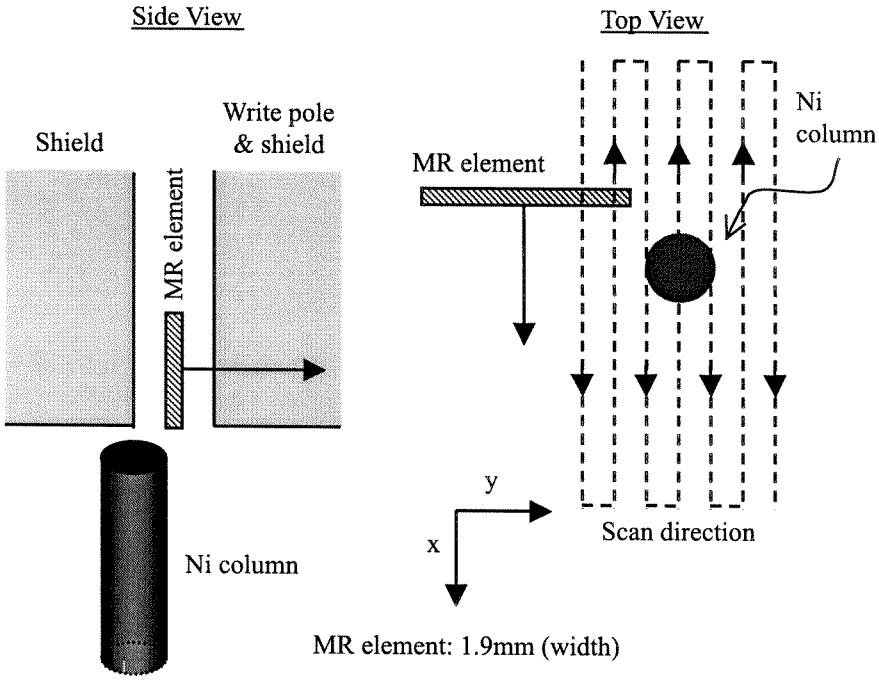

(a)

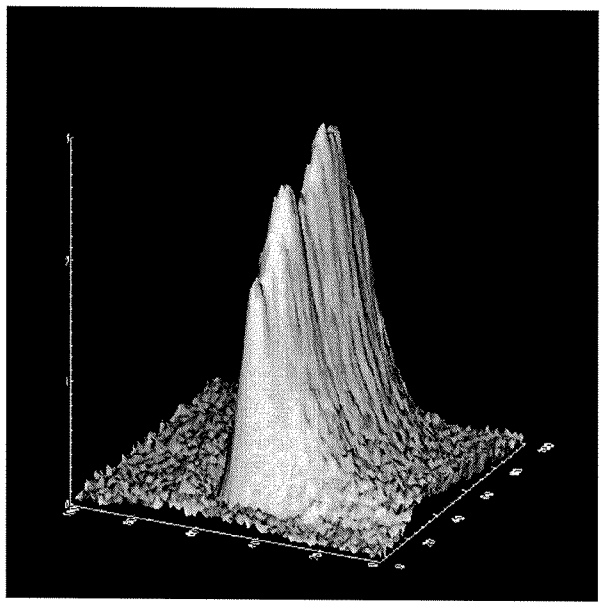

(b)

Figure 6.3: (a) Schematic diagram of the reading process in SMRM and (b) point sensitivity function of an MR element.

6.2.1 230nm diameter columns embedded in Al_2O_3/GaAs

Previous work by Yamamoto et al. [66] has shown that the MR signal from the 400nm diameter columns embedded in SiO_2 was a "dibit" type signal,i.e., both magnetization directions (black and white contrast) are present within each column, and only with the application of an external bias field was a single pole response obtained. Furthermore, the perpendicular component of the magnetic field from the bias current in the MR element was sufficient to switch the column magnetization direction, thus eliminating the possibility of reliably writing the perpendicular patterned media without erasing it through the reading process. In other words, the coercivity of the individual columns was not high enough to resist its own demagnetizing field as well as nonuniform fields experienced from the write poles and MR sensor without the assistance of an external magnetic field.

The instability in the columns has prompted us to make higher aspect ratio magnets of smaller diameter, with the desire that they will have higher coercivity, hence stability, for recording and non-destructive data retrieval using a commercial read/write head. Using the new fabrication approach described in the previous chapter, we have electroplated Ni column arrays of 6:1 aspect ratio that are embedded in a hard Al_2O_3/GaAs substrate. An SEM image of a square array of empty holes in Al_2O_3/GaAs before electrodeposition, and the same array filled with Ni single domain particles, are shown in Figures 6.4 (a) and (b), respectively. The columns are 230nm in diameter, approximately 1.4μm in height, and 2μm apart. In Figure 6.4 (c), we show a 15μm$\times$15μm scan of the same sample, imaged using magnetic force microscopy.

After switching to our new fabrication approach using Al_2O_3/GaAs as the embedding material, the first step is to determine whether our magnetic columns can be oriented in the desired magnetization direction with an external bias field. This field is produced by running a current (the direction of the current is such that the magnetic field resulted is in the desired orientation according to the right-hand rule) through a set of coils that is mounted directly underneath the sample. Figure 6.5

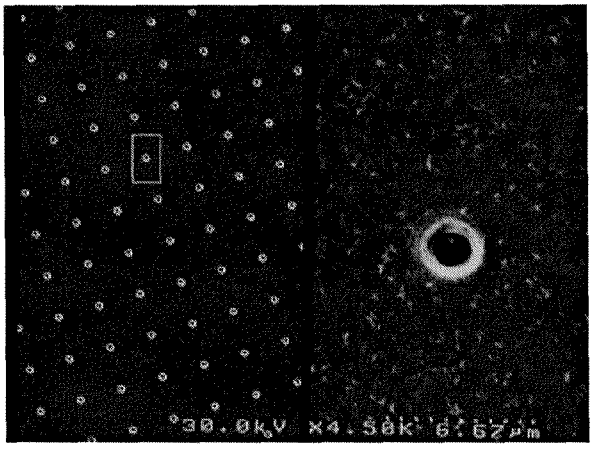

(a)

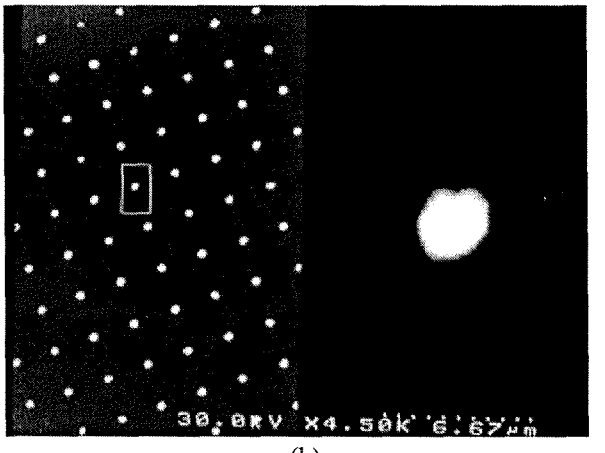

(b)

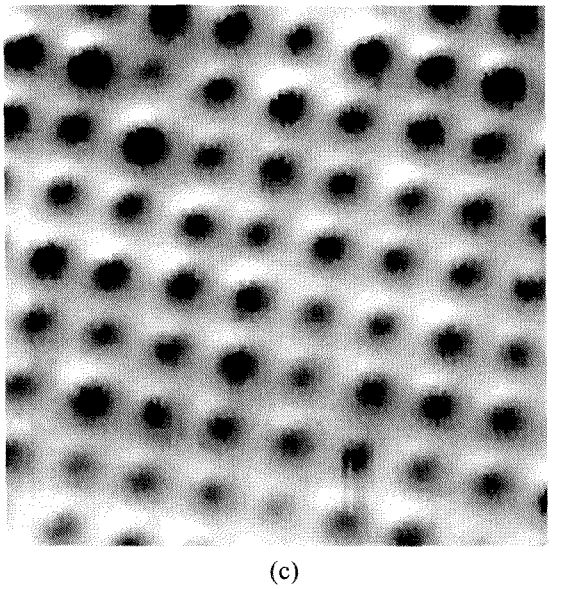

(c)

Figure 6.4: SEM images of an array of etched holes in Al_2O_3/GaAs (a) before and (b) after electroplating Ni (left), and a 10× enlargement of an etched hole and a plated column, respectively (right). A 15μm×15μm MFM image of the array is shown in part (c).

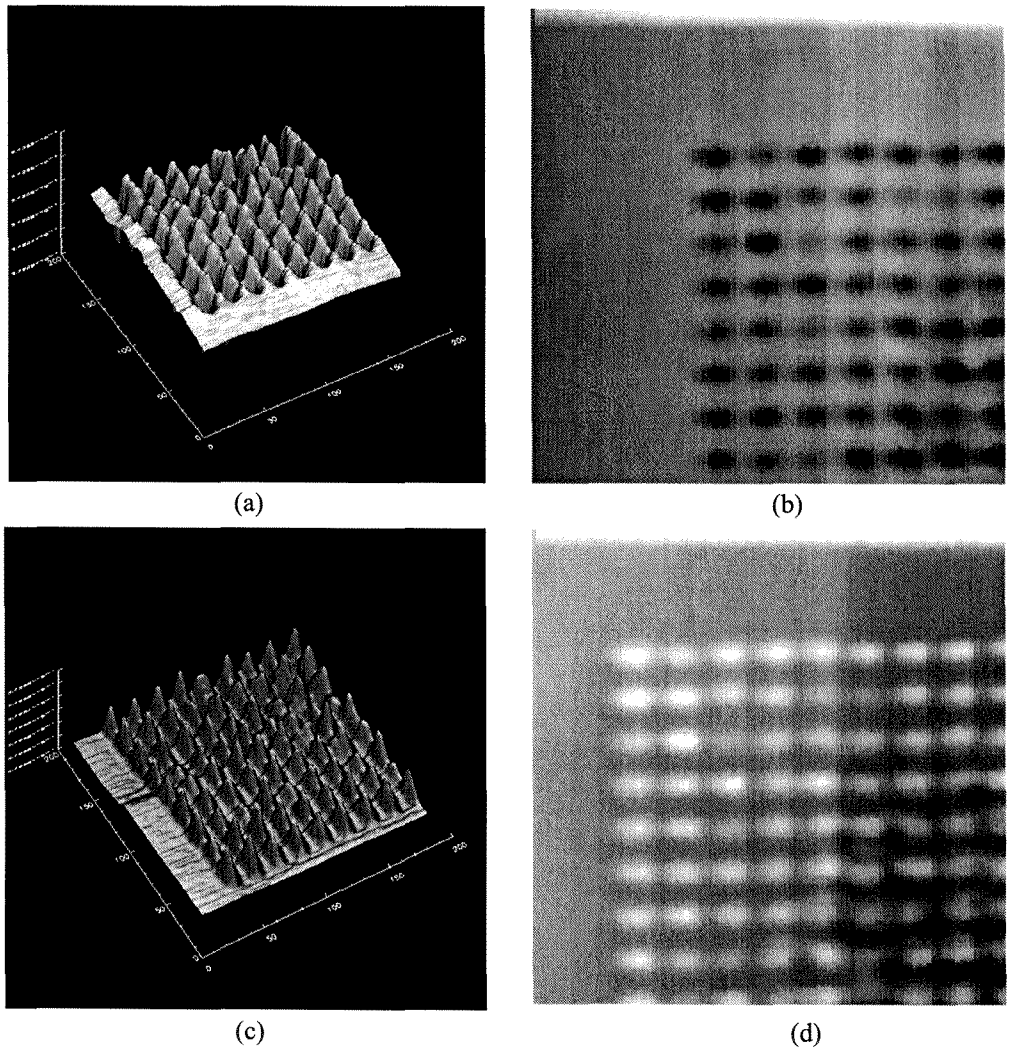

Figure 6.5: SMRM images of an array of Ni columns in Al_2O_3/GaAs saturated in the negative (b) and positive (d) externally applied magnetic field direction. Three-dimensional views of the read-back signal are shown in (a) and (c), respectively.

shows four $20\mu m \times 20\mu m$ SMRM images of an array of 250nm diameter Ni columns, embedded in an Al_2O_3/GaAs substrate, saturated in the negative (b) and positive (d) externally applied magnetic field direction. Figures 6.5 (a) and (c) show a three-dimensional view of the read-back signal, where the relative signal strength from the individual columns is more obvious than in (b) and (d).

In order to show that we have more stable, higher coercivity columns using our new fabrication approach, we need to determine whether the Ni columns in our sample will stay magnetized in the same direction as the external bias field even after the

applied field is removed. Using SMRM, the experiment just described is repeated, with the addition of a second scan using an MR head over the Ni column array after the removal of the external bias magnetic field. If the columns stay in the magnetized direction without an external field, then we can conclude that our columns are more stable than the ones previously fabricated in SiO_2, and further characterization to determine whether the columns are capable of maintaining stored information will be worthwhile. Figure 6.6 shows two SMRM images of an array of Ni columns imaged at zero field. Prior to the scans, the magnets were oriented in a direction parallel to an external magnetic field. If the magnets were unstable, we would have expected to see a dipole-type of response ("dibit" consisting of both black and white contrasts) from each magnetic column.

For a more quantitative comparison of the effects of an external bias field on the individual Ni columns, we proceed to perform a series of in and out field SMRM studies using a commerical MR head. A current coil is mounted to the bottom of our sample during the experiment. The current in the coil is varied from +100mA to +50mA to +25mA, and then through +0mA, at which time the polarity of the current is switched to sweep from −0mA to −100mA, and then again back to +100mA. This is similar to taking snapshots of the column behavior along a hysteresis loop of magnetization vs. applied field, from an external bias field of +26Oe (an equivalent of +100mA in the current coil) to +0Oe, then −0Oe to −26Oe, and finally back to +26Oe. Four sets of data from this experiment are shown in Figures 6.7 (a)–(d), where $12\mu m \times 12\mu m$ SMRM images of the same 5×5 corner array in different external fields are presented. Figure 6.7 (e) shows the single line scans that represent the MR voltage signals from each of the images. Figures 6.7 (a) and (c) show the different saturation magnetization states of the columns achieved with $\pm$26Oe of applied field, while Figures 6.7 (b) and (d) show the remanent zero field states approached from the positive and negative saturation fields, respectively.

Comparing the MR read-back signals with and without an external bias field, we found that in our current structures, the columns do provide at least a 2× larger signal when biased with an externally applied magnetic field, which indicates that they relax

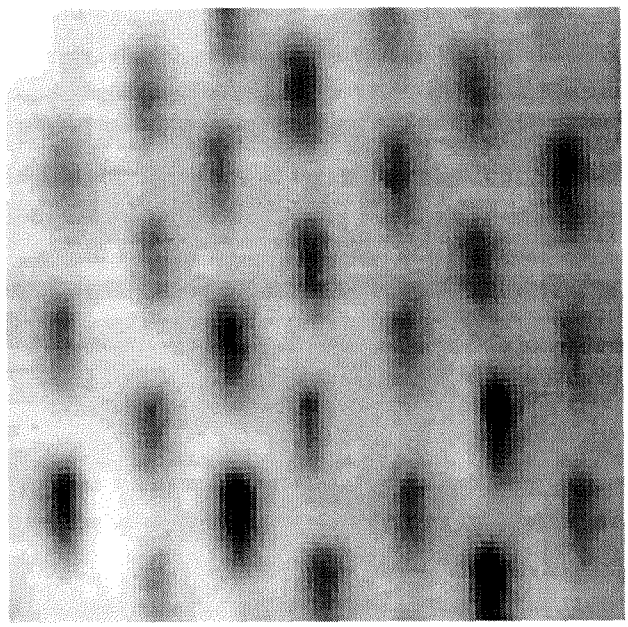

(a)

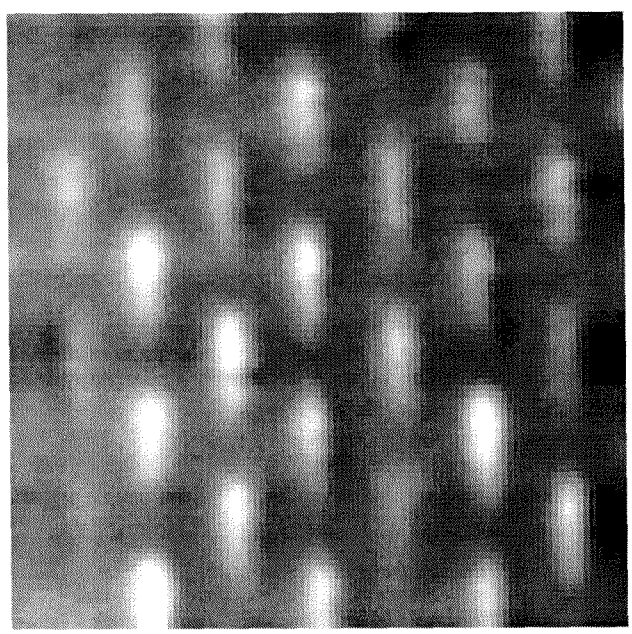

(b)

Figure 6.6: SMRM images of an array of magnets in Al_2O_3/GaAs saturated in the negative (a) and positive (b) externally applied magnetic field direction. These images are taken after the bias field has been removed, i.e., at zero external bias.

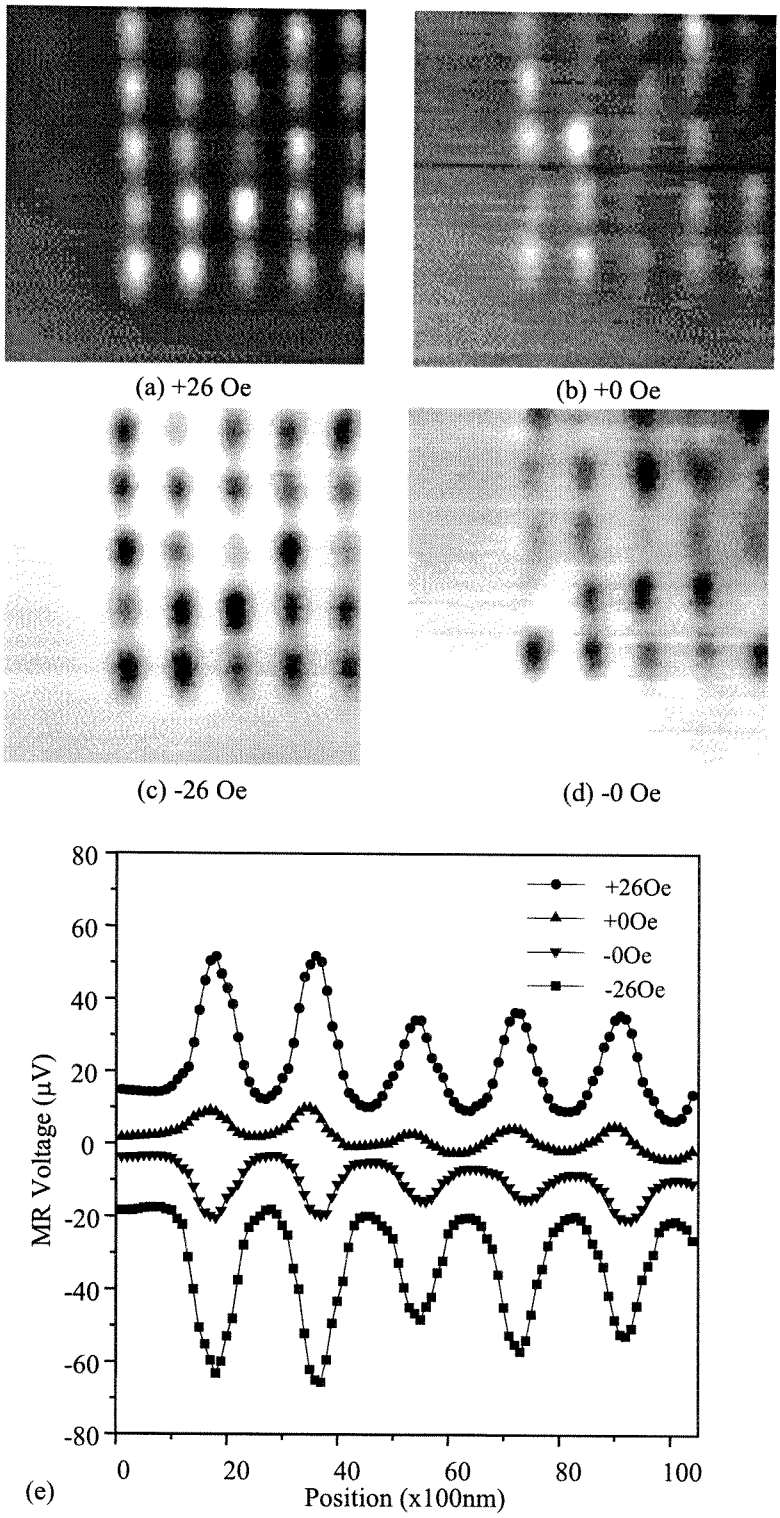

Figure 6.7: $12\mu m \times 12\mu m$ SMRM images of (a) positive saturation field of +26Oe, (b) 0Oe positive remanent state, (c) negative saturation field of −26Oe, (d) 0Oe negative remanent state, and (e) MR voltage vs. position of (a), (b), (c), and (d).

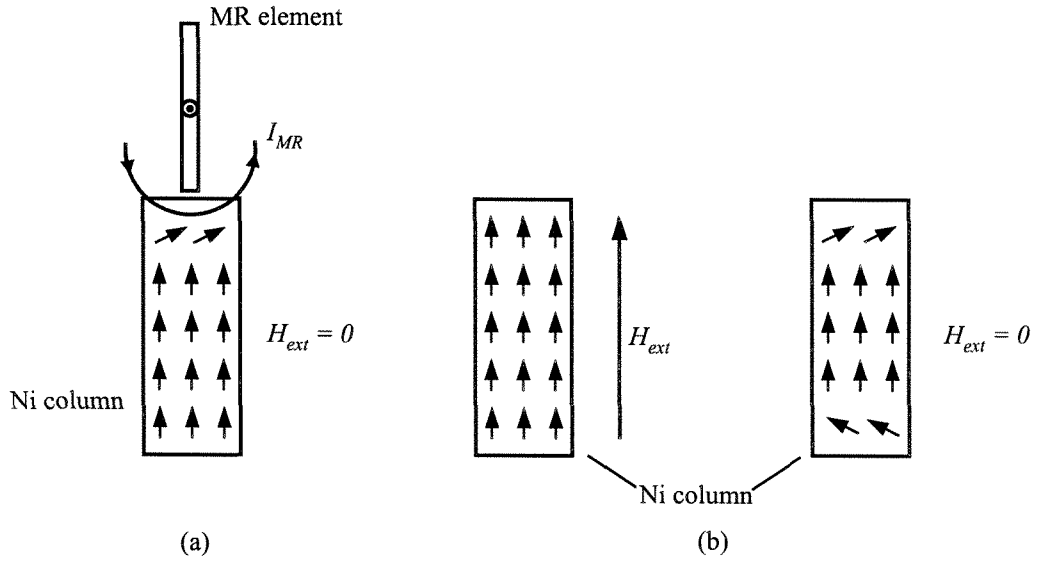

Figure 6.8: An illustration showing two possible cases where a Ni column that has a relatively large diameter can deviate from uniform magnetization throughout the column due to (a) the parallel component of the fringing field from the MR element, and (b) the removal of an external bias field alone.

into a magnetic state that deviates from a uniform magnetization throughout the particle. An illustration of two possible cases where a Ni column that has a relatively large diameter can become non-uniformly magnetized is shown in Figure 6.8. This deviation may be a result of experiencing the additional parallel component of the fringing field of the MR read element, shown in Figure 6.8 (a). Or it may merely be a result from the removal of an external bias field, H_{ext}, shown in Figure 6.8 (b). A more important observation when comparing the images of Figures 6.7 (b) and (d) is that, even though a few columns provide almost no contrast in zero field, 85% of the particles remain magnetized in the direction of the original saturation field (i.e., in the "correct" orientation), and the MR current is not sufficient to switch them when imaging at zero field. In the SMRM scans in zero field, we always obtain a single-pole response and have not observed a dibit-type response, which would have indicated a low switching field magnetic particle. The increase in H_c of the individual columns is critical for further improvement in the stability of such media, where the written information must be read nondestructively. We find the width of the column

MR response to be 600–700nm, which is much larger than the column diameter. Such a wide response from a single column has been observed previously [66]. To our knowledge, the spatial MR response of a perpendicularly magnetized cylinder has not been modeled, and we are still doing a theoretical investigation of this experimental observation.

6.3 Data storage demonstration

6.3.1 Preliminary results on data storage in patterned media

Figure 6.9 (a) shows an SMRM image that demonstrates recording of two neighboring magnetic columns at a time in perpendicular patterned media using a commercial MR head. The sample has been rotated 45° with respect to the SMRM scanning direction in order to maximize the distance between the columns. The columns here are 275nm in diameter, embedded in an Al_2O_3/GaAs substrate. Due to the large size of the individual columns and the limited spacing between them, it is very difficult to accurately place the write pole piece on top of only one column, and controlling its magnetization without affecting its neighbor. Thus, more than one column is usually switched by the write transducer during each writing process. The columns that have been switched by the MR head are shown as white (up direction) in Figure 6.9 (a). The only single column being switched is at the very bottom of the image. Since there is no column on the two adjacent sides and in the row below this corner column, there is more room to offset the write poles such that their fringing fields do not disturb any extra neighboring columns. An SEM image of the bottom view of the write poles, with the approximate locations of the Ni columns superimposed onto the image (as white filled circles) for illustration purpose is shown in Figure 6.9 (b). In this arrangement, our intention is to switch the Ni column to the immediate left of the fringing field (shown in write arrows pointing from left to right). Along with this switching, we also unintentionally switch the neighboring columns to the right of the fringing field, in the opposite magnetization direction with respect to

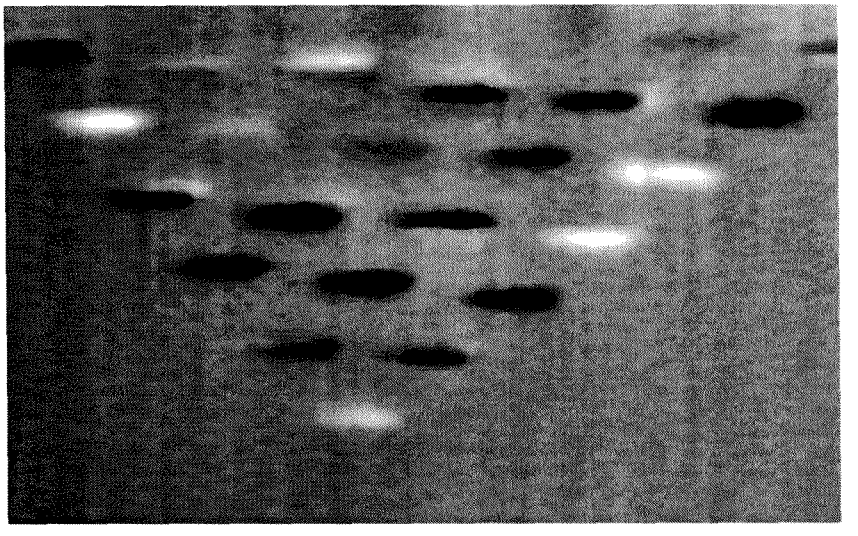

(a)

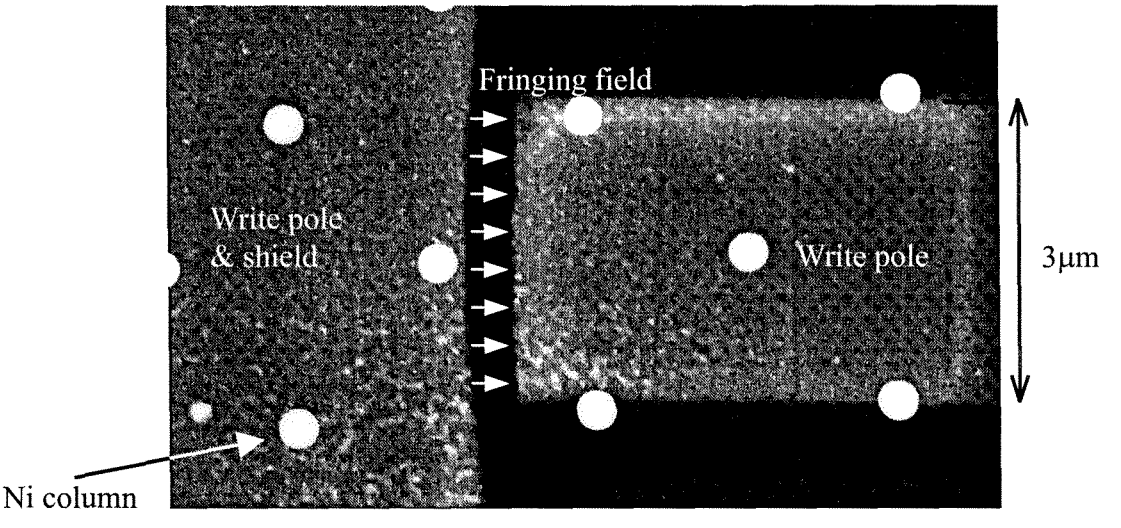

(b)

Figure 6.9: (a) First demonstration of recording (minimum of two neighboring columns at a time) in perpendicular patterned media using a commercial MR head. (b) SEM image of the top view of the write poles, with the approximate locations of the Ni columns superimposed onto the image for illustration purpose.

the single column (on the left) that we just reversed. This is sometimes unavoidable and the write poles can proceed to the right and orient these two columns to the desired direction. The two columns that are further left from the column of interest, however, also got switched by the fringing field due to their low coercivity. As a result, all three columns to the left of the write pole gap in the image are oriented in the same magnetization direction. This is undesirable if we are to demonstrate single column per bit recording. So following this, we start investigating into smaller diameter columns of 230nm.

With the smaller 230nm diameter columns, we have shown in the previous section that they are more stable than the larger 400nm columns by Yamamoto et al., and that they do stay magnetized in the desired direction when imaged using a commercial MR head even after the bias is removed. Even though the signal at zero bias is $2\times$ smaller than that with bias, the fact that they remained in the "correct" magnetization direction has provided us with the necessary ground to determine whether it is possible to record information in each individual column. The writing is performed using the inductive write sensor while the reading is achieved using the MR read transducer.

Figure 6.10 shows a collection of 3μm$\times 22.5\mu$m SMRM images with two tracks of Ni columns oriented in various configurations using an MR head. The sample is again oriented 45° with respect to the scanning direction. In all the images, the columns appear as stripes due to the finite width of the magnetoresistive read sensor. In Figure 6.10 (a), the columns in both tracks are oriented in the down direction and appearing black, while in Figure 6.10 (b), all are in the up direction and appearing white. In Figure 6.10 (c), the columns in the top track are all in the down state, while the columns in the bottom track are in the up state. The next four images show patterns with more realistic appearance of patterned media data tracks. In Figure 6.10 (d), the top track has all the columns magnetized in the downward direction, while the bottom track is oriented in an alternating up/down sequence. Figure 6.10 (e) shows the top track again with all the columns written down, while the bottom track has every third magnetic column written up. In Figure 6.10 (f), alternating pairs of columns are oriented in the up/down sequence, while the bottom track is all down.

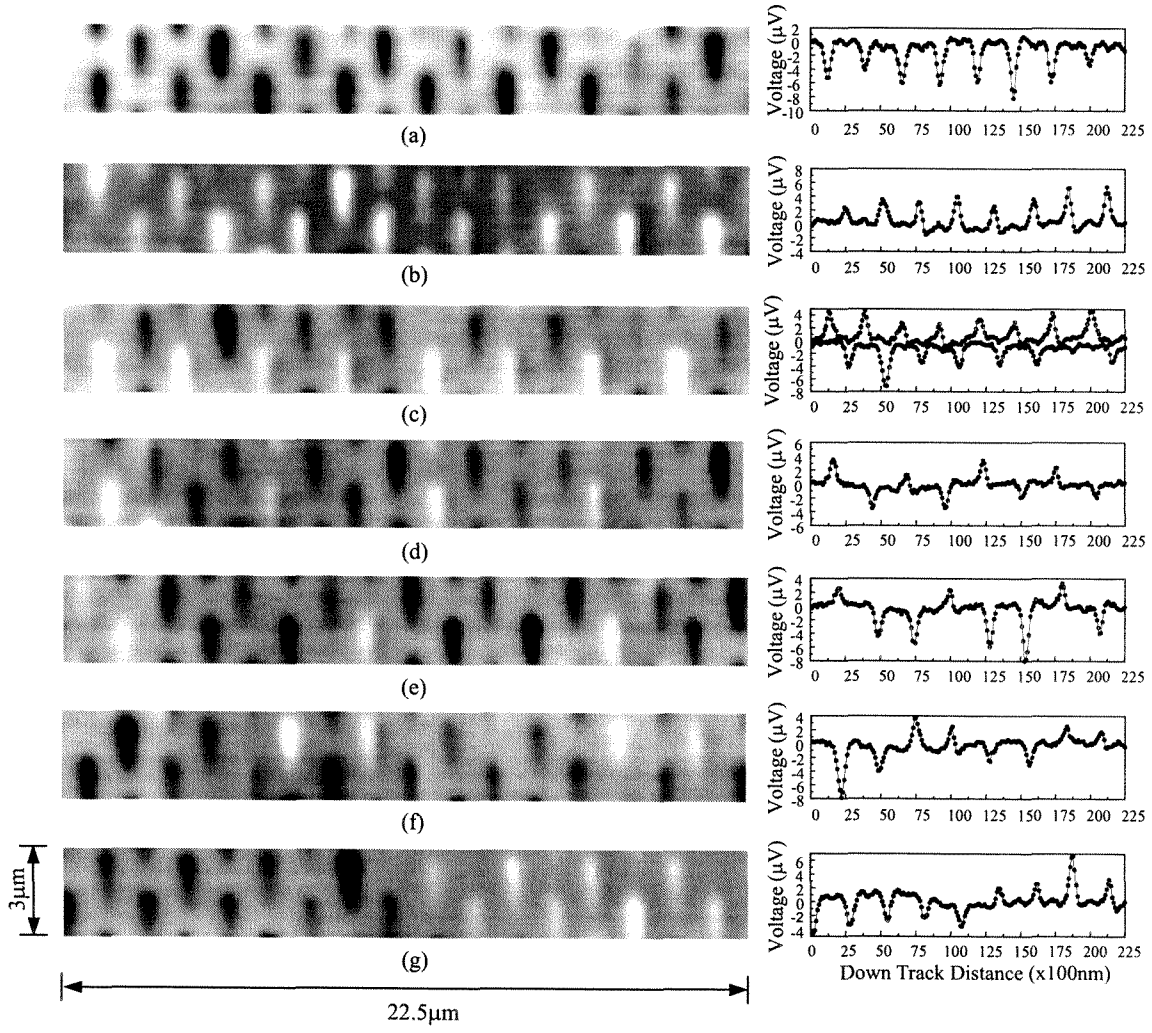

Figure 6.10: A collection of 3μm$\times 22.5\mu$m SMRM images showing recording in the individual Ni columns in various configurations. The line scans representing the MR read-back signals of the tracks in the gray scale images are shown on the right.

Finally, in Figure 6.10 (g), the left half of the array is down, and the right half is up. From the line scans that represent the MR read-back voltages shown on the right of Figure 6.10, we see that the signals are only around 5μV and there are variations in the signal strength from column to column in each track. These results, however, are still very encouraging. The observations only made us more convinced that it is important to decrease the diameter of the Ni columns so that there will be less deviation from the uniform magnetization direction in the column at zero external bias. We believe that the smaller diameter columns will allow us to achieve more stable and higher coercivity magnets for recording demonstration purposes.

6.3.2 0.16Gbits/in.^{2} recording

Using the modified fabrication procedures described in the previous chapter, we have fabricated high aspect ratio perpendicular 170nm diameter Ni columnar particles embedded in a hard $(Al_{0.9}Ga_{0.1})_2O_3$/GaAs substrate [74]. An SEM image of the square array of empty holes in $(Al_{0.9}Ga_{0.1})_2O_3$ before electroplating, and the same array filled with Ni single domain particles, are shown in Figures 6.11 (a) and (b), respectively. The columns are 170nm in diameter, approximately 900nm in height, and 2μm apart. In Figure 6.11 (c), we show a 12μm$\times$12μm scan of the same sample, imaged using magnetic force microscopy.

After confirming that the Ni columns are magnetic, we then use SMRM to investigate whether the smaller diameter columns (170nm) have higher coercivity than the larger diameter columns (230nm) fabricated and characterized previously. This is done by applying an external magnetic field in the perpendicular direction relative to the sample surface, i.e., parallel to the length of the embedded Ni columns, to orient all the columns in one of the two magnetization directions and scanning the MR sensor to detect the read-back voltages from each of the columns. Consequently, the external bias field is removed, and the MR sensor is scanned over the same array of columns again to determine the emanating fields from the columns. These scan conditions are repeated for the reversed external bias field and zero field (approach-

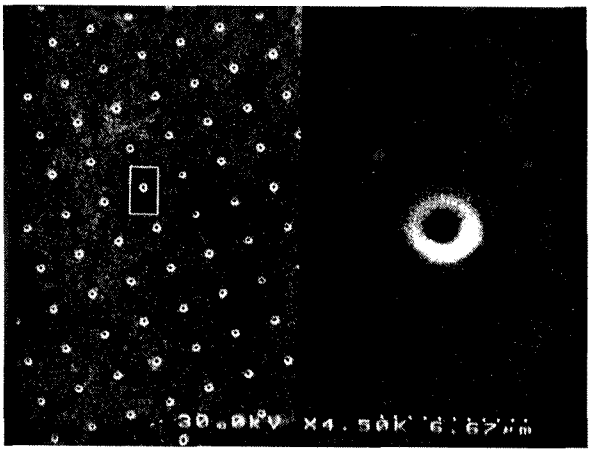

(a)

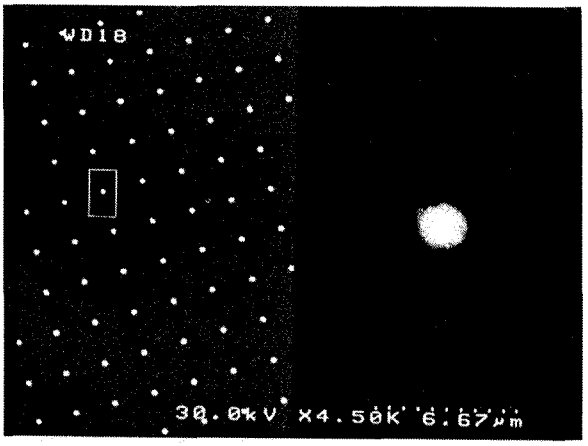

(b)

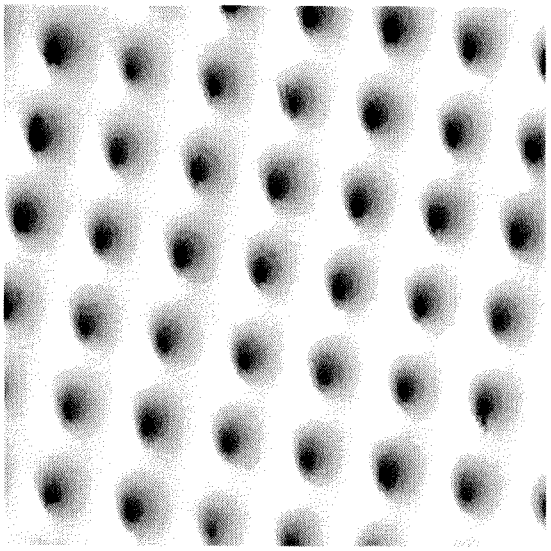

(c)

Figure 6.11: SEM images of an array of etched holes in $(Al_{0.9}Ga_{0.1})_2O_3$/GaAs (a) before and (b) after electroplating Ni (left), and a 10× enlargement of an etched hole and a plated column, respectively (right). A 12μm×12μm MFM image of the array is shown in part (c).

ing from the opposite direction). Figures 6.12 (a)–(d) show the resulting series of in and out of field SMRM scans of a square array of 170nm diameter columns that are spaced 2μm apart, with the line scans of the read-back voltages shown in (e). Compared with Figures 6.7 (a)–(e), it is evident that the difference between the MR read-back signals with and without an external bias field from the 170nm diameter columns (20μV vs. 15μV, respectively, in one of the columns) is much smaller than in the case of the 230nm diameter columns(40μV vs. 10μV, respectively, in one of the columns). This implies that the smaller diameter columns do provide a higher coercivity, and are more "single domain" than the larger ones. It is also very likely that there is less tilting of the magnetization away from the perpendicular direction, especially along the internal boundaries of the Ni columns (see Figure 6.8). It is noted here that the MR signal detected from the 230nm diameter columns has a larger amplitude than that from the 170nm diameter columns. This is believed to be a result of the increased effective magnetic charge resulting from larger diameter columns.

Following this, we use the technique of SMRM to evaluate whether our perpendicular patterned media samples can be read and written with current technology. The MR sensor used has a width of 1.9μm, and a shield spacing of 240nm, while the poles of the write element are 200nm apart and 2.2μm wide. We have oriented the sample so that the square array of columns is at 45° to the SMRM scan direction, in order to maximize the separation between the particles that we attempt to read and write. An MR bias current of 7mA was used in all the SMRM images shown in Figure 6.13. In these images, the columns appear as stripes due to the finite width of the magnetoresistive read sensor.

Figure 6.13 [74] shows a collection of 3.5μm$\times$18μm SMRM images demonstrating that prototype single column per bit patterned media data tracks can be controllably written, and then read back using a commercial inductive write and magnetoresistive read element, respectively. For writing, we use the perpendicular components of the fringing field from the write element poles to orient the columns in the desired direction. A current of 5mA through the write element is sufficient to switch the magnetization of the columns. Six different configurations of three adjacent tracks

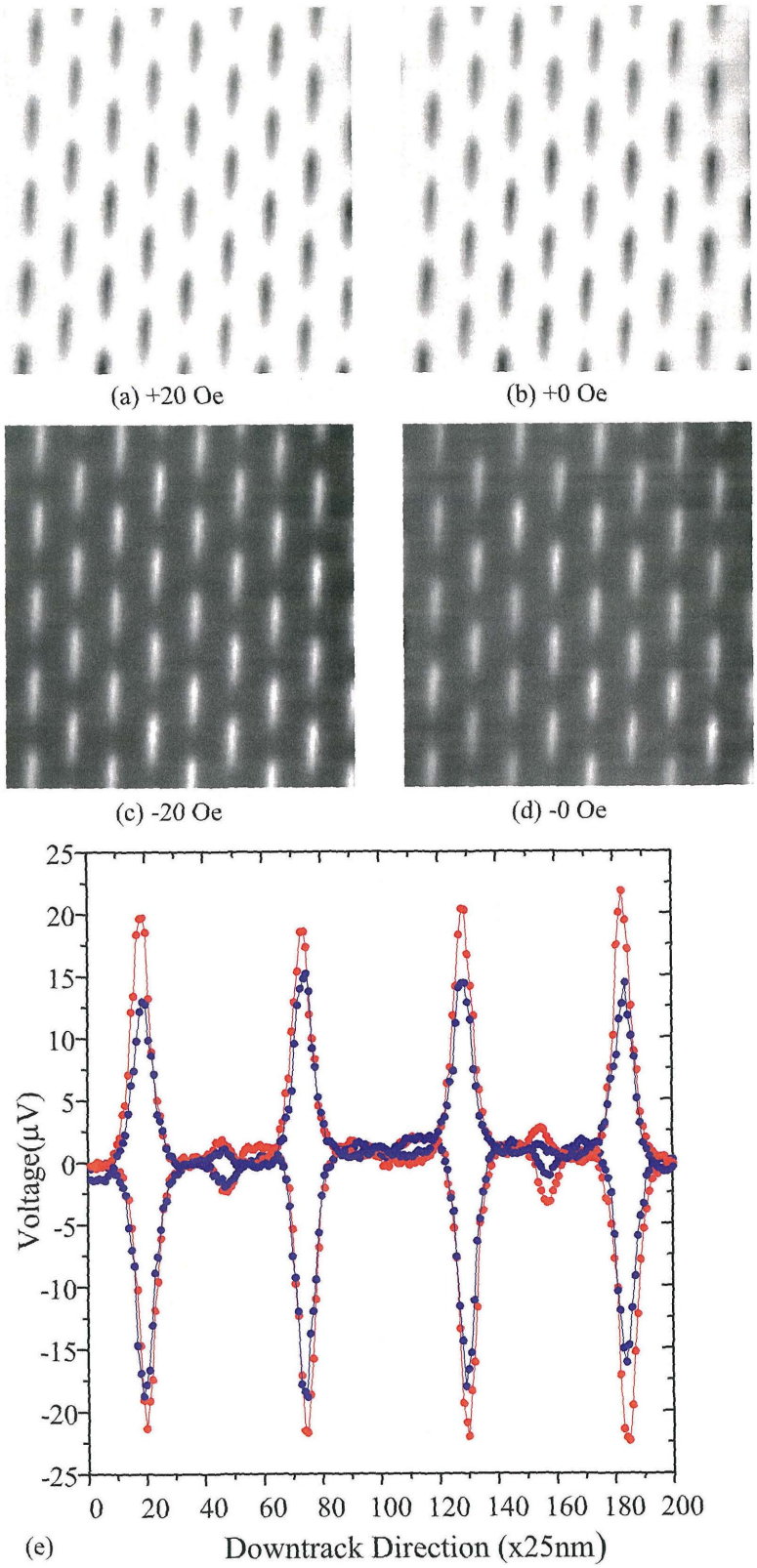

Figure 6.12: $12\mu m \times 12\mu m$ SMRM images of (a) positive saturation field of +20Oe, (b) 0Oe positive remanent state, (c) negative saturation field of -20Oe, (d) 0Oe negative

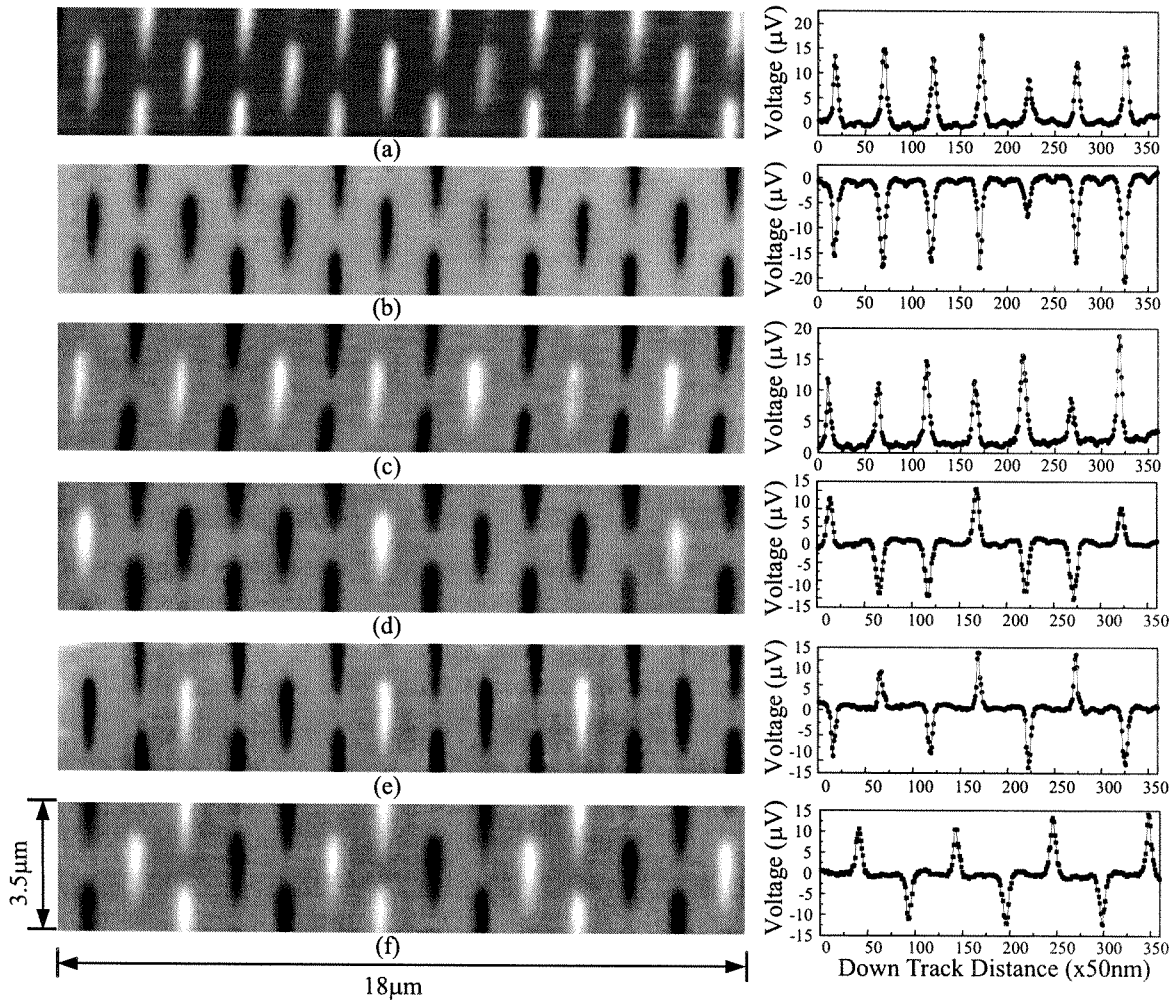

Figure 6.13: A collection of $3.5\mu m \times 18\mu m$ SMRM images, demonstrating controllable writing of single column per bit perpendicular patterned media data tracks, is shown on the left side. The line scans of the center data tracks are shown on the right.

are shown. In Figure 6.13 (a), the columns in all three tracks are oriented in the up direction and appearing white, while in Figure 6.13 (b), all are in the down direction and appearing black. In Figure 6.13 (c), the columns in the center track are all in the up state, while the columns in the side tracks are in the down state. The next three images show patterns with more realistic appearance of patterned media data tracks. In Figure 6.13 (d), the center track has all the columns oriented in an alternating up/down sequence, while the side tracks are all down. Figure 6.13 (e) shows the center track with every third magnetic column written up, while the side tracks have all the columns written down. In Figure 6.13 (f), all three tracks are written in the alternating up/down sequence. The single line scans, next to each gray scale image, show the magnetoresistive voltage signal from the center data track configuration. These voltages represent the read-back signal that would be used for further data processing and retrieval in a patterned media storage system.

The signal amplitude is an order of magnitude smaller than typically observed in continuous thin-film magnetic recording systems. This is expected, since the effective magnetic charge of a single magnetic domain that the sensor detects is approximately an order of magnitude smaller than the effective magnetic charge that the larger (i.e., 2μm) data tracks provide [66]. Simulations of the magnetoresistive sensor spatial response using the Potter approximation [81] agree well with the linewidth of the signal that we observe. The signal amplitude is dependent of the distance between the magnetoresistive sensor and the column surface, and the variation that we observe corresponds to a 20nm height difference, which is expected in our SMRM experimental setup. We believe that we are observing the near maximum value of the signal that is theoretically expected from a uniformly magnetized single domain particle, based on the effective magnetic charge comparison. Since the magnetic field sensors used in the magnetic storage industry are continually advancing towards higher sensitivities and smaller track widths, the work we have done so far will be accordingly scaled to smaller diameter columns in the future.

6.3.3 Comparison of MR and spin-valve imaging

Since the 0.16Gbits/in.^{2} recording demonstration, we have obtained more advanced recording heads from our sponsors from the magnetic recording industry. Figure 6.14 shows a comparison in imaging the same 170nm diameter Ni columns, spaced 2μm apart, using our previous magnetoresistive read sensor and our newly obtained spin-valve read transducer. The sample is kept rotated at 45° relative to the scan direction so that we can still resolve the columns using the MR sensor. Figure 6.14 (a) shows an 18μm×4μm SMRM image taken with a 2μm wide MR sensor that has a 240nm read gap. The MR resistance was ~35Ω and the bias current used was 7mA. Figure 6.14 (b) shows the same sample imaged by a 0.8μm wide spin-valve read element with a 240nm read gap. The GMR resistance was also ~35Ω, but a lower bias current of 5mA was used instead in order to prevent excessive heating of the sensor. It is evident from these SMRM images that the spin-valve sensor resulted in a narrower cross-track response than the MR sensor. A comparison of the line scans indicating the read-back voltages from the two sensors is shown in Figure 6.14 (c). From the line scans, we see that the GMR sensor provides a 2× larger signal than the MR sensor from Ni columns of the same diameter. This improvement will allow us to detect signals from smaller diameter columns better. The continual development of improved read sensors in the magnetic recording industry will be advantageous and crucial in the patterned media research as the column diameters decrease in size to satisfy the increase in areal density. With the narrower sensors, we can now resolve the 2μm apart columns without any rotation of the sample. This is evident in the two SMRM images of a square array of Ni columns shown in Figure 6.15, that are recorded in such a way that the yellow columns represent the initials of our academic institutions: "CIT" and "UCSD".

6.3.4 1.3Gbits/in.^{2} recording

The columns described in the previous sections are 170–230nm in diameter, and have a 6:1 aspect ratio. The magnets are arranged in a square array with a 2μm column-to-

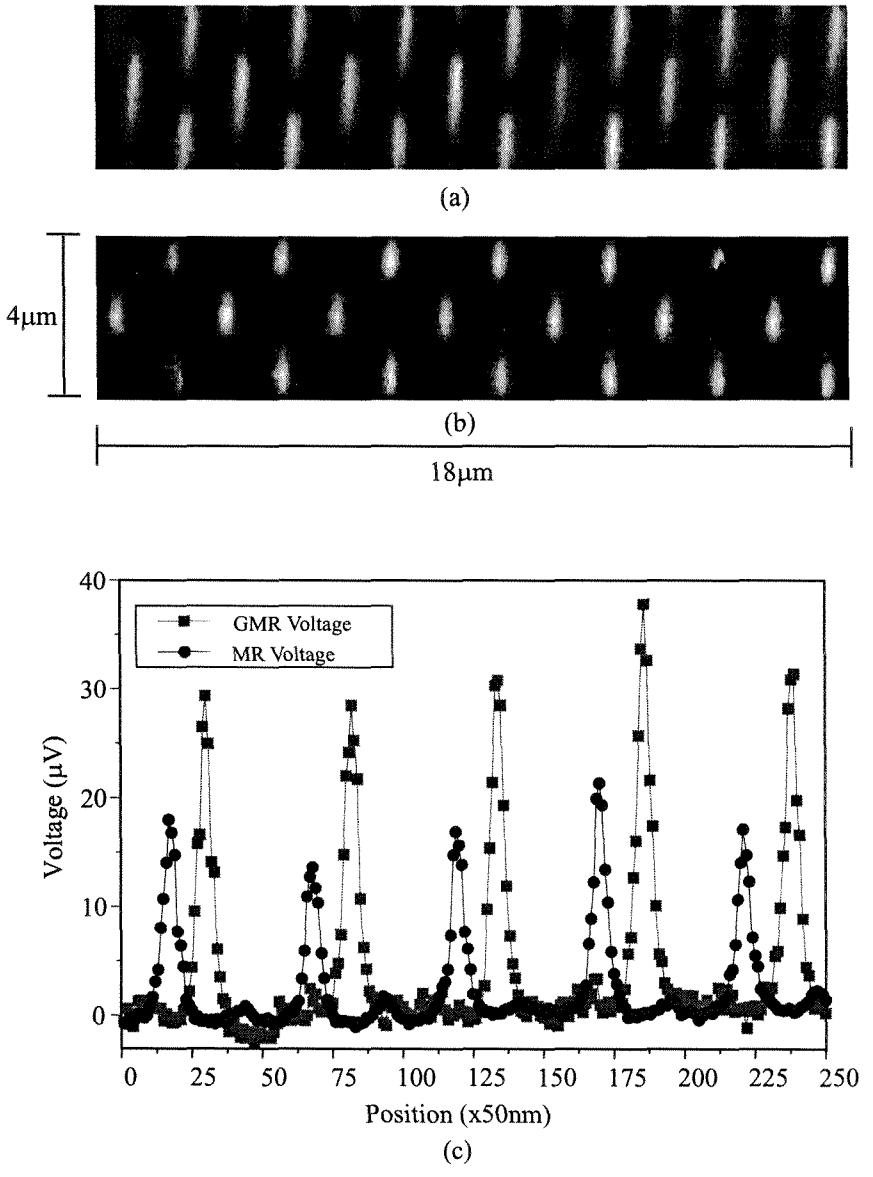

Figure 6.14: Comparison between magnetoresistive (a) and spin-valve (b) imaging of the same patterned media sample. The columns are 170nm in diameter and 2μm apart. The line scans indicating the read-back voltages of the two sensors are shown in (c).

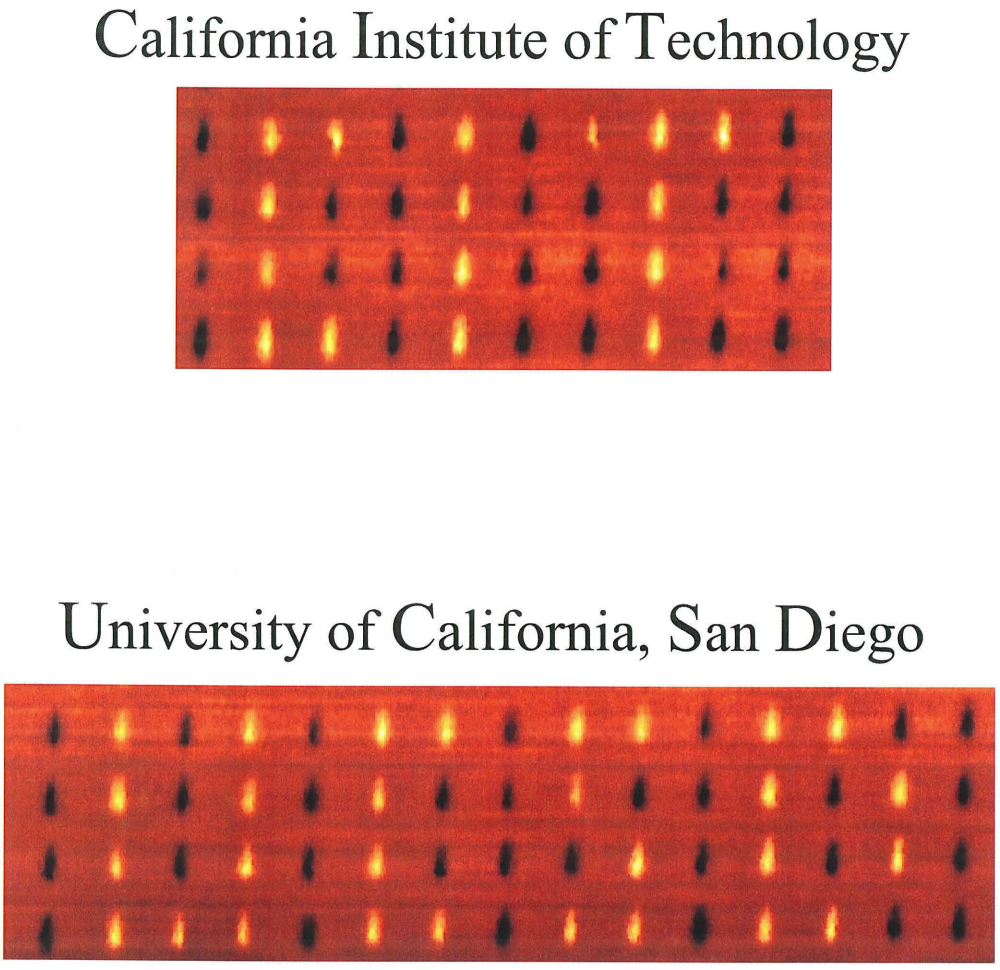

Figure 6.15: SMRM images using a spin-valve sensor of the patterned media sample recorded such that the columns appearing in yellow in the image indicate the initial letters of our academic institutions: "CIT" and "UCSD".

column spacing. This configuration was used for the initial recording demonstrations using current read/write technology. Following this proof-of-concept demonstration at a low bit density, we are now working toward making patterned media with columns that are spaced closer together, and still achieving reliable reading and writing of individual columns using conventional read/write technology. Since the read element (magnetoresistive or spin-valve) is much wider in the cross-track direction than it is in the down-track direction, our recent work focuses on the fabrication and characterization of patterned media in the form of tracks. These structures have the columns separated in the x direction by 1μm due to the width of the recently obtained spin-valve sensors. The columns are initially spaced in the y direction by 0.5μm, which gives an areal density of 1.3Gbits/in.^{2}. The finite width of the spin-valve sensor of $\sim 0.8\mu$m and the $\sim$500nm width of the spatial column response in the down track direction, as evident in Figure 6.14 (c), have been taken into account during the design of the structure configurations.

Figure 6.16 (a) shows an SEM image of an array of Ni columns embedded in an $(Al_{0.9}Ga_{0.1})_2O_3$/GaAs substrate. The columns are 200nm in diameter, and are spaced 0.5μm and 1μm in the down-track and cross-track direction, respectively. Figure 6.16 (b) shows an MFM image of a 4μm$\times 4\mu$m scan of the same set of plated Ni columns in (a). The black and white contrast seen in the MFM image represents the two possible magnetization states, which are parallel or anti-parallel to the long axis of the cylindrical columns.

Our previous results [74] have shown that the spatial extent of the column response in the down-track direction is on the order of 500nm, which should still allow us to resolve each individual column when the down-track separations are 500nm. So again we proceed to the SMRM technique to determine whether we can controllably store data in the individual columns in this 500nm$\times 1\mu$m track-like column arrangement. Figure 6.17 shows two SMRM images demonstrating recording in an array of 200nm diameter columns that are spaced 500nm and 1μm apart in the down-track and cross-track direction, respectively, using an inductive write and spin-valve read sensor. This configuration corresponds to an areal density of 1.3Gbits/in.^{2}. Line

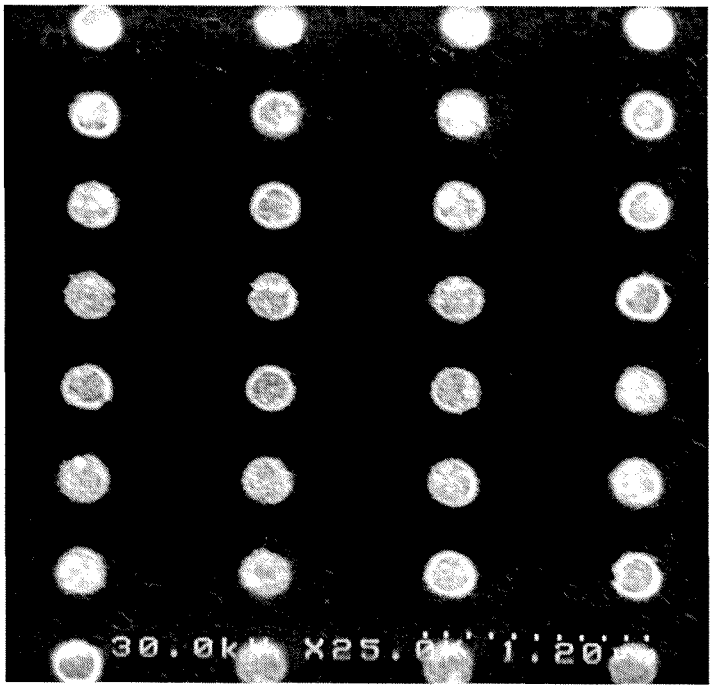

(a)

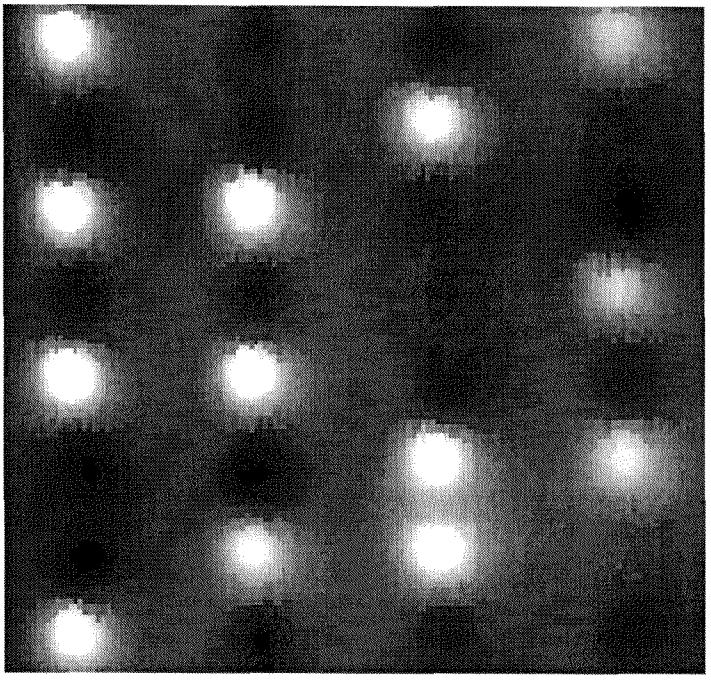

(b)

Figure 6.16: SEM image of an array of Ni columns embedded in an $(Al_{0.9}Ga_{0.1})_2O_3$/GaAs substrate. The columns are 200nm in diameter, and are spaced 0.5μm and 1μm in the down-track and cross-track direction, respectively. (b) An MFM image of a 4μm$\times$4μm scan of the same set of plated Ni columns in (a).

scans representating the GMR readback voltages from the Ni columns are shown on the right side, next to each of the two SMRM images.

In Figure 6.17 (a), all the columns are oriented in an alternating up (white) and down (black) sequence. In this range of column spacing (500nm and below), the interactions from neighboring columns are more significant compared to the larger column separation of 2μm in the previous recording demonstration of 0.1Gbits/in.^{2}. Here, the demagnetizing field of the nearest neighbor provides an additional field in favor of the magnetization orientation of the column of interest. This checkerboard-like arrangement is relatively stable and is a preferred state of the array. In Figure 6.17 (b), the three columns in the center of the image have been oriented in the upward direction (white). This is a less favorable arrangement since each of the columns is subject to an opposing demagnetizing field from its neighbor. The coercivity of each column is high enough in our case to resist the possibility of magnetization reversal due to the opposing fields. From the line scan shown on the right of Figure 6.17 (b), we see that the read-back signal from the center three columns are beginning to merge together, indicating that we are approaching the limit of the spatial resolution of the GMR read sensor used in our experiment. Further reduction in the distance between the columns (250nm and 125nm) will enable us to study the interesting regime of patterned media storage, where the signals from adjacent columns are interfering with the signal from the column directly below the read sensor.

6.3.5 2.6Gbits/in.^{2} recording

Now that we have have demonstrated 1.3Gbits/in.^{2} recording, we continue to decrease the down-track spacing to 0.25μm, while keeping the cross-track spacing at 1μm, in order to allow a systematic study of the recording properties of patterned media samples with increasing down-track densities. This configuration corresponds to an areal density of 2.6 Gbits/in.^{2}. An SEM image of a similar array as in Figure 6.16 (a), except the columns are 120nm in diameter, and have a 0.25μm down-track spacing, is shown in Figure 6.18 (a). An MFM image of an electroplated Ni column array of

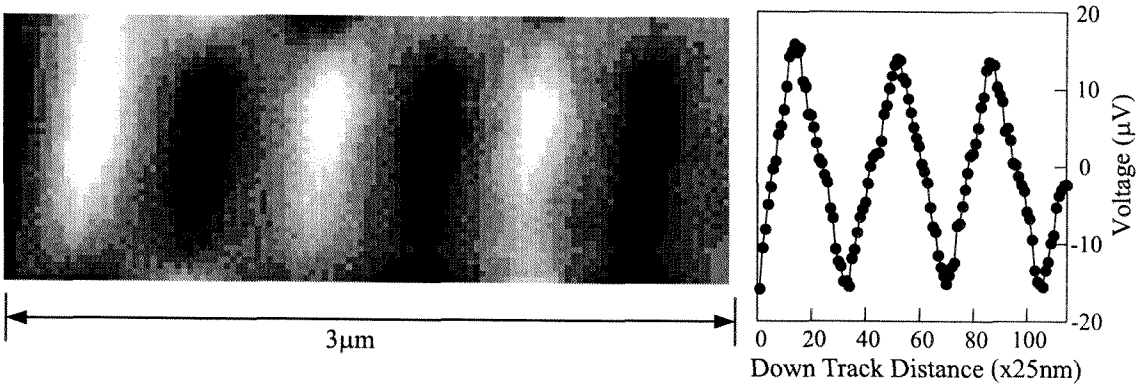

(a)

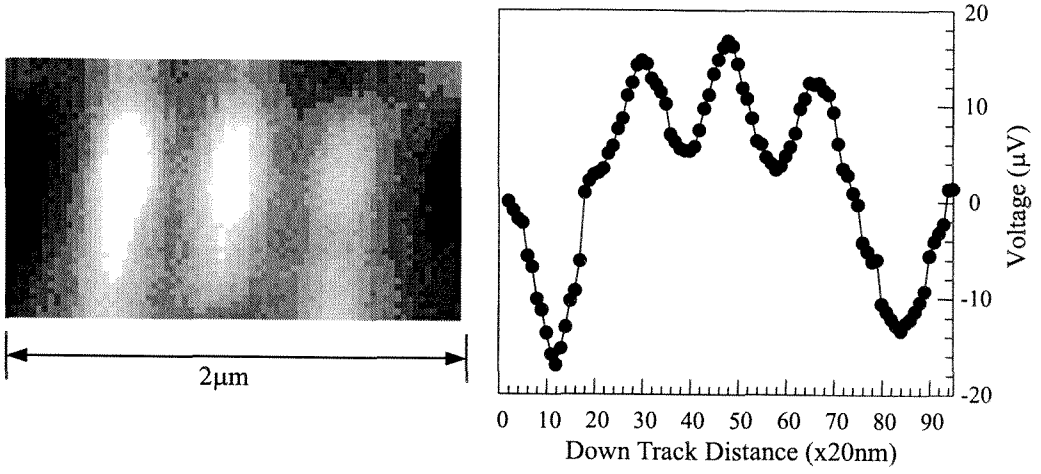

(b)

Figure 6.17: Spin-valve imaging demonstrating 1.3Gbits/in.^{2} recording. The Ni columns are 150nm in diameter, and have a 500nm and 1μm spacing in the down-track and cross-track direction, respectively. Line scans of the read-back voltage are shown on the right side of each image.

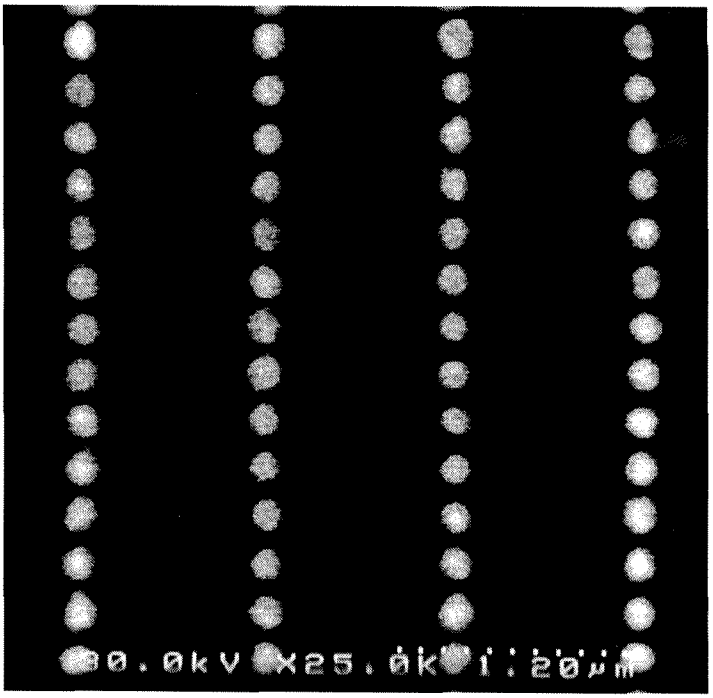

(a)

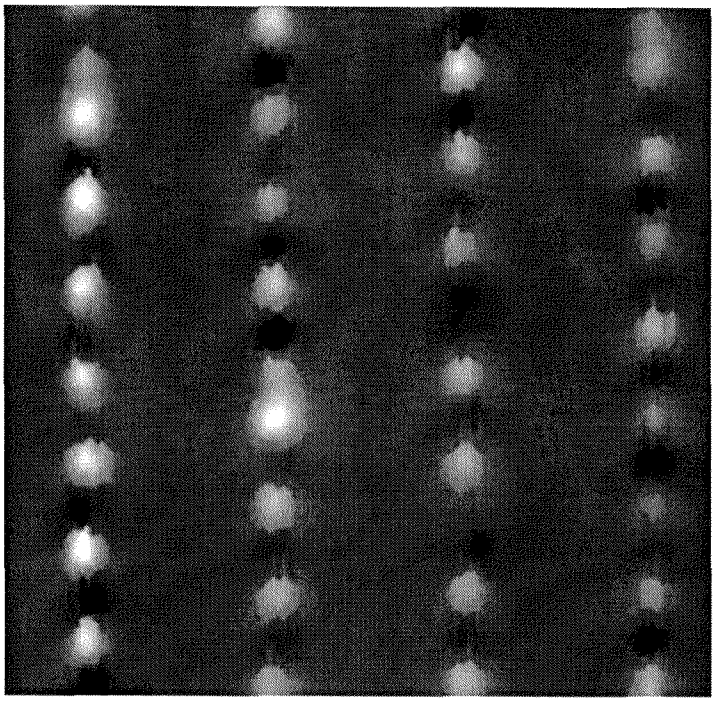

(b)

Figure 6.18: SEM image of an array of Ni columns embedded in an $(Al_{0.9}Ga_{0.1})_2O_3$/GaAs substrate. The columns are 120nm in diameter, and are spaced 0.25μm and 1μm in the down-track and cross-track direction respectively. (b) An MFM image of a 4μm×4μm scan of an electroplated Ni column array of the same configuration as in (a).

the same configuration as in (a) is shown in Figure 6.18 (b).

Figure 6.19 shows a collection of SMRM images that demonstrate single bit per column perpendicular patterned media storage at 2.6Gbits/in.^{2}. The four $3\mu m \times 1.2\mu m$ SMRM gray scale images show the various recorded data track configurations. In Figure 6.19 (a), all the columns are oriented in an alternating up/down (white/black) sequence. In Figure 6.19 (b), the columns are sequenced in a two up/two down fashion. Figure 6.19 (c) shows the pattern where every third column is in the up state, while Figure 6.19 (d) shows ten columns in a row all oriented in the up state, bracketed by the down and then an up column on each side. The line scans which represent the read-back voltages detected by the spin-valve sensor are shown on the right of each image. Note that in Figure 6.19 (d) where all the columns are oriented in the same direction, we can barely resolve the individual neighboring columns with our current read sensor. This indicates an upper areal density limit to our recording demonstration using the current read/write heads.

We emphasize that, while this demonstration is still behind the latest longitudinal thin film media areal density laboratory demonstration, the spacing in the cross-track direction is limited by the width of the read sensor (spin-valve) used in our work, and not by our lithographic method, which is capable of defining structures beyond 65Gbits/in.^{2} [59]. As sensors are developed with narrower widths and read gaps, we will be able to correspondingly reduce the cross-track distance between the columns, along with further reduction of both the column diameters and their spacing in the down-track direction. If a future read sensor width permitted a square lattice with 250nm spacing, our density described here would be 10.4Gbits/in.^{2}.

6.4 Study of the writing configurations

In the SMRM measurement, the Ni columns in our samples are oriented in the desired magnetization direction using the perpendicular component of the fringing field from the inductive write poles. For each magnetization orientation, we have a choice of using either the front or back write pole to arrive at the same outcome. Figure 6.20

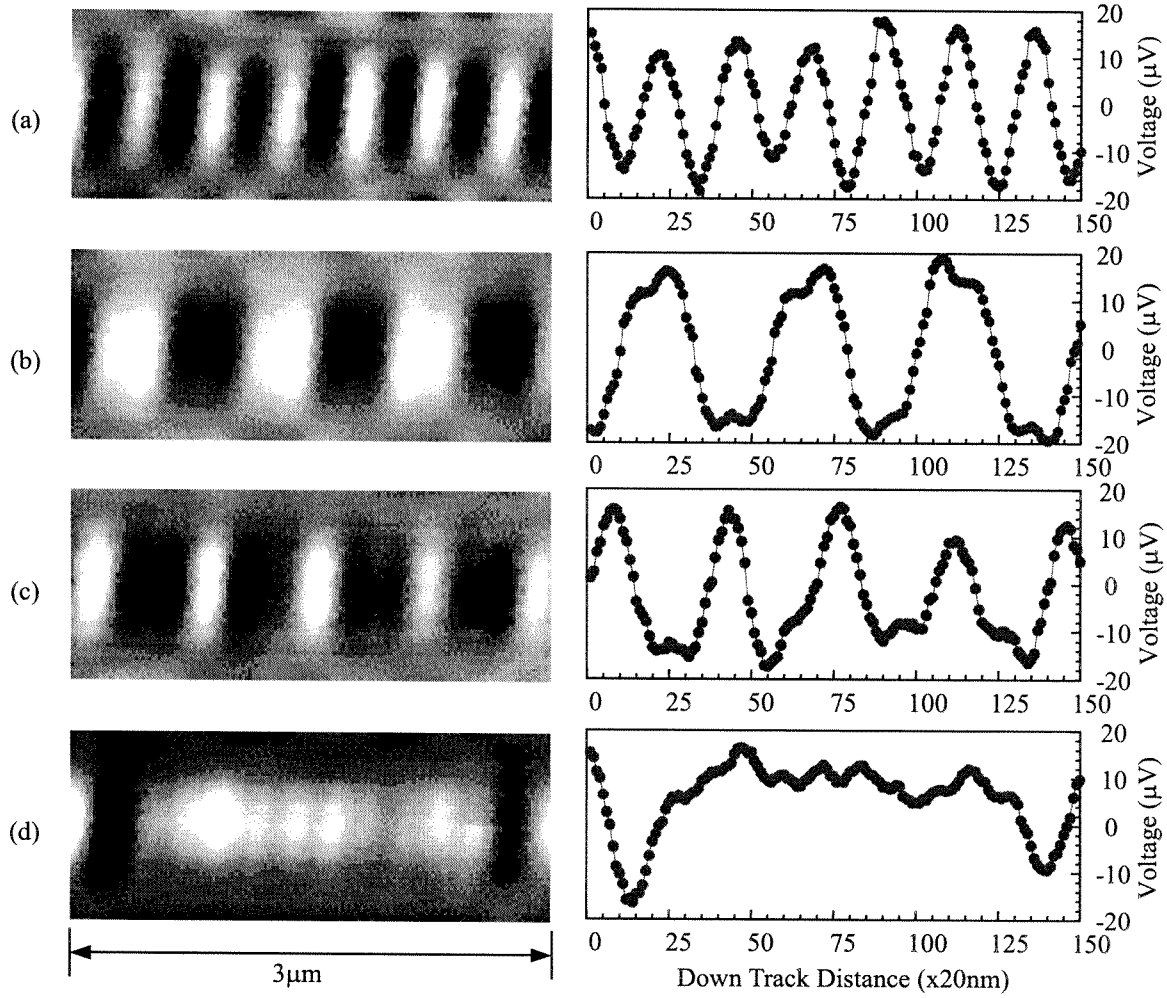

Figure 6.19: Spin-valve imaging demonstrating 2.6Gbits/in.^{2} recording. The Ni columns are 150nm in diameter, and have a 250nm and 1μm spacing in the down-track and cross-track direction, respectively. Line scans of the read-back voltage are shown on the right side of each image.

shows four possible configurations [Figures 6.20 (b), (c), (e), and (f)] in switching the Ni column from an initial state of up [Figure 6.20 (a)] or down [Figure 6.20 (d)] to the opposite magnetization. In each of the cases, the measured MR read-back voltage versus its downtrack position is presented. An illustration of the location of the write poles and MR read element with respect to the Ni column to be switched is also shown above each of the SMRM scans for clarification. In the top three images of Figure 6.20, a Ni column with an initial state in the "down" direction is being switched by the front write pole [as shown in Figure 6.20 (b)] and the back pole [as shown in Figure 6.20 (c)]. The polarity of the current through the write coils changes in the two possible writing configurations just mentioned such that the vertical component of the fringing field from the pole used for writing is in the correct ["up" in cases (b) and (c)] direction.

When the current pulse is applied to the write coils in each case, the MR element also detects a transient (or glitch) from the back pole, which is at a closer distance to the MR sensor than the front pole. The polarity of the transient indicates the magnetization of the back pole at the time the pulse is applied. In addition, the location of the transient with respect to the MR signal from the column being switched provides the actual distance between the read sensor and the pole used for the magnetization reversal of the column of interest. In Figure 6.20 (b), the distance between the downward glitch in red and the column being flipped (indicated by a blue arrow pointing in the upward direction) is 2.5μm, which is the distance between the MR and the front write pole. Whereas in Figure 6.20 (c), the distance between the upward blue glitch and the column being flipped (again indicated by a blue upward arrow) is 1.7μm, which is the distance from the back pole to the MR sensor. The configurations shown in Figures 6.20 (e) and (f) are identical to those in (b) and (c), with the difference that the initial magnetization state of the column is in the upward orientation. Therefore, current in the reverse polarity compared to the cases in (b) and (c) is applied to illustrate magnetization reversal using the front and back pole, shown in Figures 6.20 (e) and (f), respectively. The main purpose of this study is to verify the specific component (perpendicular vs. longitudinal) of the fringing

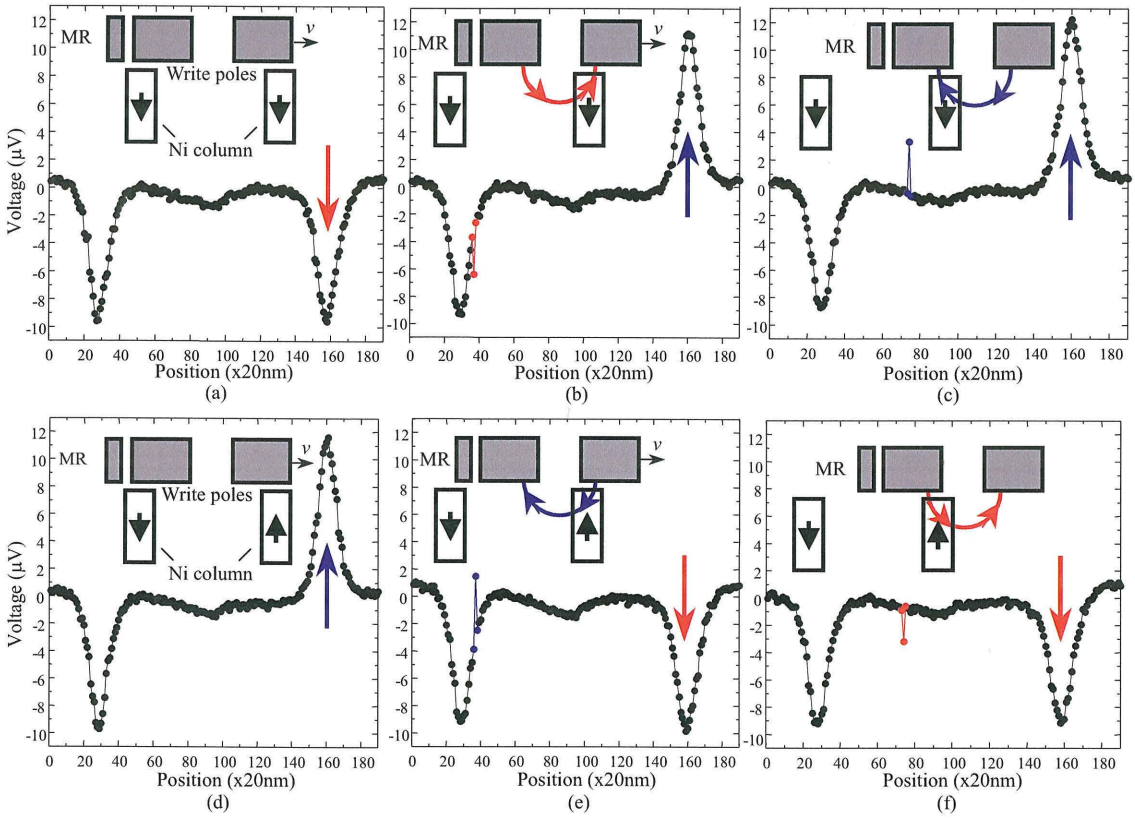

Figure 6.20: A collection of SMRM images illustrating the various writing configurations of our patterned media samples using the front and back poles of the write transducer.

fields from the write pole as well as the actual pole (front or back) that is used when recording data in our samples. Even though the write head is a complicated structure with domains of various orientations, we believe that the demonstration of recording in the individual Ni columns in our patterned media samples is a systematic one.

6.5 Modeling of the writing and reading mechanisms

The magnetic field from an inductive write head is complex due to the complicated head geometry. Head fields can be solved numerically by finite element modeling or boundary element modeling, as well as analytically by conformal mapping, Green functions, or transmission line model [17]. Here we have used a simple, and yet useful, model following Karlqvist's assumptions [82]. The x (longitudinal) and y (perpendicular) components of the Karlqvist head field are given by [17]:

$$\begin{aligned} H_x(x,y) &= -\frac{\partial \phi}{\partial x} = \frac{H_g}{\pi}\tan^{-1}[\frac{gy}{x^2+y^2-(g/2)^2}], \\ H_y(x,y) &= -\frac{\partial \phi}{\partial y} = -\frac{H_g}{2\pi}\ln\frac{(x+g/2)^2+y^2}{(x-g/2)^2+y^2}, \end{aligned} \tag{6.1}$$

where H_g and g are the head field and the write gap width, respectively. At the small gap limit, $g \to 0$, Equation 6.1 becomes:

$$\begin{aligned} H_x(x,y) &= \frac{H_g g}{\pi}\frac{y}{x^2+y^2}, \\ H_y(x,y) &= -\frac{H_g g}{\pi}\frac{x}{x^2+y^2}. \end{aligned} \tag{6.2}$$

The write poles and column arrangement during the SMRM recording procedure is illustrated in Figure 6.21 (a). Once again, the vertical component of the fringing field from the write poles is used to orient the columns in the desired magnetization direction. The perpendicular component of the Karlqvist field as a function of x (displacement along track) for various write currents applied to the head coils is

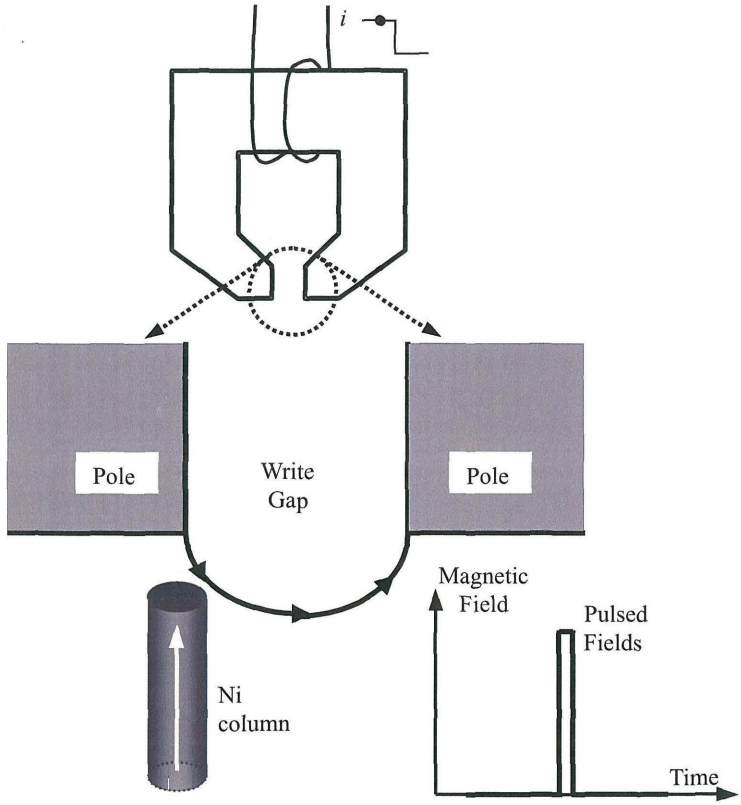

(a)

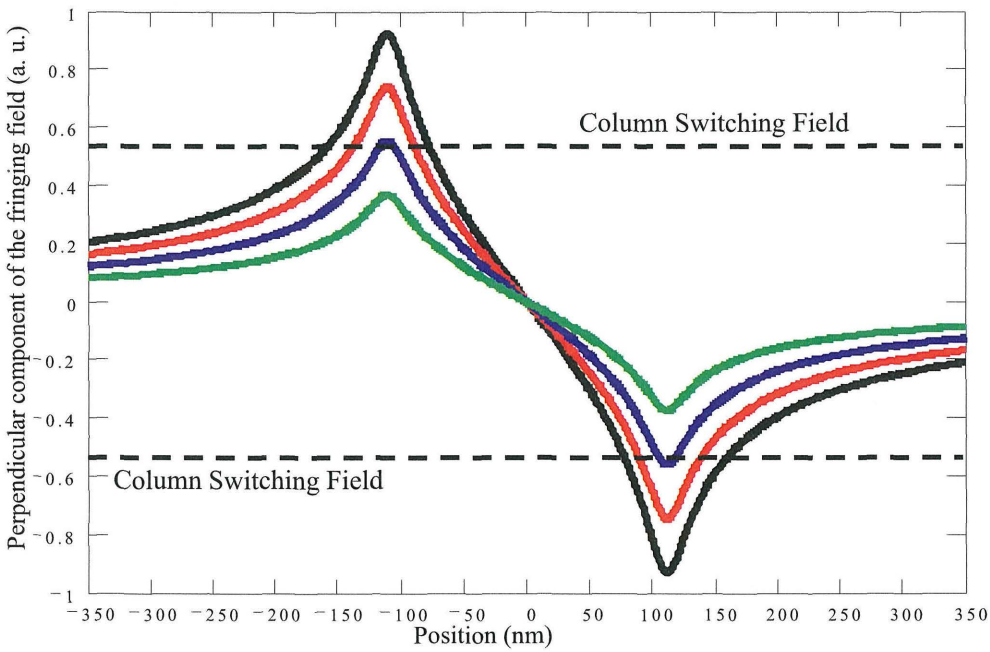

(b)

Figure 6.21: An illustration of the SMRM recording procedure using an inductive write element is shown in (a). Modeling of the Karlqvist perpendicular fields vs. downtrack position, x, for various write currents applied to the head coils is shown in (b).

plotted in Figure 6.21 (b). The spacing between the write poles and the columns is kept constant. The minimum field necessary to switch the magnetization of the Ni column is marked by a dotted line in the plot, one for each polarization of the write current (i.e., positive and negative magnetic field). It can be seen that if the minimum switching field (shown in blue in the plot) is applied, there is only one location (in each current polarization) where the column can be switched successfully. This location is at +125nm (or −125nm for the opposite polarity) with respect to the half width of the write gap. Naturally, if an insufficient field is applied (such as the green curve in the plot), the magnetization of the column will not be reversed. In our experiments, as well as in future recording systems utilizing patterned media, a field larger than the minimum required switching field (e.g., red or black curve in the plot) is used, so that there is a larger region for successful switching, hence more tolerance in the positioning error of the head with respect to the column.

As for simulating the MR spatial response from a single Ni column, we use the Potter approximation [81], assuming a unit potential in the center MR element and grounded shields. The fields detected by the MR element from a Ni column are just two displaced Karlqvist fields ($H_g g = 1$) of opposite signs. We are interested in the potential:

$$\phi(x,y) = \phi^+(x,y) + \phi^-(x,y), \tag{6.3}$$

$$\text{where} \quad \phi^{\pm}(x,y) = \frac{\pm y}{\pi g_1}(u_1^{\pm}\tan^{-1}u_1^{\pm} - 0.5\ln(1+(u_1^{\pm})^2)) - \frac{\pm y}{\pi g_2}(u_2^{\pm}\tan^{-1}u_2^{\pm} - 0.5\ln(1+(u_2^{\pm})^2)),$$

$$u_1^{\pm} = ((g_1/2)\pm(x+(g_2+t)/2))/y,$$

$$u_2^{\pm} = ((g_2/2)\pm(x-(g_2+t)/2))/y.$$

This is for an asymmetric head, where g_1 and g_2 are the right and left gap widths, respectively, and $x = 0$ refers to the position at the center of the gap between the shields. In our calculation, $g_1 = g_2 = g/2$. The read-back voltage signal from a single

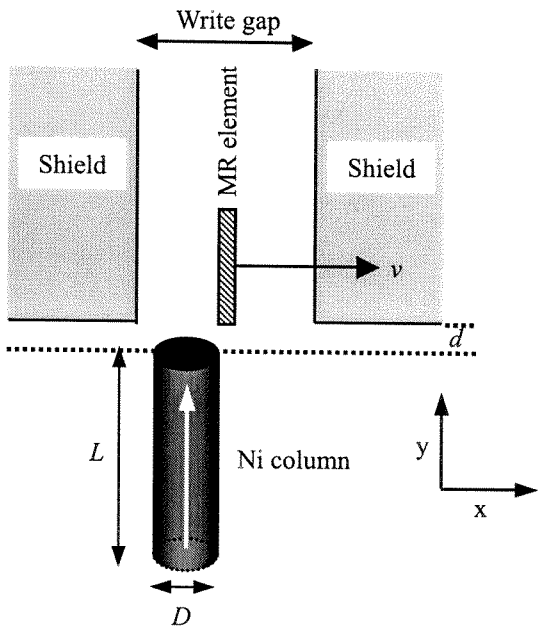

Figure 6.22: An illustration of the SMRM data retrieval procedure using an MR read sensor.

column is given by [83]:

$$V(x) = V_0 \int dx' \int dy' \int dz' \phi(x + x', y', z') \nabla \cdot \vec{M}(x', y', z'). \tag{6.4}$$

Equation 6.4 can be further simplified to:

$$V(x) = V_0 \int_{-r}^{+r} dx' \sqrt{r^2 - x'^2} (\phi(x + x', d) - \phi(x + x', d + L), \tag{6.5}$$

where x is the column down-track position, r is the column radius, d and L are the column diameter and height, respectively. A diagram illustrating the reading configuration using an MR sensor, with the above dimension variables, is shown in Figure 6.22. Using Equation 6.5, we have varied parameters such as the column diameter, height, aspect ratio, and the flying height, and investigated the MR spatial response from a single Ni column. In our modeling, the write gap width, g, is kept constant at 240nm, which is the dimension of the commercial MR sensor used. The flying height, d, is chosen to be 10nm, which should closely resemble the actual

measurement setup, where the recording head is in physical contact with the surface of the medium.

In one of the simulation cases, the aspect ratio is kept constant at 5:1, while the diameter of the column takes up values of 50, 75, 100, 125, and 150nm, which correspond to column heights of 250, 375, 500, 625, and 750nm, respectively. A plot of the expected MR read-back voltage versus down-track position of the MR sensor (assuming the Ni column is at $x = 0$) using the above modeling parameters is shown in Figure 6.24. It is evident from Figure 6.23 that the main difference among the response from various aspect ratio columns is the amplitude of the read-back signal. The signal increases by a factor of $\sim$2.5 when the column diameter changes from 50 to 150nm, with the column aspect ratio kept constant. This is reasonable due to the increase in effective magnetic charge sensed by the MR element from a larger-diameter column. The corresponding width of the spatial response is also narrower for smaller-diameter columns.

Another set of modeling parameters we used to simulate the MR response is to vary the column aspect ratio by keeping a constant column diameter while changing the height simultaneously. We have selected 150nm for the column diameter, and 100, 250, 500, and 750nm for the height, respectively. These values correspond to aspect ratios of 0.67, 1.67, 3.33, and 5 for the four cases. A plot of the MR spatial response versus its down-track position using the above parameters is shown in Figure 6.24. From Figure 6.24, we see that the signal amplitude increases by a factor of about 1.5 as the aspect ratio varies from 0.67 to 5. This change in the signal level is not as significant as in the previous modeling of varying column diameter with constant aspect ratio (Figure 6.23). In the plot of Figure 6.24, however, an interesting deviation in the general shape of the MR response is observed for the two lower aspect ratio cases. For aspect ratios of 0.67 (red curve) and 1.67 (black curve), there is an extra dip in the read-back voltages at each of the shoulders of the response curves. These dips represent voltages of negative polarity, and they indicate that an opposite magnetization direction is present at the edges of the column. In other words, the column is multi-domain. If we are to perform actual SMRM measurements of these columns, we

Modeling parameters:

Write gap width = 240nm
Column diameter = 50nm, 75nm, 100nm, 125nm, 150nm
Column height = 250nm, 375nm, 500nm, 625nm, 750nm
Aspect ratio = 5
Flying height = 10nm

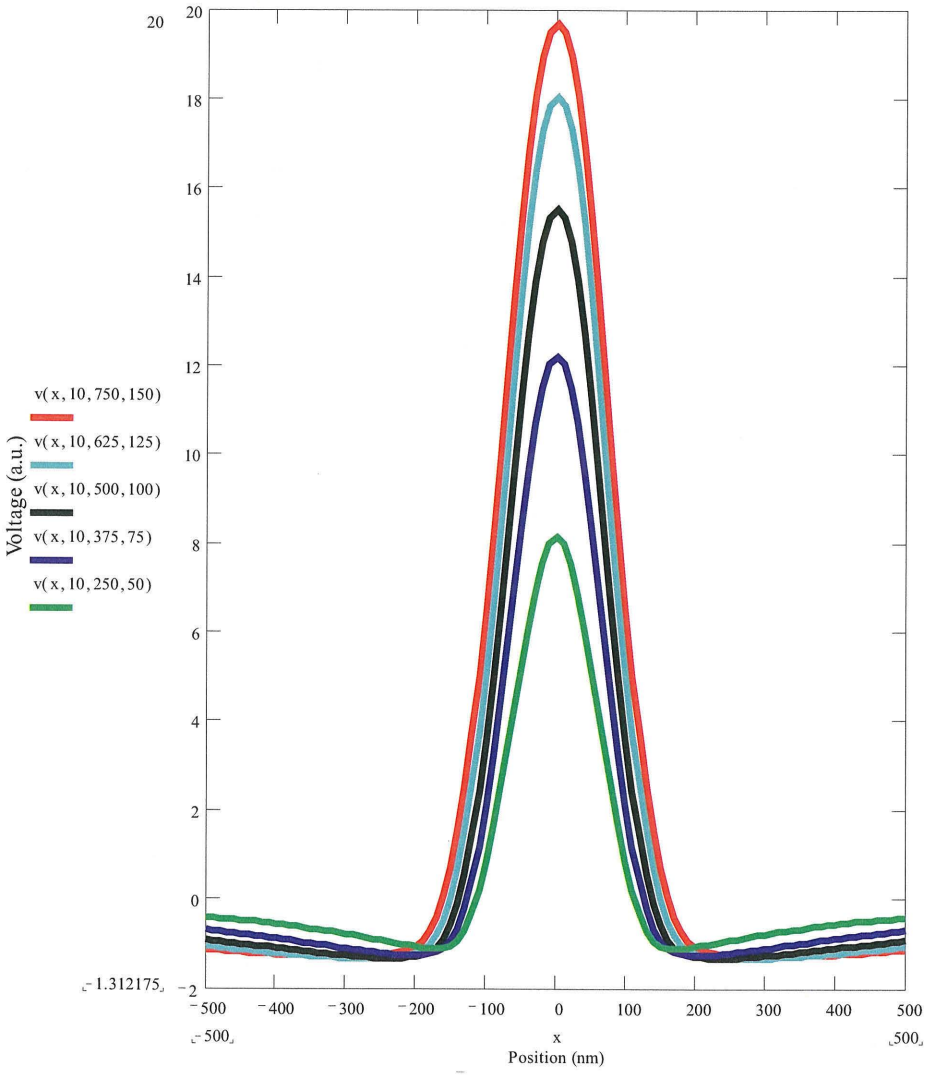

Figure 6.23: A plot of MR read-back voltage from a single Ni column vs. down-track position of the MR sensor. The column aspect ratio is kept constant at 5, while the column diameter has values of 50, 75, 100, 125, and 150nm.

Modeling parameters:
Write gap width = 240nm
Column diameter = 150nm
Column height = 100nm, 250nm, 500nm, 750nm
Aspect ratio = 0.67, 1.67, 3.33, 5
Flying height = 10nm

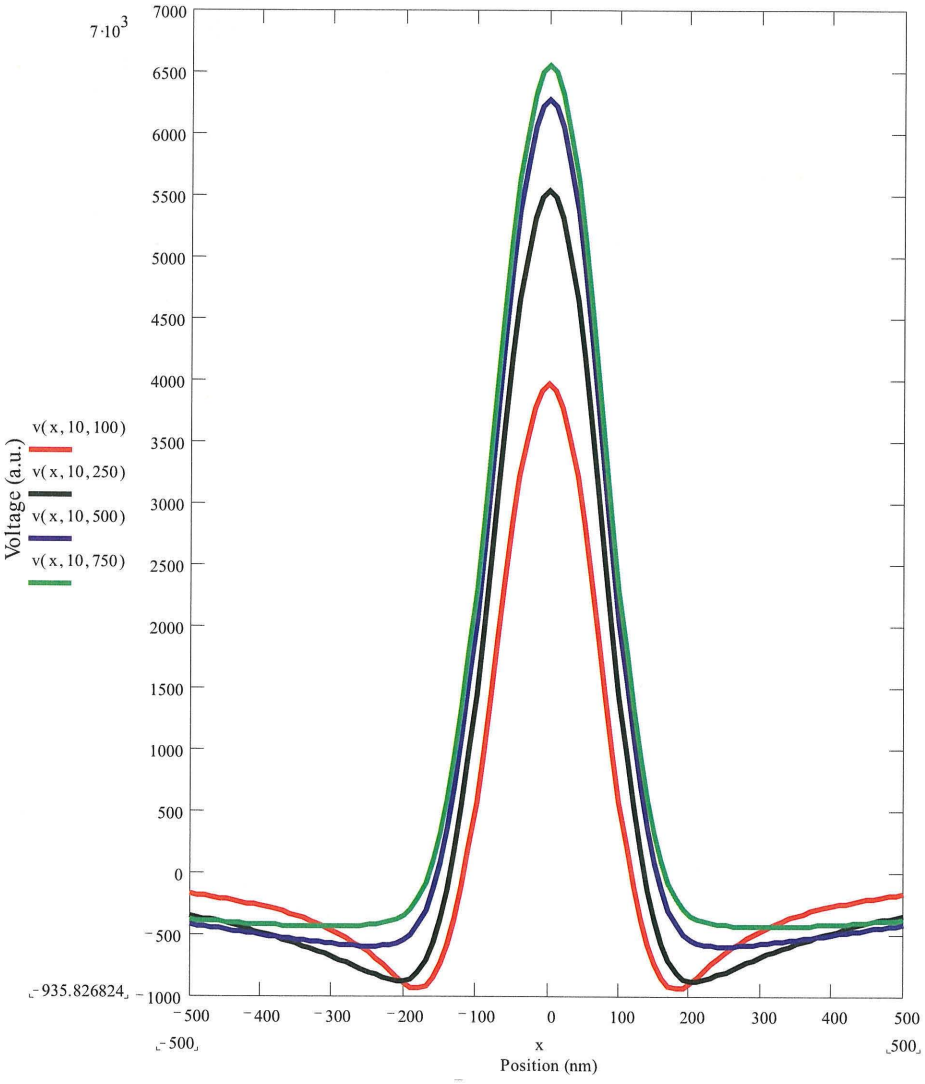

Figure 6.24: A plot of MR readback voltage from a single Ni column vs. down-track position of the MR sensor. The column diameter is kept at 150nm, while the column height has values of 100, 250, 500, and 750nm, corresponding to column aspect ratios of 0.67, 1.67, 3.33, and 5.

would expect to see a "dibit" signal (both black and white contrast or magnetization present within the same particle) in the columns with 0.67 and 1.67 aspect ratios. In our SMRM characterization, we have not measured this type of reverse polarity (or dips) in our read-back voltage signal. We also have not observed any "dibit" SMRM image consisting of both black and white contrast in any single column. This confirms that the Ni columns in our patterned media samples are indeed single-domain, and their aspect ratio is sufficient to support that mode of domain structure.

6.6 Comparison of modeling results and SMRM data

One of the assumptions included in the modeling of the MR spatial response is the magnetization of the column being represented by two sheet charges of opposite polarity at both ends of the column. This is illustrated in Figure 6.25 (a) where two sheet charges, one positive and the other negative, are placed at the top and bottom of the Ni column, respectively. The location of the MR read element, along with the two adjacent shields, with respect to the top of the Ni column is also indicated in the figure. A diameter of 170nm and height of 750nm, with an aspect ratio of 4.41, are used for the column dimensions in the modeling. The write gap width is 220nm while the flying height is 10nm. These parameters simulate the actual experimental setup. A comparison of the modeling result using the sheet charge assumption in Figure 6.25 (a) and the MR read-back voltage from one of the Ni columns in our patterned media samples is shown in Figure 6.25 (b). The peak amplitude of the SMRM data (shown as filled squares) is 20μV, and the modeling curve (shown as a solid line) fits well within the neighborhood of 100nm on both sides of the peak. Around the shoulders of the peak, however, there is a large difference between the modeling result and the actual data.

We suspect that the large discrepancy between the modeling and the data in Figure 6.25 (b) is due to deviation of the magnetization from the preferred state,

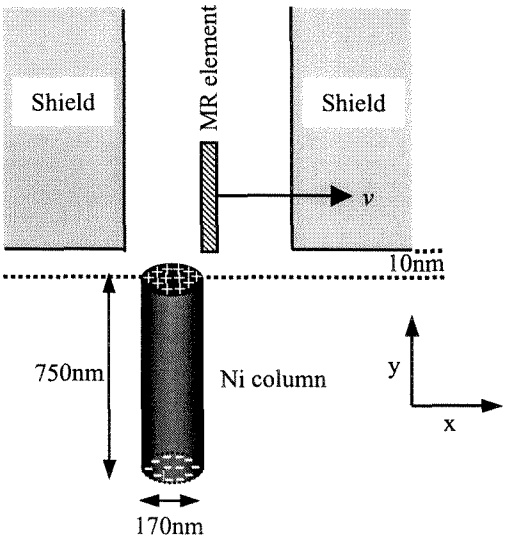

(a)

Modeling parameters:
Write gap width = 220nm
Column diameter = 170nm
Column height = 750nm
Aspect ratio = 4.41
Flying height = 10nm

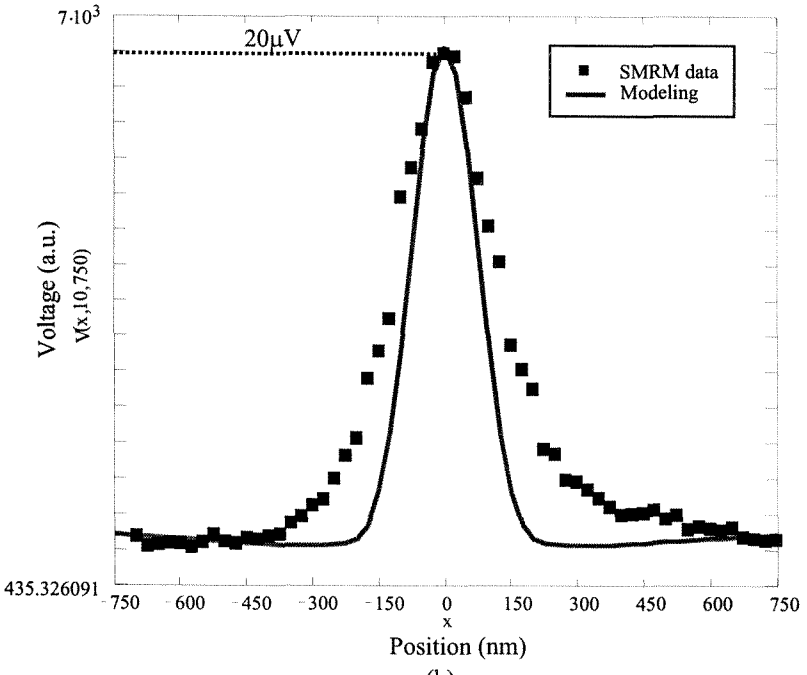

(b)

Figure 6.25: An illustration of the MR read sensor above a Ni column, with a positive and negative sheet charge located at the top and bottom of the column, respectively, is shown in (a). A superposition of the modeling result using the sheet charge assumption in (a) and the SMRM data is shown in (b).

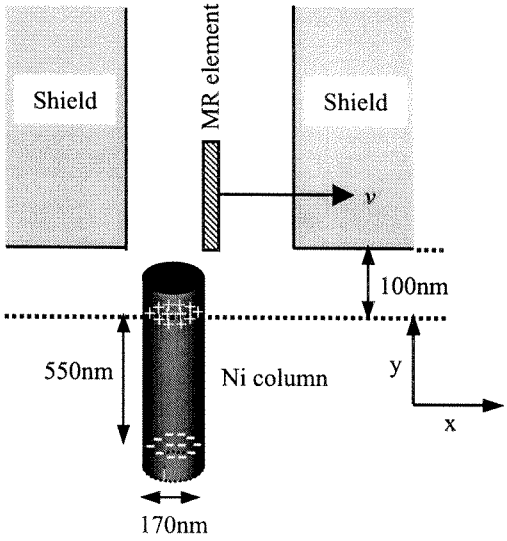

(a)

Modeling parameters:
Write gap width = 220nm
Column diameter = 170nm
Column height = 550nm
Aspect ratio = 3.24
Flying height = 100nm

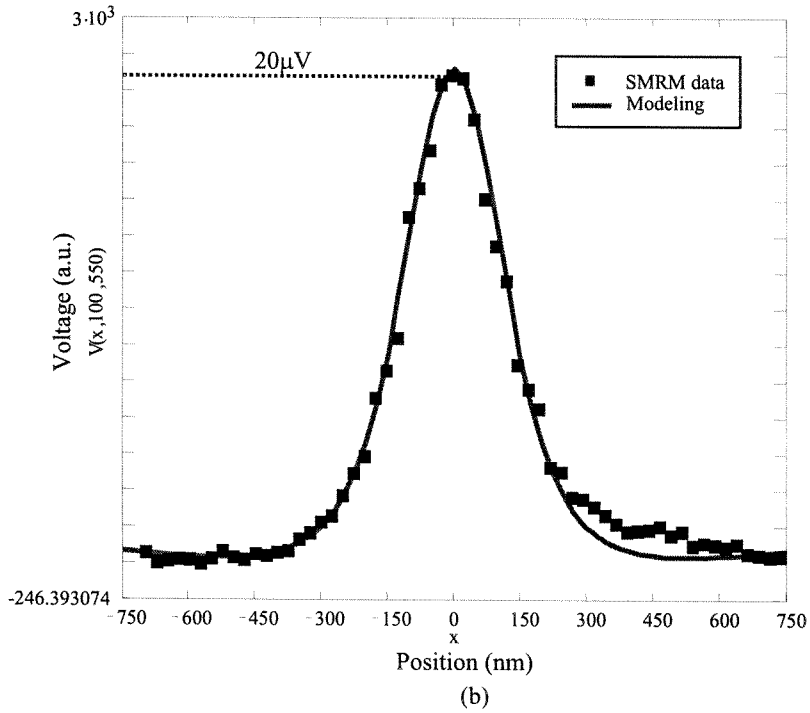

(b)

Figure 6.26: An illustration of the MR read sensor above a Ni column, with a positive and negative sheet charge located 100nm from the top and bottom of the column, respectively, is shown in (a). A superposition of the modeling result using the sheet charge assumption in (a) and the SMRM data is shown in (b).

in which all the spins within the column are uniformly aligned throughout the entire length of the column, once the external field is removed. This possibility is illustrated in Figure 6.8 (b), in a previous section of this chapter. To account for this deviation, we shift the two sheet charges away from both ends by 100nm towards the center of the column, as illustrated in Figure 6.26 (a). Effectively, the height of the column is 550nm instead of 750nm. The diameter of the column remains to be 170nm, which corresponds to an aspect ratio of 3.24. The "flying height" between the MR sensor and the column is now 100nm, as a result of the lowering of the top positive sheet charge. The write gap width is 220nm, as in the previous modeling case. A comparison between the modeling result using the modified sheet charge assumption in Figure 6.26 (a) and the MR response from a Ni column is shown in Figure 6.26 (b). The same set of SMRM data, with a peak voltage of 20μV, is used for both comparisons. As seen in Figure 6.26 (b), the modeling result fits reasonably well with the SMRM data, suggesting the validity of our modified sheet charge assumption. We expect that as the column diameter becomes smaller, provided that the aspect ratio of the column is large enough to support single-domain behavior, the deviation of the magnetization direction within the column will become less significant.

Chapter 7 High resolution patterning and storage limits of perpendicular patterned media

One of the determining factors for ultrahigh areal storage densities is the capability of the lithography technique for high resolution patterning. We have continued to use electron beam lithography to define our structures. In this chapter, current work on higher density structures fabricated in the $(AlGa)_2O_3$/GaAs material system, in the form of both tracks (5.2Gbits/in.^{2}) and square arrays (65Gbits/in.^{2}), is described. Even higher density structures have been fabricated as well, in the form of square arrays, on a Si substrate using a very thin layer of PMMA. Important parameters in the process of high resolution e-beam patterning are briefly discussed. The chapter ends with the anticipated limits of perpendicular patterned media from the patterning as well as the perspectives of magnetics.

7.1 Higher density structures

7.1.1 Electron beam lithography conditions

For defining high resolution structures, each of the steps in the electron beam lithography procedure is very critical, in addition to the subsequent etching steps. The metal layers and substrate underneath the resist, composition and thickness of the resist material, prebake condition of the resist, background pressure of the vacuum chamber for e-beam writing, beam voltages and currents, exposure doses, resist developer composition and development time, etc., are some of the process parameters that need to be taken into account and carefully monitored to achieve the minimum feature size possible with the available lithography system. A few of the e-beam

lithography parameters will be briefly discussed. Among all the above conditions, the one that is often overlooked is the prebake (or softbake) process prior to exposure. This process will be emphasized here, since without a resist film that is precise and uniform across the regions where the patterns will be defined on the wafer, it will be difficult to obtain high resolution patterning that is reproducible in the subsequent exposure, development, and etching procedures.

Prebake is the process of converting a liquid-cast resist into a solid film before exposure and development of the resist. This step involves the physical removal of the casting solvent without the degradation of the resist components. By removing the casting solvent, a solid state is formed so that the exposed and unexposed regions in the resist do not mix and degrade the resolution of the desired features [84]. The prebake process not only allows solvent removal before exposure, but it also promotes stress relief, closure of pinholes, and film planarization as a result of polymer flow. Chlorobenzene is a common casting solvent used in PMMA. It has a boiling point of 126°C, which is above the glass transition temperature, $T_g = 105$°C, and below the decomposition temperature, $T_d = 200$°C, of PMMA. Baking PMMA above its T_g will be sufficient to drive all the solvents out of the resist.

A common prebake temperature for PMMA is 150–160°C. Even though all the solvents should be removed from PMMA in a matter of seconds when baking it at 150–160°C, a longer baking time, e.g., 30mins or more, is recommended to allow enough time for polymer relaxation and flow to constrict any holes in the film. For our structures, the prebake process is performed on a hot plate, and the target temperature is 150°C. The initial temperature of the hot plate is at 25°C, and a ramping rate of 480°C/h is used. The baking time once the temperature reaches its target is 30min to 1-1/2h, depending on the thickness of the resist used. The coating and prebaking of PMMA on the substrate is always performed immediately before e-beam exposure to provide consistency in the process.

Another parameter of importance for high resolution patterning is the condition of the vacuum system in which e-beam lithography is performed. A good mechanical alignment of the electron gun is critical for defining high resolution structures. In

addition, focusing and stigmatism of the electron beam should be adjusted and optimized electronically during beam-writing to achieve the minimum beam spot size on the sample. The pressure of the vacuum chamber needs to be monitored carefully before and during the lithography procedure as well. Lower pressure results in longer mean free paths for the accelerated electrons before reaching the PMMA layer on the substrate. Longer paths of the electrons before collision minimize the lateral spreading of the exposed region on the sample. A pressure of 1×10^{-6}Pa or better is preferable in our e-beam lithography system for high resolution work.

Other factors such as the thickness and composition of the PMMA, beam voltages and currents, exposure doses, developer composition and development time, etc., are dependent upon the sizes of the features to be defined. As a common practice, thinner PMMA and lower beam voltages and currents are used when high resolution features are desired. This is to minimize the proximity effects, which will be explained in more detail later in this chapter, encountered in e-beam lithography. In general, each of the above mentioned parameters has its own importance and effects on defining minute features using electron beam lithography, and should be optimized in such a way that high resolution structures can be reproducibly obtained.

7.1.2 5.2Gbits/in.^{2} and beyond

In addition to the magnetic characterization of the structures shown in the previous chapters, we have also fabricated higher density structures in the form of tracks for further data storage demonstration purposes. These tracks have a reduced down-track spacing of 0.125μm while the cross-track spacing of 1μm is maintained, which corresponds to an areal density of 5.2Gbits/in.^{2}. An SEM image of an array of etched holes of 35nm diameter, spaced 0.125μm and 1μm apart in the y and x direction respectively, in an $(Al_{0.9}Ga_{0.1})_2O_3$/GaAs substrate is shown in Figure 7.1.

From the recording demonstration of the 2.6Gbits/in.^{2} array shown in Figure 6.19, it can be seen that we are approaching the spatial resolution limit of the current read/write heads obtained from our industry sponsors. At even higher densities, the

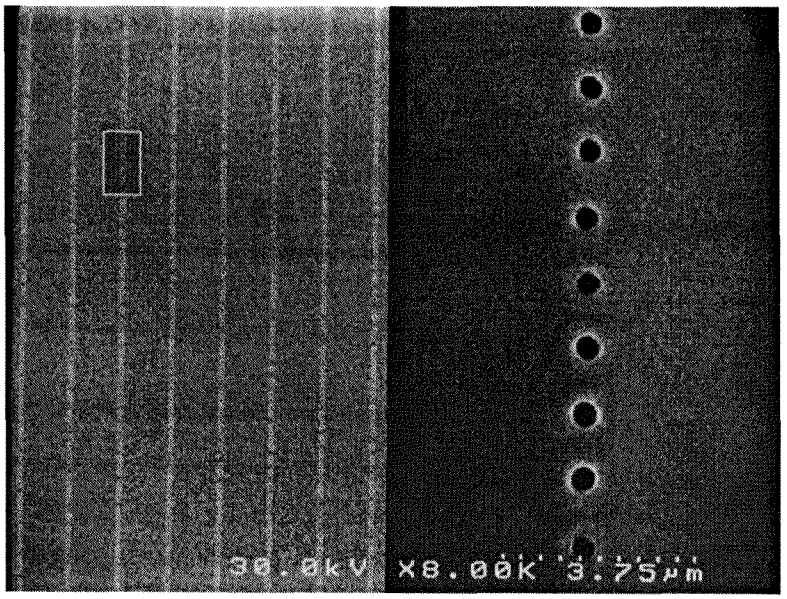

Figure 7.1: SEM image of an array of etched holes of 35nm diameter, spaced 0.125μm and 1 μm apart in the y and x direction, respectively (left). A 10$\times$ enlargement of eight of the holes is shown on the right.

read-back voltages from the individual columns may overlap with the neighboring ones, resulting in difficulties in resolving the signal. For columns with magnetization in an alternating up and down sequence, we may have slightly more tolerances as long as the signals do not overlap so much that they completely cancel one another. In the case of a slight overlap, we may only be able to measure the partial strength and linewidth of the response from each column resulting from signal cancellation, but we should still be able to correctly detect the magnetization direction of a single column in the track. As mentioned before, this alternating sequence is the preferable arrangement for closely packed magnetic columns. Thus the ability to record in such an arrangement cannot be extended to represent the general case for recording in that particular packing density. Besides, the medium must also be able to store low frequency signals (e.g., several neighboring bits in the same orientation) in addition to the high frequency ones (e.g., alternating up and down sequence). So the ultimate test for recording capability in a high density medium is to have all the columns oriented in the same direction, and determine whether each magnetic element is stable under the influence of the demagnetizing and other nonuniform external fields encountered.

In the magnetic recording industry today, efforts are invested in the development of more sensitive and higher resolution read/write heads. Before a revolutionary solution is demonstrated, researchers will continue to scale down the dimensions of the write head by physically trimming it using focused ion beam etching. As for the MR or spin-valve read elements, more careful tailoring methods still need to be investigated. The areal density of the medium in which we can perform recording would be greatly enhanced when narrower read sensors become available to us, in which case the tracks can be spaced closer than 0.25μm and 1μm in the down-track and cross-track direction, respectively.

Besides the track-like configurations, we are concurrently pursuing denser Ni columns in the form of a square array. The goal is to push our lithography techniques to define higher density structures for future use in patterned media, even though recording demonstration in these higher density structures is extremely difficult with our current read/write heads. Using electron beam lithography, we have patterned large arrays of holes of 18nm diameter and 100nm spacing (65Gbits/in.^{2}) into a 450nm-thick PMMA layer, which again serves as both the e-beam resist and an ion etch mask. We have used Cl_2 assisted ion beam etching to transfer the hole patterns into the $Al_{0.9}Ga_{0.1}As$ layer, which is converted into a robust $(Al_{0.9}Ga_{0.1})_2O_3$ mask during wet thermal oxidation. Figure 7.2 (a) shows an SEM image of a 100×100 array of etched holes of 18nm diameter and 100nm spacing in an $Al_{0.9}Ga_{0.1}As/GaAs$ substrate. A close-up view of the array is shown in Figure 7.2 (b).

One difficulty with the smaller diameter holes is the slower etching rate compared with the bigger diameter holes. If the first CAIBE stops in the $Al_{0.9}Ga_{0.1}As$ layer instead of the GaAs substrate, the bottom of the hole patterns will be converted to $(Al_{0.9}Ga_{0.1})_2O_3$ after oxidation. When this happens, any further transfer of the hole patterns into the GaAs substrate will be very difficult, and in some cases, impossible without the complete degradation of the $(Al_{0.9}Ga_{0.1})_2O_3$ masking layer. One solution will be to use thicker PMMA masking layer, provided that the high resolution of the e-beam lithography is preserved. $Cr/Au/SiO_2$ masking layers can also be used in conjunction with a thin layer of PMMA [67]. A thinner AlGaAs masking layer may

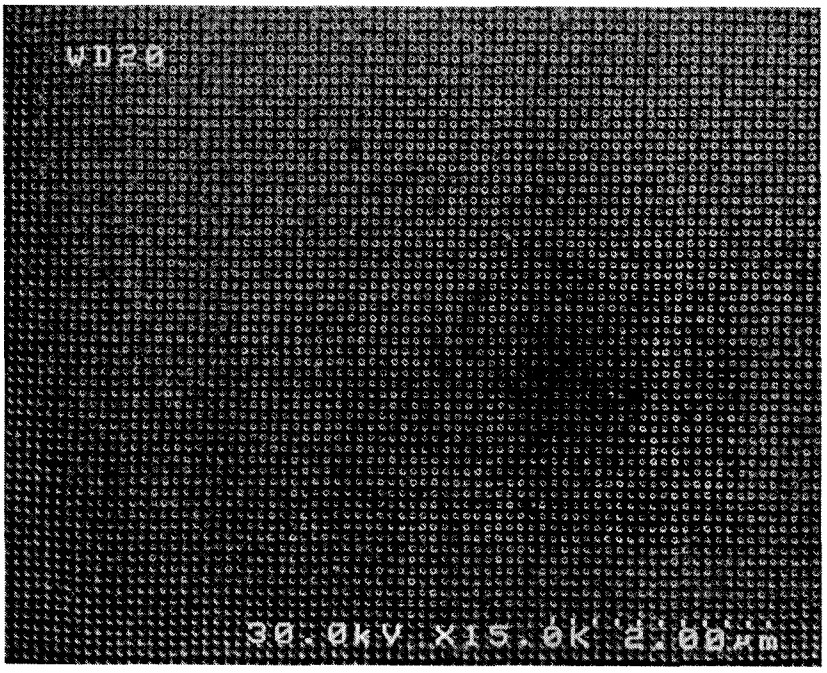

(a)

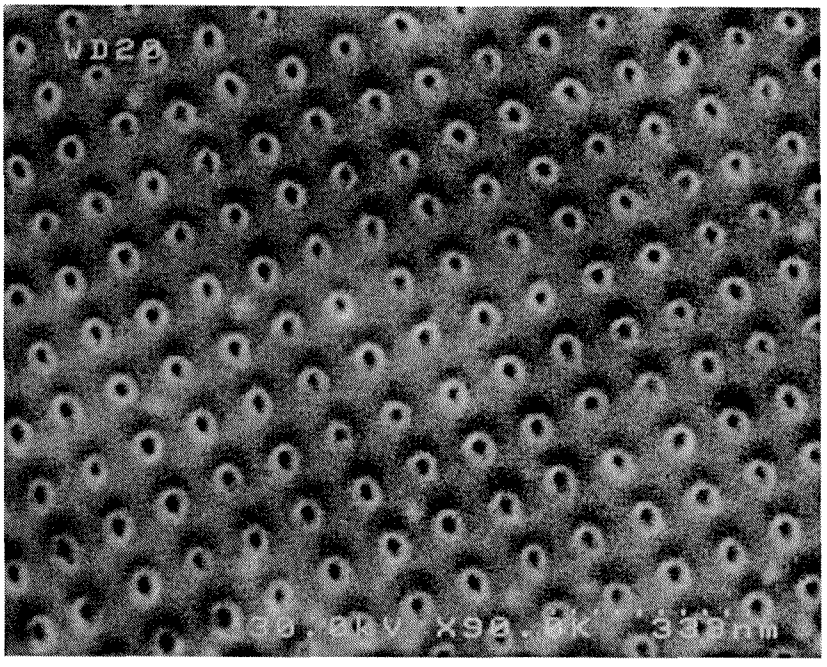

(b)

Figure 7.2: (a) SEM image of a 100×100 array of etched holes of 18nm diameter and 100nm spacing in an $(Al_{0.9}Ga_{0.1})_2O_3$/GaAs substrate. (b) A close-up view of the array in (a).

be sufficient as well, since smaller diameter holes will require shallower etch depths for the same aspect ratio.

7.1.3 100Gbits/in.^{2} and beyond

For areal densities of 100Gbits/in.^{2} and beyond, the parameters for e-beam lithography described earlier play an even more significant role in determining where the limit of the lithography procedure lies. To explore the limits of our e-beam lithography system, we have defined arrays of holes in a thin (40–50nm) PMMA layer coated on top of 70Å of sputtered AuPd on a Si substrate. Using the prebake procedure described in a previous section, the PMMA is baked on a 150°C hot plate for 30min immediately before the exposure. A 30kV beam voltage is used in most cases, and the smallest objective aperture and highest condenser lens current in our scanning electron microscope is chosen to obtain the lowest beam current setting (~3–4pA). Each of the holes in the arrays is a single beam exposure, and the dose is optimized so as to achieve the smallest feature size possible. The focus and stigmatism of the beam is adjusted electronically to get the minimum spot size for maximum resolution. A magnification of 5000× is used, which gives a field of view of 20μm×20μm. After exposure, the sample is developed immediately in isopropyl alcohol for 10s, and dried thoroughly in dry N_2.

Following e-beam exposure and development, the dot array patterns in the PMMA are transferred into the underlying AuPd layer using Ar^+ ion milling. Since the AuPd is very thin, a milling time of 0.5min is sufficient using a beam current and voltage of 10mA and 1000V, respectively. The patterns in the AuPd layer are then examined in a scanning electron microscope, where the lateral dimensions of the e-beam defined patterns are determined. An SEM image of 14 arrays of holes of various diameter and spacing is shown in Figure 7.3 (a). The densest array in both the top and bottom row in the image has hole diameter and spacing of 20nm and 80nm, respectively. The SEM image shown in Figure 7.3 (b) is an enlargement of an array of holes of 17nm diameter and 80nm spacing. There is still a thin layer of PMMA remained after Ar^+

20nm 40nm 60nm 80nm 100nm 150nm 200nm

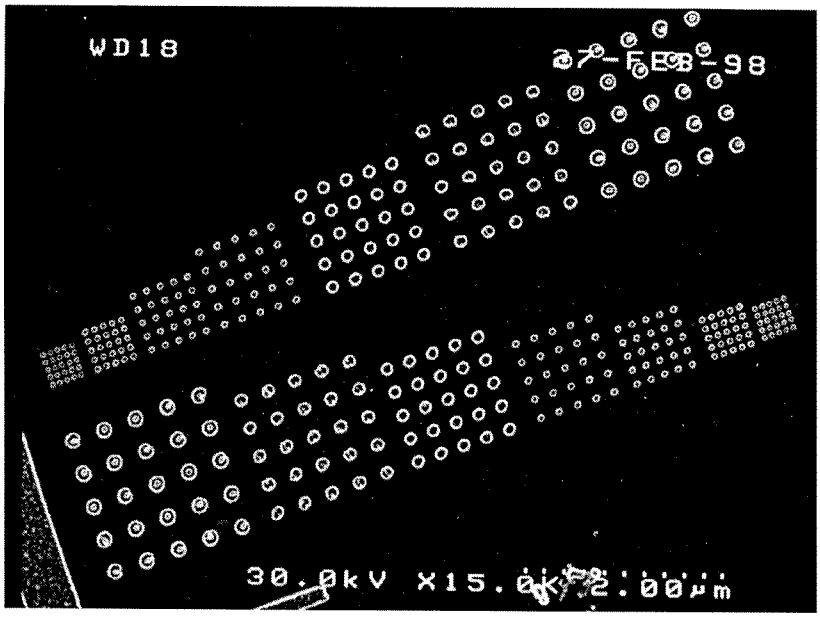

(a)

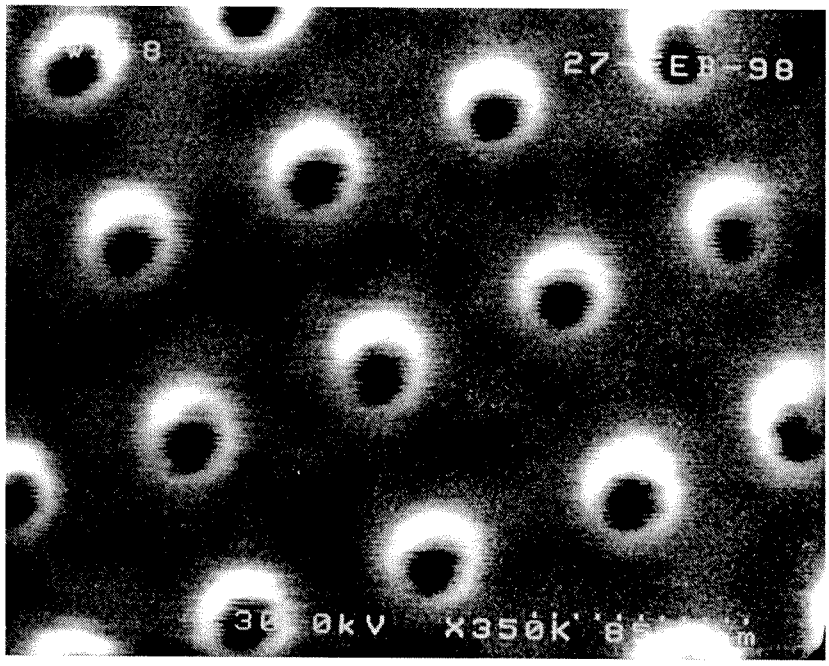

(b)

Figure 7.3: An SEM image of several arrays of holes of various diameter and spacing etched in AuPd on a Si substrate is shown in (a). An enlarged view of an array of holes with 17nm diameter and 80nm spacing is shown in (b).

ion milling, which results in charging during the slow scanning of the e-beam across the array. This charging of the PMMA appears as white fuzzy regions around each hole in the array. If all the holes in the 80nm-period array in Figure 7.3 (b) are filled with magnetic material, this configuration will then correspond to an areal storage density of 100Gbits/in.^{2}.

Hole arrays with a periodicity as small as 45nm have also been fabricated using the procedures described above. The SEM images in Figure 7.4 show several hole arrays of various diameters and center-to-center spacings, that have been etched in AuPd on a Si substrate. The hole array on the left portion of Figure 7.4 (a) has diameter and periodicity of 20nm and 50nm, respectively, corresponding to a packing density of ~250Gbits/in.^{2}. The arrays in Figure 7.4 (b) have diameters of 20nm, 35nm, and 40nm, and spacings of 45nm, 80nm, and 115nm. The 45nm-spacing array is the densest structure that I have fabricated using our electron-beam lithography system, and it represents an areal density of ~350Gbits/in.^{2}. For densities beyond 350Gbits/in.^{2}, proximity correction algorithms during the e-beam writing process will become essential. Note that as the periodicity of the holes drops below 50nm and becomes comparable to the diameter, the holes along the four edges of the square array may have slightly different sizes than the ones toward the center of the array. This is expected since the outer-most row or column of the array has fewer immediate neighbors than the center part of the array, resulting in a lower exposure dose due to less backscattered electrons from nearby neighbors during the e-beam writing process. One remedy will be to increase the exposure time for the outer-most row or column to compensate for the lower dose in those regions.

7.2 Anticipated storage limits of perpendicular patterned media

Perpendicular patterned media are not likely to be the final solution to solve the superparamagnetic problem. At some point, the areal density will be limited by

20nm diameter
50nm c-c spacing

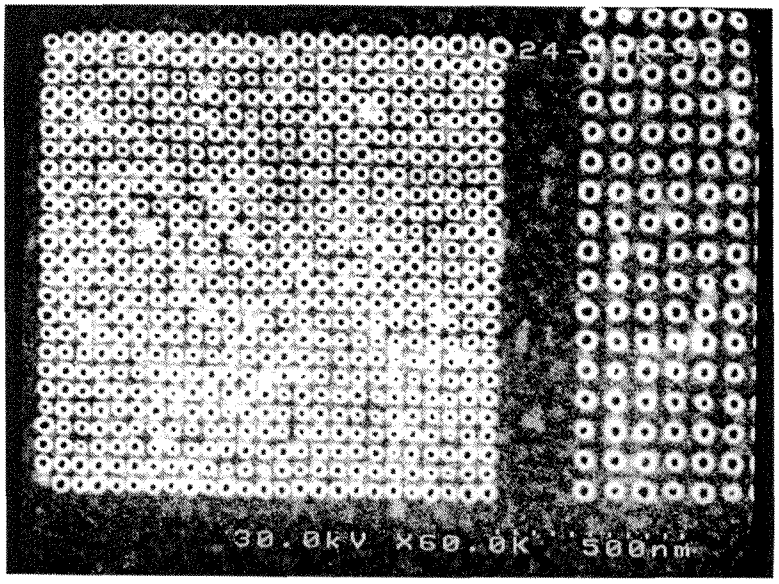

(a)

20nm 35nm 40nm diameter
45nm 80nm 115nm c-c spacing

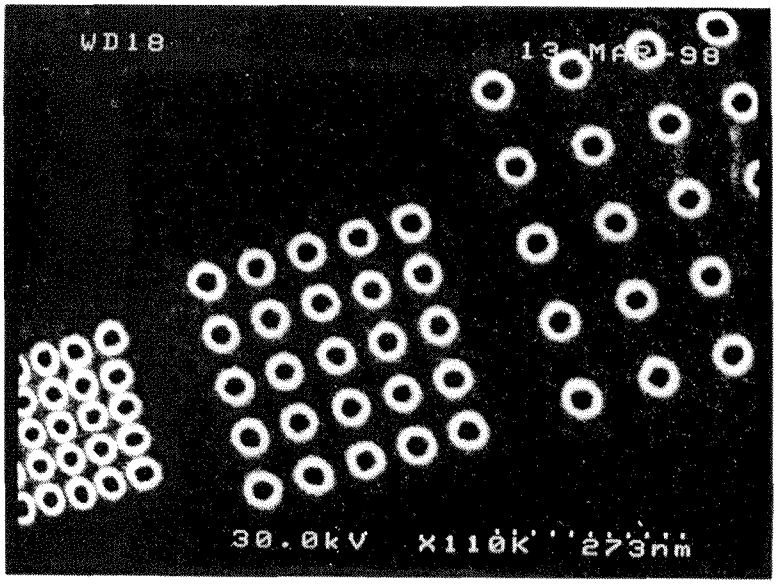

(b)

Figure 7.4: SEM images of several arrays of holes of various diameter and spacing etched in AuPd on a Si substrate are shown. The densest array in (a) and (b) has a periodicity of 50nm and 45nm, corresponding to an areal density of ~250 and 350Gbits/in.^{2}, respectively.

the lithographic techniques used to define the individual magnets. In addition, from the standpoint of magnetics, problems such as the interaction among neighboring columns, which will eventually lead to instability and loss of stored information, will be encountered. The predicted ultimate areal density of patterned media, considering both the patterning issues using e-beam lithography as well as the limitations imposed by magnetics, will be discussed.

7.2.1 Proximity effects in electron beam lithography

With electron beam lithography, the ultimate resolution is not limited by the wavelength of an electron, as in the case of optical lithography with the minimum dimension imposed by the diffraction limit. According to the de Broglie theorem, the wavelength of an electron is given by:

$$\begin{aligned} \lambda &= \frac{h}{p} \\ &= \frac{h}{\sqrt{2mE_0}} \\ &= \frac{1.24}{\sqrt{E_0}}, \end{aligned} \tag{7.1}$$

where h is the Plank's constant, p is the momentum of the particle, E_0 is the energy of the electron in eV, and λ is the wavelength in nm. Using Equation 7.1, a 10-keV electron has a wavelength of about 0.1Å. This decreases to 0.07Å for a 30-keV electron. From this, we see that the resolution limit in electron beam lithography is not restricted by the wavelength of the electron. Instead, the size of the focused beam and the interaction of the electrons with the resist layer will be the limiting factors; the latter of which will be addressed here.

Proximity effects have been the curse of e-beam lithography. The main type (interproximity effect) involves the undesired exposure of regions in the neighborhood of an exposed area due to backscattered electrons. At 25keV, the range of backscattered electrons for a 1-μm spot is 5μm wide and this increases to 12μm wide at 50keV [84]. This range follows an $E^{1.7}$ dependence. When the voltage is low (1-10keV), most of

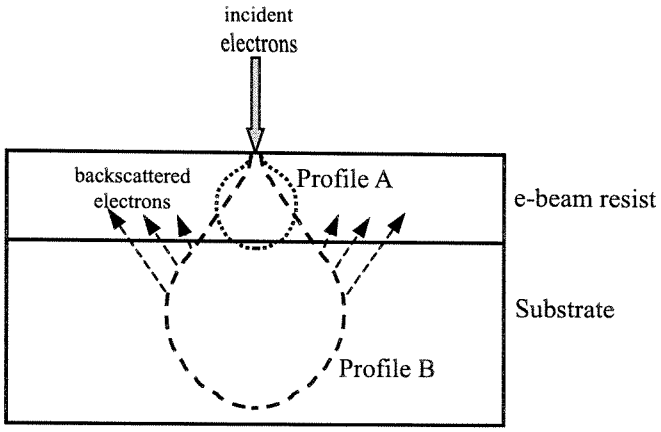

Figure 7.5: Illustration showing the extent of backscattering electrons during an e-beam exposure using low voltages (profile A) and high voltages (profile B) [85].

the forward energy from the electron beam is deposited in the resist layer (as illustrated in profile A in Figure 7.5), and the energy spread is at its minimum. At high beam energies, however, there will be a deeper penetration of the incident electrons into the substrate, and the exposure will be greatly dominated by backscattered electrons (as illustrated in profile B in Figure 7.5). As a result, lower beam voltages are preferable when the lateral extent of undesirable exposure due to proximity effects is to be minimized.

Besides the energy of the electron beam, the thickness of the resist layer is also critical in determining the extent of the backscattered electrons. It is clear from simple geometry that thicker resists will result in a wider lateral distribution of backscatterers resulting in larger exposed features. Another factor that governs the amount of lateral exposure due to the proximity effect is the atomic number, Z, of the substrate and subsequent materials underneath the e-beam resist. Substrates with a high Z number result in an enhanced resist sensitivity since fewer primary electrons are needed for the exposure due to the presence of more efficient backscatterers from the substrate. Thus, a combination of thin resist and low beam voltages, and if suitable, materials with high atomic numbers, are often employed in the fabrication of nanometer-scale structures. For further study and correction algorithms for the proximity effects in electron beam lithography, see References [86, 87, 88, 89].

If all the parameters such as the thickness of the resist and beam voltages are optimized, and correction algorithms are included to minimize the proximity effect, researchers believe that structures with a period of 20nm or smaller should be possible with e-beam lithography. Assuming a 20nm spacing between structures, this would correspond to a packing density of 1.6Tbits/in.^{2}. Since the areal density is determined by the period of the columns, the size of the columns for a patterned magenetic medium will be chosen such that the interaction among columns will be at a small enough level to maintain the stability of the individual storage elements. The decrease in the column spacing to 15 and 10nm would further increase the areal density to an even more promising level of 2.9 and 6.5Tbits/in^2.

7.2.2 From the standpoint of magnetics

Before the ultimate storage limit of perpendicular patterned media is imposed by high resolution patterning issues, certain aspects involving the magnetics in the storage elements will likely become more critical and detrimental. Researchers in the magnetic recording industry have been casting their doubts on the capability of patterned media to reach beyond the 1Tbits/in.^{2} threshold. The main concern lies in the thermal stability of the individual storage units in the magnetic medium at those types of densities. Their skepticism may be more understandable after examining the interactions and switching fields of an assembly of magnetic columns that satisfy a 1.6Tbits/in.^{2} areal density requirements.

Consider an array of Ni cylindrical particles with a 20nm center-to-center spacing arranged in a square lattice. This configuration corresponds to a packing density of 1.6Tbits/in.^{2}. Let us assume a 2:1 aspect ratio for the columns. The volume, V, of each particle is $V = \pi r^2 h = 4\pi r^3$, where r and h are the radius and height of the column, respectively. Neglecting the magnetocrystalline anisotropy, it is assumed that the main contribution to the total anisotropy is shape anisotropy, K_s, given by Equation 2.14 for ellipsoids or cylinders. For a Ni column of 2:1 aspect ratio, K_s has the value of 3.5×10^5erg/cm^3, assuming M_s of 484emu/cm^3. Following the same

arguments as in Chapter 2, in order to retain one bit of information for a minimum of 10 years, the energy barrier, ΔE, between the two possible magnetization states needs to be greater than $40k_BT$, where k_B and T are the Boltzmann constant and temperature, respectively, with $k_BT = 4.14 \times 10^{-14}$erg at $T = 300K$. This impose a requirement on the volume of the individual storage element to be: $V > 40k_BT/K$. Substituting in the value of K for a 2:1 Ni column calculated earlier, we arrive at the minimum volume to be 4.73×10^{-18}cm^3, or 4730nm^3. This gives a minimum radius of ~7nm for each column. Therefore, the minimum dimensions we have gathered so far for an array of 2:1 aspect ratio Ni columns to arrive at an areal density of 1.6Tbits/in.^{2} are: $r = 7nm$, $h = 4r = 28nm$, and $p = 20nm$ (periodicity).

Using these values, we can get an approximation of the interactions encountered from neighboring columns within the square array, as well as the switching field of the column. Referring to the perpendicular patterned media design section in Chapter 3, the interaction field, H_i, from a neighboring column is given by: $H_i = ab^3(M_s\pi/4)$, where a and b represent the column aspect ratio and ratio of column diameter and period, respectively. From the table of calculated interaction fields in Figure 3.3 (a), we find that for a 2:1 aspect ratio column of 14nm diameter and 20nm spacing ($a = 1$ and $b = 14nm/20nm = 0.7$), H_i has a value of ~261Oe. For a square array, the total amount of interaction is $9H_i$, or ~2350Oe. Now we need to calculate the switching field of a single column to determine whether the interaction field from its neighbors is sufficient to reverse its magnetization. The switching field, H_{sw}, of a magnetic column is given by: $H_{sw} = 2K/M_s$, which is 1446Oe for a 2:1 Ni column. This is smaller than the interaction field we just approximated by a significant amount, which implies that the stability of the individual columns in this configuration is a serious, and valid concern.

This instability problem can be improved to a certain extent if a material with a higher anisotropy, which can be a combination of magnetocrystalline, shape, stress and other types of induced anisotropy, is used instead of Ni. With a higher anisotropy, the minimum volume, and hence diameter, required to retain information in each column for 10 years is smaller. The ratio of diameter and periodicity of the column

will in turn be decreased, resulting in a weaker interaction field from neighboring columns. In addition, since the switching field of a column is directly proportional to the anisotropy constant, the value of H_{sw} will increase with a higher anisotropy material. Therefore it is possible, through the appropriate choice of material with a sufficiently high anisotropy, that a balance be reached between the interaction field and the switching field of an individual column within an array to satisfy the stability requirements for 1.6Tbits/in.^{2}.

One possible problem that may need to be addressed with high anisotropy materials, hence high coercivity elements, in the recording medium is whether the write transducer is capable of producing the required magnetic field to switch the magnetization of the elements. Along with this is the concern regarding the time necessary for each magnetic column to complete its magnetization reversal. In order for patterned media to be implemented in an actual magnetic recording system, each column or bit will need to have a switching time of 1ns or below. Isolated columns of higher aspect ratios tend to be more stable than the lower ones, but the former have longer switching times. The interaction fields from neighboring columns also increase with aspect ratio. There will be a trade-off between thermal stability requirements and the time of switching in determining the appropriate aspect ratio and other material parameters for the individual storage bits in patterned media for high density recording applications.

Combining the issues in current patterning technology for high resolution structures and the interaction among particles that might eventually lead to thermal stability problems, hence loss of stored information, the anticipated limit of perpendicular patterned media of around 1Tbits/in.^{2} may not be too far from reality.

Chapter 8 Conclusion

With the storage areal densities increasing at rates up to 130% per year, the magnetic recording industry has been meeting the demands by incorporating modifications to the key areas of the storage system parameters, such as the reduction in grain size in the media, increased sensitivity of the read sensor, as well as increased fields and field gradients from the write element. Researchers are confident that the current longitudinal thin-film media, with modifications to the grain size and anisotropy of the magnetic material, will be capable of taking the areal density up to the 200Gbits/in.^{2} threshold. Beyond that point, however, the individual grains in the medium may start displaying the superparamagnetic effect. When that happens, the stored information can be lost due to thermal instability of the magnetic grains. There are several proposed solutions to postpone the onset of the superparamagnetic effect, and the one we have been focusing on is the perpendicular patterned media approach.

There have been various previous approaches in the fabrication of perpendicular patterned media. Two of the approaches, embedding Ni columns in PMMA as well as SiO_2, have been briefly discussed. Our new approach uses a combination of electron beam lithography, dry etching, and electroplating to fabricate Ni column arrays that are embedded in an $(AlGa)_2O_3$/GaAs substrate. High aspect ratio columns are achieved by taking advantage of the high etching rate of AlGaAs/GaAs and its selectivity over $(AlGa)_2O_3$ in the Cl_2 chemically assisted ion beam etching procedure. Besides being a robust etching mask, the $(AlGa)_2O_3$ layer is also an ideal material for the final chemical mechanical polishing step to remove any overplated Ni mushroom. A smooth and uniformly flat surface is critical for the low "flying" height between the recording head and the magnetic medium in an actual recording system.

After the Ni column arrays are fabricated, magnetic characterization is performed using magnetic force microscopy (MFM) and scanning magnetoresistance microscopy (SMRM). Once the columns are confirmed to be magnetic using the MFM, we pro-

ceed to the SMRM characterization to determine whether the columns have a high enough coercivity, hence stability, to store and retain information for a desired period of time. Initially, we focus on 170nm diameter columns in a square array format with a periodicity of 2μm, which corresponds to 0.16Gbits/in.^{2}, to demonstrate recording at a low bit density. We have successfully recorded and retrieved data in the individual columns using a commercial inductive write and magnetoresistive (MR) read transducer. This is the first demonstration of single magnetic column per bit data storage in the perpendicular patterned media format. After this demonstration, we proceed to higher density Ni columns arranged in the form of tracks, which have a larger spacing in the cross-track (1μm apart) than the down-track (0.5 and 0.25μm apart) direction. In these track-like configurations, we have successfully demonstrated recording at areal densities of 1.3 and 2.6Gbits/in.^{2}.

We are currently limited by the spatial resolution of the spin-valve read sensors that we obtained from industry sponsors. In spite of this, we have continued to pursue higher density structures in the form of tracks as well as square arrays. So far we have fabricated 5.2Gbits/in.^{2} in tracks and up to 350Gbits/in.^{2} in a square array format. We believe that structures with a 20nm period are possible with electron beam lithography, provided an algorithm for proximity effect correction is included and other lithography parameters are optimized. From the standpoint of magnetics, issues such as interactions among neighboring columns need to be considered when determining whether the stability requirements can be met for a specific areal storage density. Taking into account both the lithography and magnetics aspects, the anticipated limit for perpendicular patterned media is around 1Tbits/in.^{2}.

For recording densities of 1Tbits/in.^{2} and greater, there are several research groups currently investigating in atomic resolution storage. One program is at Hewlett-Packard (HP), where probe storage technology is employed to read and write data to spots on the storage medium using an array of probe tips with sizes as small as a single atom [1]. The probe tip emits a well-directed beam of electrons when voltage is applied. This beam heats a data spot to write or erase a bit. For information retrieval, the tip scans the surface of the medium to detect the resistance or other

phase-dependent electrical properties of a data-containing spot, and is capable of producing images with accuracy to within a few nanometers. The relative position of the medium to the tips would be controlled by a micromover. Another program aiming towards atomic resolution storage is at the IBM Research Laboratory in Zurich, where thousands of tiny styluses are arranged in an array to write and read data as microscopic indentations on a flat polymer surface. To create the indentation, an electric current is passed through the stylus for a short amount of time, heating the tip to 400°C, which melts the polymer on the medium slightly. Strings of indentations and flats on the medium would correspond to the binary data of 1's or 0's. To retrieve the data, the tip is heated to 350°C as it scans across the surface of the polymer. When the stylus encounters and drops into an indentation, heat from the tip dissipates and the resulting temperature drop can be detected by a change in the electrical resistance of the stylus [1]. To achieve the ultimate storage density using this "millipede" approach, researchers at IBM are considering using carbon nanotubes as stylus tips, which would further enhance their resolution. Even though these atomic resolution storage approaches are still in their early development stages, and full realization as commercial products may be a decade or more away, they are a reassurance that the Information Age will not come to a halt due to the superparamagnetic effect.

Bibliography

[1] J. W. Toigo. Avoiding a data crunch. *Scientific American*, 282(5):58–74, 2000.

[2] M. Barbic. *Ph.D. Dissertation.* Department of Physics, University of California, San Diego, to be published.

[3] A. Aharoni. *Ferromagnetism.* Van Nostrand, New York, NY, 1951.

[4] G. T. Rado and H. Suhl, eds. *Magnetism – Vol. III. Spin Arrangements and Crystal Structure, Domains, and Micromagnetics.* Academic Press, New York, NY and London, UK, 1963.

[5] B. D. Cullity. *Introduction to Magnetic Materials.* Addison-Wesley Publishing Company, Reading, MA, 1972.

[6] S. Chikazumi and S. H. Charap. *Physics of Magnetism.* Krieger, Malabar, FL, 1978.

[7] E. P. Wohlfarth. *Ferromagnetic Materials.* North Holland, I-IV, Amsterdam, Holland, 1980-2.

[8] D. Jiles. *Introduction to Magnetism and Magnetic Materials.* Chapman & Hall, London, UK, 1991.

[9] A. Aharoni. *Introduction to the Theory of Ferromagnetism.* Oxford University Press, New York, NY, 1996.

[10] R. L. White. *Introduction to Magnetic Recording.* IEEE Press, New York, NY, 1985.

[11] J. C. Mallinson. *The Foundations of Magnetic Recording.* Academic Press, San Diego, CA, 2nd edition, 1993.

[12] H. N. Bertram. *Theory of Magnetic Recording.* Cambridge University Press, Cambridge, UK, 1994.

[13] C. D. Mee and E. D. Daniel. *Magnetic Recording Technology.* McGraw-Hill, New York, NY, 2nd edition, 1995.

[14] K. Ashar. *Magnetic Disk Drive Technology.* IEEE Press, Piscataway, NJ, 1997.

[15] E. D. Daniel and C. D. Mee. *Magnetic Recording: The First 100 Years.* IEEE Press, New York, NY, 1998.

[16] M. Camras. *Magnetic Recording Handbook.* Van Nostrand, New York, NY, 1988.

[17] S. X. Wang and A. M. Taratorin. *Magnetic Information Storage Technology.* Academic Press, San Diego, CA, 1999.

[18] J. Frenkel and J. Dorfman. Spontaneous and induced magnetization in ferromagnetic bodies. *Nature*, 126:274–275, 1930.

[19] C. Kittel. Theory of the structure of ferromagnetic domains in films and small particles. *Phys. Rev. Lett.*, 70:965–971, 1946.

[20] L. Néel. Propriétés d'un ferromagnétique cubiques en grains fins. *Compt. Rend.*, 224:1488–1490, 1947.

[21] E. C. Stoner and E. P. Wohlfarth. A mechanism of magnetic hysteresis in heterogeneous alloys. *Phil. Trans. Roy. Soc.*, A-240:599–642, 1948.

[22] W. F. Brown, Jr. and F. E. Luborsky. The fundamental theorem of fine-ferromagnetic-particle theory. *J. App. Phys.*, 39:993–994, 1968.

[23] A. Aharoni. Elongated single-domain ferromagnetic particles. *J. App. Phys.*, 63(12):5879–5882, 1988.

[24] L. Néel. Influence des fluctuations thermiques sur l'aimantation de grains ferromagnétiques trés fins. *Compt. Rend.*, 228:664–666, 1949.

[25] C. P. Bean and F. E. Luborsky. Particle size dependence of coercivity and remanence of single-domain particles. *J. App. Phys.*, 30:120S–129S, 1959.

[26] R. Hunt. A magnetoresistive readout transducer. *IEEE Trans. Magn.*, 7(1):150–154, 1971.

[27] T. R. McGuire and R. I. Potter. Anisotropic magnetoresistance in ferromagnetic 3d alloys. *IEEE Trans. Magn.*, 11(4):1018–1038, 1975.

[28] M. N. Baibich, I. M. Broto, A. Fert, F. Nguyen Van Dau, F. Petroff, P. Eitenne, G. Creuzet, A. Friederich, and J. Chazelas. Giant magnetoresistance of (001)Fe/(001)Cr magnetic superlattices. *Phys. Rev. Lett.*, 61(21):2472–2475, 1988.

[29] S. S. P. Parkin. private communication, 1997.

[30] B. Dieny, V. S. Speriosu, S. S. P. Parkin, D. A. Gurney, D. R. Wilhoit, and D. Mauri. Giant magnetoresistance in soft ferromagnetic multilayers. *Phys. Rev. B*, 43(1):1297–1300, 1991.

[31] C. A. Ross, H. I. Smith, T. Savas, M. Schattenburg, M. Farhoud, M. Hwang, M. Walsh, M. C. Abraham, and R. J. Ram. Fabrication of patterned media for high density magnetic storage. *J. Vac. Sci. Tech. B*, 17(6):3168–3176, 1999.

[32] R. L. White. Patterned media: a viable route to 50Gbits/in.^{2} and up for magnetic recording? *IEEE Trans. Magn.*, 33:990–995, 1997.

[33] S. Y. Chou, M. S. Wei, P. R. Krauss, and P. B. Fischer. Single-domain magnetic pillar array of 35-nm diameter and 65-Gbit/in.^{2} density for ultrahigh density quantum magnetic storage. *J. App. Phys.*, 76(10):6673–6675, 1994.

[34] L. F. Shew. Discrete tracks for saturation magnetic recording. *IEEE Trans. Broadcast and TV Rec.*, BTR-9(1):56–62, 1963.

[35] R. M. H. New. *Patterned Media for High Density Magnetic Recording, Ph.D. Dissertation.* Department of Electrical Engineering, Stanford University, 1995.

[36] R. M. H. New, R. F. W. Pease, R. L. White, R. M. Osgood, and K. Babcock. Magnetic force microscopy of single-domain single-crystal iron particles with uniaxial surface anisotropy. *J. App. Phys.*, 79(8):5851–5853, 1996.

[37] S. Y. Chou. Patterned magnetic nanostructures and quantized magnetic disks. *Proc. of IEEE*, 85(4):652–671, 1997.

[38] M. Pardavi-Horvath. Switching properties of a regular two-dimensional array of small uniaxial particles. *IEEE Trans. Magn.*, 32(5):4458–4462, 1996.

[39] E. H. Frei, A. Strickman, and D. Treves. Critical size and nucleation field of ideal ferromagnetic particles. *Phys. Rev. Lett.*, 106:446–455, 1957.

[40] A. Aharoni. Angular dependence of nucleation by curling in a prolate spheroid. *J. App. Phys.*, 82(3):1281–1287, 1997.

[41] D. R. Fredkin, T. R. Koehler, and S. Schultz. Magnetization reversal in permalloy particles - micromagnetic computations. *J. App. Phys.*, 69(8):5276–5478, 1991.

[42] C. Seberino and H. N. Bertram. Micromagnetics of long ferromagnetic particles. *IEEE Trans. Magn.*, 33(5):3055–3057, 1997.

[43] M. Schabes. Micromagnetic theory of non-uniform magnetization process in magnetic recording particles. *J. Magn. Magn. Mater.*, 95(3):249–288, 1991.

[44] M. Lederman, G. A. Gibson, and S. Schultz. Observation of thermal switching of a single ferromagnetic particle. *J. App. Phys.*, 73(10):6961–6963, 1993.

[45] R. O'Barr and S. Schultz. Switching field studies of individual single domain ni columns. *J. App. Phys.*, 81(8):5458–5460, 1997.

[46] T. Suzuki. High density optical storage materials. *Jpn. J. Appl. Phys.*, 64(3):208, 1995.

[47] E. Betzig, J. R. Trantman, R. Wolfe, E. M. Gyorgy, P. L. Flinn, M. H. Kryder, and C. H. Chang. Near-field magneto-optics and high density data storage. *App. Phys. Lett.*, 61(2):142–144, 1992.

[48] J. F. Heanue, M. C. Bashaw, and L. Hesselink. Volume holographic storage and retrieval of digital data. *Science*, 265(5173):749–752, 1994.

[49] A. G. Barre. Flash memory: magnetic disk replacement? *IEEE Trans. Magn.*, 29(6):4104–4107, 1993.

[50] J. M. Daughton. Magnetoresistive memory technology. *Thin Solid Films*, 216(1):162–168, 1992.

[51] B. D. Terris, H. P. Martin, M. E. Best, D. Rugar, and S. A. Rishton. Nanoscale replication for scanning probe data storage. *App. Phys. Lett.*, 69(27):4262–4264, 1996.

[52] J. Lindmayer, P. Goldsmith, and K. Gross. Electron trapping for mass data storage memory. *Proc. SPIE*, 1401:103, 1990.

[53] A. Scherer and H. G. Craighead. Fabrication of small laterally patterned multiple quantum-wells. *App. Phys. Lett.*, 49(19):1284–1286, 1986.

[54] R. E. Behringer, P. M. Mankiewich, and R. E. Howard. Fabrication of ultrahigh resolution structures in compound semiconductor heterostructures. *J. Vac. Sci. Tech. B*, 5(1):326–327, 1987.

[55] S. Mackie and S. P. Beaumont. Materials and processes for nanometer lithography. *Solid State Technol.*, 28(8):117–122, 1985.

[56] A. N. Broers. Resolution limits for electron-beam lithography. *IBM J. Res. Dev.*, 32(4):502–513, 1988.

[57] P. R. Krauss, P. B. Fischer, and S. Y. Chou. Fabrication of single-domain magnetic pillar array of 35nm diameter and 65Gbit/in.^{2} density. *J. Vac. Sci. Tech. B*, 12(6):3639–3642, 1994.

[58] L. Piraux, J. M. George, and J. F. Despres. Giant magnetoresistance in magnetic multilayerd nanowires. *App. Phys. Lett.*, 65(19):2484–2486, 1994.

[59] W. Xu, J. Wong, C. C. Cheng, R. Johnson, and A. Scherer. Fabrication of ultrasmall magnets by electroplating. *J. Vac. Sci. Tech. B*, 13(6):2372–2375, 1995.

[60] B. P. Van der Gaag and A. Scherer. Microfabrication below 10nm. *App. Phys. Lett.*, 56(5):481–483, 1990.

[61] A. Scherer and B. P. Van der Gaag. Characterization of nanostructures by reflection electron- microscopy. *App. Phys. Lett.*, 56(25):2566–2568, 1990.

[62] G. A. Gibson, J. F. Smyth, and S. Schultz. Observation of the switching fields of individual permalloy particles in nanolithographic arrays via magnetic force microscopy. *IEEE Trans. Magn.*, 27(6):5187–5189, 1991.

[63] V. L. Lainer and N. T. Kudryatsev. *Fundamentals of Electroplating II, 3rd ed.* U. S. Department of Commerce, New York, NY, 1957.

[64] D. A. Kyser. Spatial-resolution limits in electron-beam nanolithography. *J. Vac. Sci. Tech. B*, 1(4):1391–1397, 1983.

[65] R O'Barr, S. Y. Yamamoto, S Schultz, W. Xu, and A. Scherer. Fabrication and characterization of nanoscale arrays of nickel columns. *J. App. Phys.*, 81(8):4730–4732, 1997.

[66] S. Y. Yamamoto, R. O'Barr, and S. Schultz. MR head response from arrays of lithographically patterned perpendicular nickel columns. *IEEE Trans. Magn.*, 33(5):3016–3018, 1997.

[67] J. Wong, A. Scherer, M. Todorovic, and S. Schultz. Fabrication and characterization of high aspect ratio perpendicular patterned information storage media in an Al_2O_3/GaAs substrate. *J. App. Phys.*, 85(8):5489–5491, 1999.

[68] O. J. Painter, C. C. Cheng, R. K. Lee, and A. Scherer. Steam-oxidized aluminum arsenide as a high resolution ion etch mask. Unpublished.

[69] O. Dial, C. C. Cheng, and A. Scherer. Fabrication of high-density nanostructures by electron beam lithography. *J. Vac. Sci. Technol.*, 16(6):3887–3890, 1998.

[70] K. D. Choquette, K. M. Geib, C. I. H. Ashby, R. D. Twesten, O. Blum, H. Q. Hou, D. M. Follstaedt, B. E. Hammons, D. Mathes, and R. Hull. Advances in selective wet oxidation of AlGaAs alloys. *IEEE J. Select. Top. Quant. Elect.*, 3(3):916–926, 1997.

[71] K. D. Choquette, K. M. Geib, C. I. H. Ashby, R. D. Twesten, O. Blum, H. Q. Hou, D. M. Follstaedt, B. E. Hammons, D. Mathes, and R. Hull. Selective oxidation of buried AlGaAs versus AlAs layers. *App. Phys. Lett.*, 69(10):1385–1387, 1996.

[72] J. Wong, A. Scherer, M. Barbic, and S. Schultz. Perpendicular patterned media in an $(Al_{0.9}Ga_{0.1})_2O_3$/GaAs substrate for magnetic storage. *J. Vac. Sci. Tech. B*, 17(6):3190–3196, 1999.

[73] Rodel, Inc. Newark, Delaware 19713.

[74] M. Todorovic, S. Schultz, J. Wong, and A. Scherer. Writing and reading of single magnetic domain per bit perpendicular patterned media. *App. Phys. Lett.*, 74(17):2516–2518, 1999.

[75] S. Glasstone. *Introduction to Electrochemistry.* D. Ban Nostrand Company, Inc., New York, NY, 1949.

[76] Y. Martin and H. K. Wickramasinghe. Magnetic imaging by force microscopy with 1000Å resolution. *App. Phys. Lett.*, 50(20):1455–1457, 1987.

[77] S. Y. Yamamoto and S. Schultz. Scanning magnetoresistance microscopy (SMRM): Imaging with a MR head. *J. App. Phys.*, 81(8):4696–4698, 1997.

[78] D. Rugar, H. J. Mamin, P. Guethner, S. E Lambert, J. E Stern, I. McFadyen, and T. Yogy. Magnetic force microscopy: General principles and application to longitudinal recording media. *J. App. Phys.*, 68(3):1169–1183, 1990.

[79] D. Rugar, H. J. Mamin, and P. Guethner. Improved fiber-optic interferometer for atomic force microscopy. *App. Phys. Lett.*, 55(25):2588–2590, 1989.

[80] S. Y. Yamamoto and S. Schultz. Scanning magnetoresistance microscopy. *App. Phys. Lett.*, 69(21):3263–3265, 1996.

[81] R. Potter. Digital magnetic recording theory. *IEEE Trans. Magn.*, 10(3):502–508, 1974.

[82] Karlqvist1954. Calculation of the magnetic field in the ferromagnetic layer of a magnetic drum. *Trans. Roy. Inst. Technol. Stockholm*, 86:3, 1954.

[83] H. N. Bertram. Private communication.

[84] W. M. Moreau. *Semiconductor lithography principles, practices, and materials.* Plenum Press, New York, NY, 1987.

[85] A. Barraud, C. Rosillo, and A. Ruadel-Texrier. Monomolecular resists – A new approach to high resolution electron beam microlithography. *J. Vac. Sci. Technol.*, 16(6):2003–2007, 1979.

[86] A. Olkhovets and H. G. Craighead. Low voltage electron beam lithography in PMMA. *J. Vac. Sci. Tech. B*, 17(4):1366–1370, 1999.

[87] S. J. Wind, P. D. Gerber, and H. Rothuizen. Accuracy and efficiency in election beam proximity effect correction. *J. Vac. Sci. Tech. B*, 16(6):3262–3268, 1998.

[88] R. Crandall, U. Hofmann, and R. L. Lozes. Contrast limitations in electron-beam lithography. *J. Vac. Sci. Tech. B*, 17(6):2945–2947, 1999.

[89] U. Hofmann, R. Crandall, and L. Johnson. Fundamental performance of state-of-the-art proximity effect correction methods. *J. Vac. Sci. Tech. B*, 17(6):2940–2944, 1999.